DEVELOPMENT OF HIGH STRENGTH LIGHTWEIGHT HIGH ENTROPY ALLOYS (LWHEAs)

A THESIS SUBMITTED TO
THE GRADUATE SCHOOL OF NATURAL AND APPLIED SCIENCES
OF
MIDDLE EAST TECHNICAL UNIVERSITY

BY

GÖKHAN POLAT

IN PARTIAL FULFILLMENT OF THE REQUIREMENTS
FOR
THE DEGREE OF DOCTOR OF PHILOSOPHY
IN
METALLURGICAL AND MATERIALS ENGINEERING

JANUARY 2020

Approval of the thesis:

DEVELOPMENT OF HIGH STRENGTH LIGHTWEIGHT HIGH ENTROPY ALLOYS (LWHEAS)

submitted by **GÖKHAN POLAT** in partial fulfillment of the requirements for the degree of **Doctor of Philosophy in Metallurgical and Materials Engineering Department, Middle East Technical University** by,

Prof. Dr. Halil Kalıpçılar
Dean, Graduate School of **Natural and Applied Sciences**

Prof. Dr. Cemil Hakan Gür
Head of Department, **Met. and Mat. Eng.**

Assoc. Prof. Dr. Yunus Eren Kalay
Supervisor, **Met. and Mat. Eng., METU**

Examining Committee Members:

Prof. Dr. Tayfur Öztürk
Met. and Mat. Eng., METU

Assoc. Prof. Dr. Yunus Eren Kalay
Met. and Mat. Eng., METU

Prof. Dr. Cemil Hakan Gür
Met. and Mat. Eng., METU

Assoc. Prof. Dr. Hasan Kotan
Met. and. Mat. Eng., Necmettin Erbakan University

Assoc. Prof. Dr. Yiğit Karpat
Industrial Engineering, Bilkent University

Date: 02.01.2020

I hereby declare that all information in this document has been obtained and presented in accordance with academic rules and ethical conduct. I also declare that, as required by these rules and conduct, I have fully cited and referenced all material and results that are not original to this work.

Name, Surname: Gökhan Polat

Signature:

ABSTRACT

DEVELOPMENT OF HIGH STRENGTH LIGHTWEIGHT HIGH ENTROPY ALLOYS (LWHEAs)

Polat, Gökhan
Doctor of Philosophy, Metallurgical and Materials Engineering
Supervisor: Assoc. Prof. Dr. Yunus Eren Kalay

January 2020, 132 pages

In this thesis, the HEA formation ability of low-density elements was carefully studied in detail. In this respect, lightweight or relatively lightweight elements such as B, Mg, Al, Si, Ti, V, Cr, Mn and combinations of these elements with high-density elements such as Cu, Ni were used to produce novel lightweight high entropy alloys (LWHEAs) relative to the density of steel parts (~7.86 g/cm^3).

This thesis involves the design, production, and characterization of LWHEAs. The design and selection of the proper elements to be used in such alloys were calculated based on thermophysical calculations, Thermo-Calc HEA database and first-principle calculation with Vienna Ab Initio Simulation Package (VASP). Firstly, the HEA formation ability of selected elements and their compositions were determined by these computational methods. Then, the selected compositions were produced by copper heart arc-melting set-up adapted with suction casting technique. The LWHEAs are investigated in detail by using electron microscopy (SEM, TEM), X-ray diffraction (XRD) and thermal analysis techniques. The specimens were analyzed to determine the corresponding mechanical properties under compression test. The most promising alloy was found to be $Cu_{29}Ni_{29}Al_{14}Ti_{14}Cr_{14}$ with its relatively low density (6.76 g/cm^3) among the investigated LWHEAs. The suction cast LWHEA is annealed at 900 °C for 2 h. based on the phase diagram constructed by Thermo-Calc software. The annealed

$Cu_{29}Ni_{29}Al_{14}Ti_{14}Cr_{14}$ LWHEA shows optimal mechanical behavior with 855 MPa compressive strength, 22.6 % ductility and 338 HV hardness. Also, $Cu_{29}Ni_{29}Al_{14}Ti_{14}Cr_{14}$ LWHEA was produced from industrial grade raw materials at scale-up using the induction casting technique. The 5 mm cylindrical samples annealed at 900 °C for 2 h. show 902 MPa yield strength, 1332 MPa fracture strength and 12.7 % ductility.

Keywords: High Entropy Alloys, Mechanical Properties, Characterization, Structure, Lightweight

ÖZ

YÜKSEK MUKAVEMETLİ HAFİF YÜKSEK ENTROPİ ALAŞIMLARININ (HYEA) GELİŞTİRİLMESİ

Polat, Gökhan
Doktora, Metalurji ve Malzeme Mühendisliği
Tez Danışmanı: Doç. Dr. Yunus Eren Kalay

Ocak 2020, 132 sayfa

Bu tez çalışmasında düşük yoğunluklu elementlerin YEA oluşturma yeteneği ayrıntılı olarak incelenmiştir. Bu bağlamda, B, Mg, Al, Si, Ti, V, Cr, Mn gibi hafif veya nispeten hafif elementler ve bu elementlerin Cu, Ni gibi yüksek yoğunluklu elementlerle kombinasyonları, çelik malzemelerin yoğunluğuna kıyasla (~7,86 gr/cm^3) yeni HYEA'lar üretmek için kullanılmıştır.

Bu tez, HYEA'ların tasarımını, üretimini ve karakterizasyonunu içermektedir. Bu tür alaşımlarda kullanılacak uygun elemanların seçimi tasarımı, termofiziksel hesaplamalar, Thermo-Calc YEA veritabanı ve Vienna Ab Initio Simülasyon Paketi (VASP) ile ilk prensip hesaplaması esas alınarak gerçekleştirilmiştir. İlk olarak, bu hesaplama yöntemleri ile seçilen elementlerin HEA oluşturma kabiliyeti ve bunların kompozisyonu belirlenmiştir. Daha sonra, seçilen bileşimler, emişli döküm tekniğine uyarlanmış bakır tablalı ergitme düzeneği ile üretilmiştir. HYEA'lar, elektron mikroskobu (SEM, TEM), X-ışını kırınımı (XRD) ve termal analiz teknikleri kullanılarak ayrıntılı olarak incelenmiştir. Ayrıca, basma testleri ile de bu numunelerin mekanik özellikleri incelenmiştir. HEA'lar arasından en umut vadeden alaşım, nispeten düşük yoğunluğa sahip (6,76 gr/cm^3) alaşım $Cu_{29}Ni_{29}Al_{14}Ti_{14}Cr_{14}$ olmuştur. Emişli dökümle üretilmiş HYEA, Thermo-Calc yazılımı yardımıyla oluşturulan faz diyagramına dayanarak 2 sa. boyunca 900 °C'de tavlanmıştır. Tavlanmış

$Cu_{29}Ni_{29}Al_{14}Ti_{14}Cr_{14}$ HYEA, 855 MPa basma dayanımı, % 22,6 süneklik ve 338 HV sertlik ile optimum mekanik davranış sergilemektedir. Ayrıca, $Cu_{29}Ni_{29}Al_{14}Ti_{14}Cr_{14}$ HYEA, indüksiyon döküm tekniği kullanılarak endüstriyel saflıkta hammaddelerden büyük boyutta üretilmiştir. 900 ° C'de 2 sa. tavlanmış 5 mm'lik silindirik numuneler, 902 MPa akma dayanımı, 1332 MPa kırılma dayanımı ve % 12,7 süneklik göstermektedir.

Anahtar Kelimeler: Yüksek Entropi Alaşımları, Mekanik Özellikler, Karakterizasyon, Yapı, Hafif

This thesis is dedicated to my family, and especially to my mother.

ACKNOWLEDGEMENTS

I would like to express my deepest gratitude to my thesis advisor Assoc. Prof. Dr. Y. Eren Kalay for his valuable support, contribution, inspiration, motivation, enthusiasm and guidance in every step of my thesis. He is one of the best inspiring scientists for me in terms of research, ethics, and social responsibility.

I would also like to send my special acknowledge and thanks to Ziya Anıl Erdal and Fatih Sıkan for their assistance and support in many stages of my studies. I wish to thank to my thesis progress meeting committee members Prof. Dr. Tayfur Öztürk and Assoc. Prof. Dr. Hasan Kotan for their invaluable participation and insights. Their support and guidance throughout the research are greatly appreciated. I am also grateful to Prof. Dr. Servet Turan and Umut Savacı for their help in TEM studies.

I owe particular thanks to my past and present laboratory mates Ayşe Merve Genç Ünalan, Bengisu Sarı, Doğancan Sarı, Serkan Yılmaz, Sıla Ece Atabay Sıkan, Serkan Koylan, Lütfi Koray İroç, Doğuhan Sarıtürk, Tolgahan Ulucan and Emel Erdal for all of their friendship and help throughout this process.

I am also very grateful to my family for their endless love, support and encouragement throughout my education life.

At last but not least, I would also like to extend my gratitude to Gülten Çelik, Rabia Orhan Çeliktaş and Emrah Çeliktaş for making every situation better with their support and friendship.

This work is partially supported by the Scientific and Technological Research Council of Turkey (TUBITAK) under grant no. 216M058.

TABLE OF CONTENTS

LIST OF TABLES

TABLES

LIST OF FIGURES

FIGURES

LIST OF ABBREVIATIONS

ABBREVIATIONS

HEA	High Entropy Alloy
MEA	Medium Entropy Alloy
LWHEA	Lightweight High Entropy Alloy
HA-BMG	High Entropy Bulk Metallic Glass
MG	Metallic Glass
VEC	Valance Electron Concentration
DFT	Density Functional Theory
GPa	Giga Pascal
MPa	Mega Pascal
FCC	Face Centered Cubic
BCC	Body Centered Cubic
HCP	Hexagonal Close Packed
HV	Vickers Hardness
IC	Intermetallic Compound
XRD	X-ray Diffraction
SEM	Scanning Electron Microcopy
TEM	Transmission Electron Microscopy
SE	Secondary Electron
HT-XRD	High Temperature X-ray Diffraction
CCA	Complex Concentrated Alloy

LIST OF SYMBOLS

SYMBOLS	
Å	Angstrom
°C	Degree Celsius
K	Kelvin
S_{conf}	Configurational Entropy
S_{mix}	Entropy of Mixing
ΔH_{mix}	Enthalpy of Mixing
ΔG_{mix}	Gibbs Free Energy of Mixing
δ	Atomic Size Difference
$\bar{r}$	Average Atomic Radius
r_i	Radius of i^{th} Element
T_m	Melting Point

CHAPTER 1

INTRODUCTION

Conventional alloy systems are based on one or two main components. The properties such as mechanical, electrical, magnetic, corrosion can be improved by the addition of minor alloying elements to the main component. That being said, such alloying strategy restricts the researchers to increase the alloy configuration and forcing them to study only in the regions close to the edge or corner of the multicomponent systems. However, there is less knowledge about the center of phase diagrams of multicomponent systems. In this manner, high entropy alloys (HEAs) concept which was first proposed in 2004, makes it possible to study the center part of the phase diagrams of multicomponent systems. HEA concept introduces a new area to produce novel alloys with unique properties that cannot be achieved by conventional alloy systems. HEAs are basically defined as a new type of solid solution that contains at least five or more principal elements with a composition between 5-35 at. % for each candidate element. As shown in Figure 1.1, these alloy systems are located at the center or close to the center of the phase diagram [1] that it increases the configurational entropy to its maximum. Thus, these HEAs are also called equiatomic or near equiatomic alloys. Due to their higher configurational entropy (S_{conf}) stable single or dual solid solution phases without any intermetallic can be produced maintaining the phase stability even at elevated temperatures.

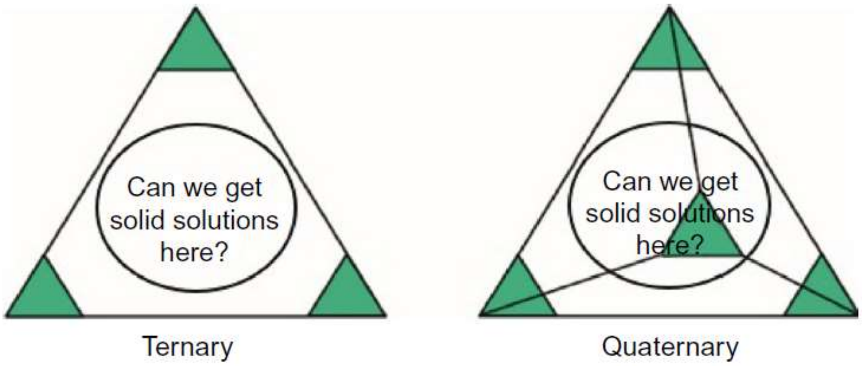

Figure 1.1. Schematic view of ternary and quaternary systems that showing regions of the phase diagram [1]

Recently, there is great attention to HEAs to obtain new and superior physical and mechanical properties. However, there are limited studies on lightweight high entropy alloys (LWHEA) due to the difficulty to produce such alloys with single or dual solid solution phases from low-density elements. So, the development of LWHEA is one of the challenging topics in this field for industrial applications. In the present thesis, the HEA formation ability of low-density elements will be studied. In this manner, lightweight elements which are B, Mg, Al, Si, Ti, V, Cr, Mn and combinations of these elements with high-density elements such as Fe, Co, Ni, Cu, Zn will be used to obtain a LWHEA relative to the density of steel materials (~7.86 g/cm^3). Such kind of alloys can be applicable to the automotive industry, even in the high-temperature parts to reduce the weight of a car with their low density and high strength. Thus, such a car can save the consumed energy and decrease CO_2 emission that is regulated by European Emission Standards (Euro6).

The thesis involves the design, production, and characterization of LWHEAs. The design and selection of the proper elements to be used in such alloys are calculated based on basic thermodynamics equations, Thermo-calc HEA database and first-principle calculation with Vienna Ab-initio Simulation Package (VASP). Using these techniques, the elements and their molar ratios are determined. Firstly, HEA ability of selected elements and their compositions are determined by these computational methods. Then, the selected compositions are produced with copper heart arc-melting set-up. The effects of the cooling rate are determined using suction casting of the produced alloys into cylindrical molds with different diameters. The HEAs are investigated in detail by using electron microscopy (SEM, TEM), X-ray diffraction (XRD) and thermal analysis techniques. These specimens are also analyzed to determine their mechanical properties (compressive strength and ductility). HEAs showing the best structural and mechanical properties are produced at large scale using induction casting method to test their ability to be manufactured for the industrial purposes.

This thesis begins with providing some basic concepts, phase formation rules, four core effects of HEAs and a review of previous LWHEA studies in Chapter 2. In Chapter 3, experimental procedure and characterization techniques are given in detail. In Chapter 4, novel LWHEAs consist of B, Al, Si, Ti, V, Cr, Mn light elements are designed and experimentally investigated. Novel Cu-Ni-Al-Ti medium entropy alloys (MEAs) are designed and the effect of transition elements on the structure and mechanical properties are investigated in Chapter 5. In Chapter 6, addition of Cr or V as a fifth element on the structure and mechanical properties of Cu-Ni-Al-Ti MEAs are investigated. Finally, this thesis is concluded in Chapter 7 by highlighting the major contributions to the HEAs, LWHEAs and MEAs research fields in terms of design, simulation, structure and mechanical properties and future recommendations are emphasized in Chapter 8.

CHAPTER 2

THEORETICAL BACKGROUND

2.1. General Definition of HEAs

Conventional alloy systems are based on one or two principal elements that minor alloying elements are added to improve the properties of the alloys. Due to the limited number of elements on the periodic table, it restricts the combination of these elements to produce new alloy systems and improve their properties. In this manner, a new alloy system which is called as High Entropy Alloys (HEAs) was first proposed in 1995 that there is no such a restriction in this new alloys system. HEAs contain at least five principal elements with 5-35 at. % for each element that let us study in a wide range to produce new alloys. Although HEAs were first proposed in 1995, it has been started in 2004 by Yeh at al. Recently, there are many studies on mechanical, magnetic, and thermal properties of HEAs [2]. According to Yeh et al. [3], an alloy is defined as high entropy alloy when the following conditions are satisfied;

- Alloys show higher mixing entropy in liquid or solid solution,
- Containing at least five or more principal elements,
- The concentration of each element 5-35 at. %.

2.2. Prediction Formation of Solid Solution, Phases and Crystal Structure in HEAs

Basically, HEA term is based on the highest configurational entropy (S_{conf}) of the alloy system containing at least five principal elements. However, the traditional alloy systems depend principally on one or two main components with the addition of small amounts of alloying elements to improve the properties or processability of the material [4]. According to the Gibbs phase rule, when the number of the main element is increased, the formation of intermetallic compounds and complicated microstructures, which could lead to brittleness and processing problems, may take place [5]. However, studies conducted by Yeh et al. [6], [7] show that alloys with five or more principal elements and the concentrations between 5 and 35 at. % can be obtained without the formation of intermetallic phases. Solid solution phases have usually higher entropy compared to intermetallics that can greatly decrease the Gibbs free energy of the system [8]. Therefore, the HEAs generally form face-centered cubic (FCC) and/or body-centered cubic (BCC) structures rather than many complex phases. Moreover, hexagonal close-packed (HCP) structure, nano-sized precipitated and amorphous phases can be observed in HEAs [9]–[12].

When equiatomic composition is prepared for each component of an alloy containing five or more principal elements, it is shown that $S_{konf}/R = \ln N$ (N: number of elements present in the alloy, R: gas constant). From this equation, when five principle elements are chosen for a HEA (Figure 2.1), S_{conf}/R will be equal to $\ln 5=1.61$. If S_{konf}/R is equal or higher than this critical value, this alloy can be defined as a HEA. Another important parameter for HEA formation ability of a system is the delta parameter (δ) which is defined as the atomic size difference between candidate atoms. In addition to these parameters, enthalpy of mixing (ΔH_{mix}) is important for the formation of HEAs rather than intermetallic phases.

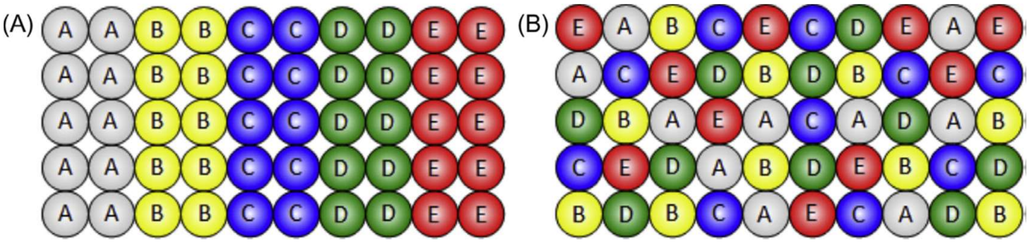

Figure 2.1. An equi-atomic multicomponent system containing five elements a) before mixing, b) randomly mixed solid solution form [13]

The general thermodynamic parameters are summarized as follows [14], [15]:

- $\Delta S_{mix} > 13.38$ J/ K mol
- $\delta < 6.6$
- -22 kJ/mol $< \Delta H_{mix} <$ 7 kJ/mol

$\Delta G_{mix}=\Delta H_{mix}- \Delta S_{mix}$ Equation 2.1

where ΔG_{mix} is the Gibbs free energy of mixing, ΔH_{mix} is the enthalpy of mixing, ΔS_{mix} is the entropy of mixing, and T is the absolute temperature. It is clear from the equation that when equiatomic composition is selected for HEAs, ΔS_{mix} reaches its maximum value (Figure 2.2) for a specific ΔH_{mix}, it will decrease the ΔG_{mix} value of the system. The lower ΔG_{mix} will lead to the formation of stable phases [5].

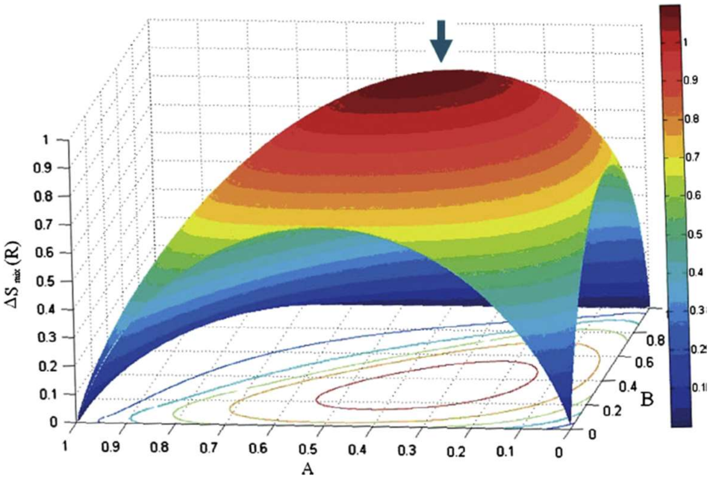

Figure 2.2. The change of ΔS_{mix} with changing composition for a ternary system [16]

The thermodynamic criteria ΔG_{mix}, ΔH_{mix}, ΔS_{mix}, and δ parameters are critical for the formation of HEAs. Derivation and design of these parameters are other important issues for HEA formation ability of selected candidates. According to Takeuchi et al. [14], S_{conf} can be calculated with the help of the concentration of each element in the alloy system. In the same study, they showed that with counting the possible interactions of solute and solvent atoms in a hypothetical system, S_{conf} value can be calculated based on thermodynamic principles. That calculation is shown below [14]:

$$\frac{S_{conf}}{R} = -\sum_{i=1}^{N} c_i \ln c_i$$ Equation 2.2

$$\frac{S_{conf}}{R} = \ln N$$ Equation 2.3

where c_i is the concentration of i^{th} element in the alloy. In the same study, they calculated ΔH_{mix}, δ and $\bar{r}$ for an alloys system [14]:

$$\Delta H_{mix} = 4x \sum_{j \neq i}^{N} \sum_{i=1}^{N} \Delta H_{ij} c_i c_j \qquad \text{Equation 2.4}$$

$$\delta = 100x \sqrt{\sum_{i=1}^{N} c_i} \, (1 - \frac{r_i}{r})^2 \qquad \text{Equation 2.5}$$

$$\bar{r} = -\sum_{i=1}^{N} c_i \, r_i \qquad \text{Equation 2.6}$$

Where r_i is the radius of i^{th} element and $\bar{r}$ is the average value for all the atoms in the system. By using these equations the most suitable composition for the formation of a specific HEA can be determined empirically with thermodynamic calculations.

Another critical point for HEAs is the estimation of the resultant crystal structure. The common crystal structures in the literature are face-centered cubic (FCC), body-centered cubic (BCC) and hexagonal closed pack (HCP) for HEAs. The statistic approaches conducted for possible structures of HEAs show that 50 % of solid solution (ss) will be BCC, 49 % will be FCC and the remaining portion will be HCP structure [15]. Valance electron concentration (VEC) (Table 2.1) is a good physical approach to determine the final crystal structure of a HEA. Guo et al. [17] show that when VEC is equal or higher than 8, the resultant crystal structure will be FCC; when this value is lower than 6.87 the final crystal structure will be BCC. In the gap of 6.67 and 8 for VEC, HEAs will have FCC+BCC composite crystal structure.

Table 2.1. Physicochemical properties of commonly used elements for the production of HEAs [17]

Element	**Atomic radius (Å)**	**VEC**
Al	1.432	3
B	0.820	3
C	0.773	4
Co	1.251	9
Cr	1.249	6
Fe	1.241	8
Mn	1.350	7
Mo	1.363	6
Nb	1.429	5
Ni	1.246	10
Ta	1.430	5
Ti	1.462	4
V	1.316	5
W	1.367	6

VEC of a multicomponent system can be calculated according to the following formula [15]:

$$\mathrm{VEC} = \sum \mathrm{c_i}\,\mathrm{VEC_i} \qquad \text{Equation 2.7}$$

2.3. Four Core Effects of HEAs

There are so many factors that affect mechanical, microstructural and other properties of HEAs. However, the most common factors are high entropy effect, sluggish diffusion effect, severe lattice distortion effect, and cocktail effect which are called as "core effects" [5], [12].

2.3.1. High Entropy Effect

High entropy effect is the most important parameter for HEAs. This effect differs HEAs from conventional alloys that it leads to produce simple solid solution phases [13]. This concept states that by increasing the $S_{conf.}$, the free energy of solid solutions decreases. This situation promotes the formation of solid solution phases, especially at elevated temperatures. Because of the increasing solubility among candidate elements, the resultant number of phases decreases in HEAs. The mixing entropy of solid solution phases is greater than intermetallic compounds in conventional alloy systems (Table 2.2). In the case of HEAs, the difference of mixing entropy between solid solution and intermetallic compounds is quite large due to the higher number of principal elements in the alloy. Thus, HEAs have higher solid solution stability particularly at higher temperatures [2], [13].

Table 2.2. Comparison of ΔG_{mix}, ΔH_{mix}, ΔS_{mix} values for elemental phases, compounds, intermediate phases and random solid solutions [13]

Comparative States	Elemental Phases	Compounds	Intermediate Phases	Random Solid Solution
ΔH_{mix}	~ 0	Large negative	Less large negative	Medium negative
ΔS_{mix}	~ 0	~ 0	Medium	$\Delta S_{mix} = -R\sum_{i=1}^{N} c_i \ln c_i$
ΔG_{mix}	~ 0	Large negative	Larger negative	Larger negative

When the temperature is increased to elevated temperatures, the degree of ordered structure in HEAs decreases. Therefore, although these alloys show ordered structure in their as-cast state, the ordered structure transform to solid solution at elevated temperatures. On the other hand, when the formation enthalpy of intermetallic compounds is sufficiently high at higher temperatures, the effect of the enthalpy will overcome the high entropy effect. In this case, instead of solid solution phases, intermetallic compounds will be stable phases [2].

2.3.2. Sluggish Diffusion Effect

Sluggish diffusion effect was first proposed by Yeh et al. [15] in 2006 and it was based on secondary observation. However, the first study on diffusion in HEAs was published in 2013. This claim includes the formation of nanocrystal phases that the presence of this nanocrystals cause a slow diffusion in HEA solid solution phases as compared to the conventional alloys [2], [15].

Sluggish diffusion effect can be explained with two major concepts. First of all, due to the highest number of elements present with high at. % in HEAs, the neighboring atoms in the lattice site of a crystal structure are different than each other. According to recent studies [18], as shown in Figure 2.3, higher fluctuations in potential energies of lattice sites cause slow diffusion in HEAs. When an atom jump from one site to a vacancy, the interaction between atoms will be different than the first original case. When an atom is replaced by another type of atom, this new atomic configuration will cause a different bonding between atoms that the local energy will change. When an atom jumps to a lower energy site, this atom will be trapped in the structure that the probability of this atom leaving that site is very low. In this scenario, the atom will be trapped in the structure. In contrast to the first case, when the final energy site of the atom is high, it will have a higher probability to go back to its original site. Both of these cases will slow down the diffusion kinetics [2], [18]. The second important case for slow diffusion rates in HEAs is the different diffusion rates of each element present in a HEA. Some atoms in HEA may be less active than the other type of atoms that the chance of these atoms to jump to a vacancy is very low when these two types of atoms are in competition. The atoms that have low diffusion rates will become the rate limited atoms that they will prevent the transformations in the system [2].

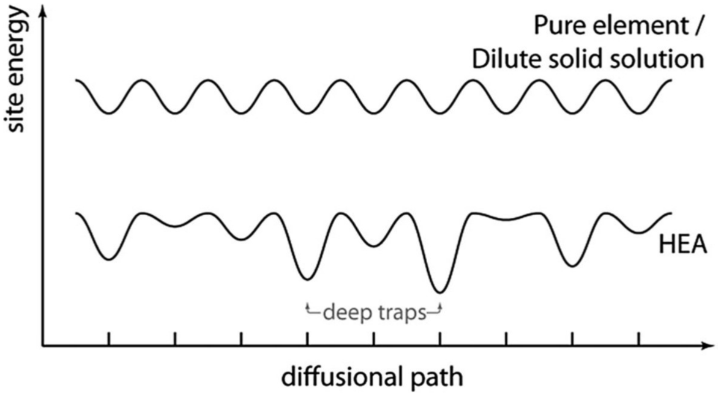

Figure 2.3. The difference in the lattice in lattice potential energy along with an atomic diffusion profile for HEAs (bottom) and dilute solid solution (top) [18]

2.3.3. Severe Lattice Distortion Effect

HEAs contain at least five principal elements. Each element in the alloy has a different atomic radius. The probability of occupying the lattice sites for the different elements is the same that a crystal structure contains all the atoms of principal elements. Due to the difference in atomic radius, lattice distortion occurs in HEAs [19]. Yeh et al. [5] show that a decrease in X-ray diffraction (XRD) intensities is observed in CuNiAlCoCrFeSi HEA as seen in Figure 2.4. The effect of the systematic addition of principal elements is investigated in this study. They observed that although temperature decreases the intensities of XRD patterns, there is a further decrease in the intensity due to the increasing number of constituent principal elements. When the difference in the radii of the candidate elements are increased, a significant decrease in intensity is expected.

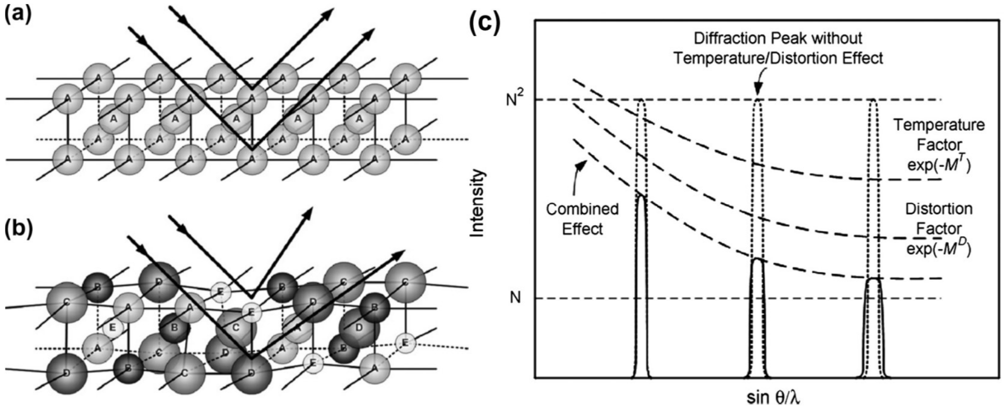

Figure 2.4. Effect of lattice distortion on XRD intensities a) perfect lattice consist of the same atoms, b) distorted lattice due to the different atoms with various radii, c) effect of temperature and lattice distortion on XRD intensities [20]

Besides the effect of lattice distortion on intensities of the phases, it also decreases thermal effects on properties of HEAs. Mechanical properties such as hardness and strength increase significantly due to the highly distorted lattice. For instance, studies show that Vickers hardness of single FCC solid solution CoCrFeMnNi HEA is 1192 MPa when it is homogenized, although the value obtained from the rule of mixture is 864 MPa [13].

2.3.4. Cocktail Effect

The cocktail effect is used for HEAs to define the improvement of properties of the alloy by the addition of five or more constituent principal elements and all the resultant properties of the phases present in the multicomponent alloy based on the properties of constituent phases. This property can be considered as a composite effect on the atomic-scale due to the contribution of each phase on the properties of HEAs [13]. However, although individual elements in HEAs affect the properties of the alloy, the interaction among the constituent atoms is not a negligible effect on the properties. According to a study conducted by Yeh et al. [4], the crystal structure of $Al_xCoCrCuFeNi$ changes from FCC to BCC with an increasing amount of Al as seen in Figure 2.5. In addition to the change in the crystal structure, the hardness of HEA increases with increasing at. % of Al element dramatically but normally Al is a soft metal and its melting point is low. This result occurs due to the formation of hard BCC phases, cohesive bonding among Al and the other atoms, and large atomic size of Al [4], [13].

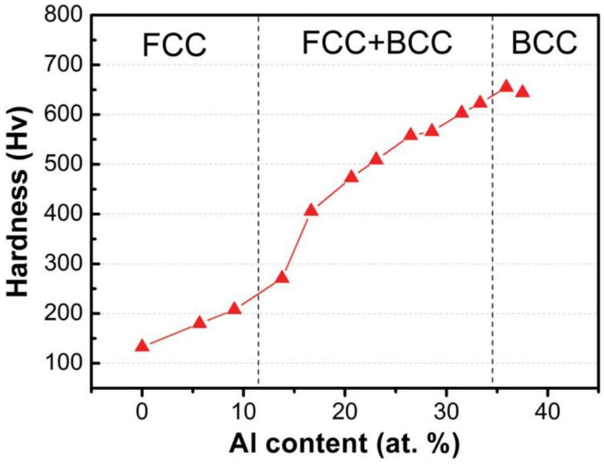

Figure 2.5. Effect of Al at. % on the hardness of $Al_xCoCrCuFeNi$ HEA [4]

2.4. Computational Materials Science for HEAs

It is clear that it is not possible to produce a HEA from randomly chosen five or more principal elements. As mentioned previously, some thermodynamic properties promote the formation of solid solution phases without intermetallic compounds that only carefully chosen elements and compositions can form a single FCC, BCC or their combination. The combination of elements and compositions to produce HEAs give enormous number of phases that it cannot be possible to study this experimentally. In conventional alloys, with the help of binary and ternary phase diagrams, it is possible to estimate the resultant phases for a specific temperature and composition. However, in literature, there is no phase diagram for a quaternary or higher system to predict the phases. Recently, computational methods start to become widespread that instead of studying for all the possible compositions and elements to produce HEA, a computational prediction method can save time and decrease the cost for experimental studies. The most common computational modeling techniques to predict HEA formation ability among candidate elements and their variable compositions are density functional theory (DFT) calculations, ab initio molecular dynamics (AIMD) and acronym of Calculation of Phase Diagrams (CALPHAD) [2], [4], [5], [15].

2.4.1. Density Functional Theory (DFT) Calculations

Among the other modeling technique, DFT seems the most proper technique to apply a multi-component system like HEAs. The main requirements for DFT as the input are the atomic number and crystal structure of candidate elements to calculate the electronic and cohesive properties of the alloy. With the help of these inputs, the DFT technique transforms the electronic many-body problems into a set of many coupled single-electron problems. An infinite number of alloys are processed by the software and only the promising compositions are given to the user as an output to study [4], [5].

Zaddach et al. [21] used DFT calculations to investigate the physical properties of selected solid solution alloys. They used two methods which are the exact muffin-tin orbital (EMTO) and plane-wave pseudopotential approach adapted to the Vienna ab initio simulation packages (VASP). In the same study, special quasi-random structures (SQSs) method has been developed to investigate quaternary systems [5], [21].

2.4.2. Ab Initio Molecular Dynamics (AIMD)

AIMD technique is based on quantum mechanics that it makes it easier to predict the atomic behavior of solid and liquid phases at constant elevated temperatures. Also, this technique is a common computational method to predict structural, dynamic, thermodynamic and diffusion constant at different temperatures [5].

Kivy et al. [22] used AIMD to determine crystal structures and phases of AlFeCoNi, FeCoCu and AlFeCoNiCu alloy systems. The study shows that BCC AlFeCoNi and FCC FeCoCu phases are stable at 0 K in this alloy. However, when the temperature increased to 1073 K, it is predicted that this dual-phase transforms into a single equiatomic FCC phase as shown in Figure 2.6 [22].

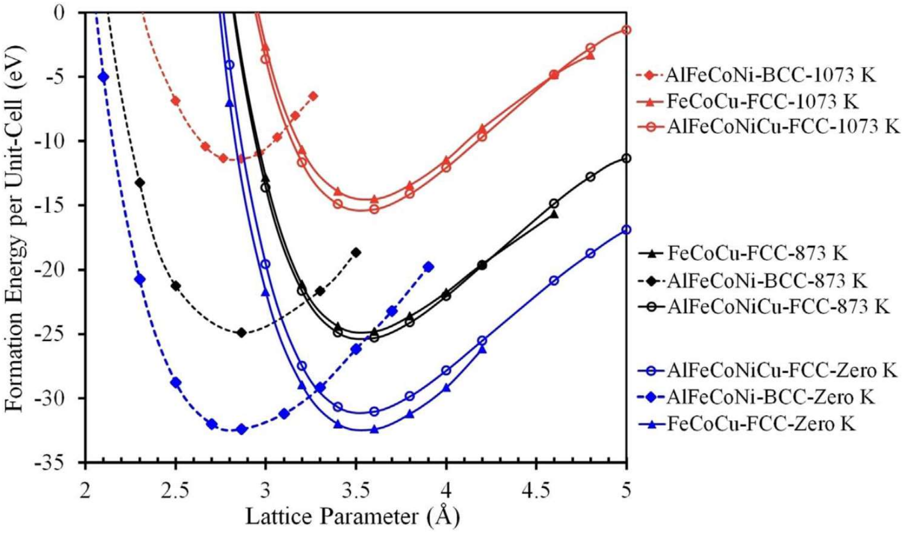

Figure 2.6. Formation energies of AlFeCoNi, FeCoCu and AlFeCoNiCu alloys at different temperatures [22]

2.4.3. Calculation of Phase Diagrams (CALPHAD)

CALPHAD is a common method in materials science to predict the possible phases in an alloy. This method is based on Gibbs Free Energy that is derived from a function of composition, temperature, and pressure for a specific system. Until quite recently, CALPHAD was only applicable to binary and ternary systems and there was no useful database for HEAs. However, a new database to predict HEA has been created in the last few years based on scientific parameters indicated in recent publications [23]–[25]. The TCHEA2 database of CALPHAD contains 15 elements which are Al, Co, Cr, Cu, Fe, Hf, Mn, Mo, Nb, Ni, Ta, Ti, V, W, and Zr. The binary module of Thermo-Calc is used to calculate the interaction between the elements in the range of composition and temperature [24].

Mao et al. [24] used CALPHAD to predict the amount of the phases present in NbTaTiV multicomponent system and the phase changes with the addition of Al to the alloy which was experimentally investigated by Yang et al. [25]. As shown in Figure 2.7, when Al is added to the $Al_xNbTaTiV$ ($0<x<1$) multicomponent system, the resultant phase remain as BCC for all the possible x values. These results well agree with the experimental studies [24], [26].

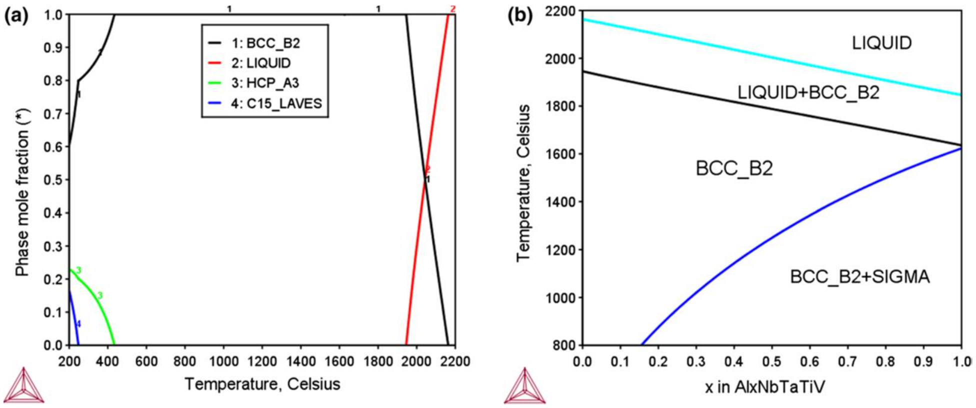

Figure 2.7. Application of CALPHAD for predicting of a) mole fraction of phases present in NbTaTiV quaternary system, b) stable phases with the addition of Al to AlxNbTaTiV alloy [24]

2.5. Fabrication Routes of HEAs

The production methods of HEAs can be divided into three main groups as shown in Figure 2.8: liquid melting, solid-state mechanical alloying and gas state mixing.

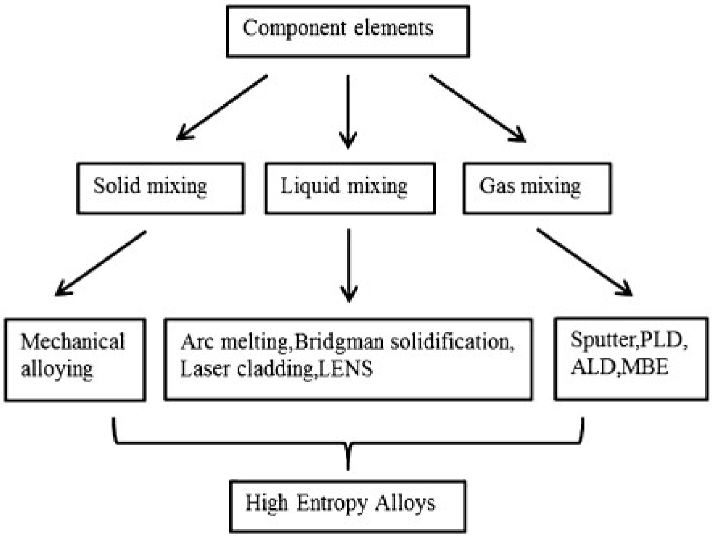

Figure 2.8. Production routes of HEAs [27]

The most common method is production HEAs of from the liquid state. It is shown in Figure 2.9 that, almost 75 % of the publications on HEAs use this technique. This method is applied by the help of arc melting, electric resistance melting, inductive melting, laser melting laser cladding and Laser Enhanced Net Shape (LENS) forming techniques. The second important method which is solid mixing includes mechanical alloying with some additional compressing processes. The last production technique for HEAs is gas mixing that includes sputter deposition, pulse laser deposition (PLD), atomic layer deposition (ALD), molecular beam epitaxy (MBE) and vapor phase deposition techniques [27], [28].

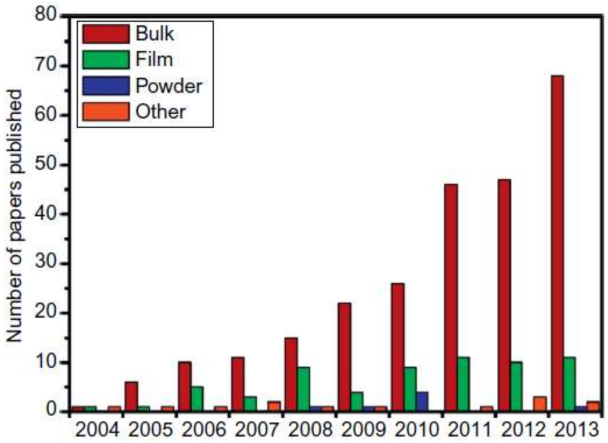

Figure 2.9. Comparison of production routes for HEAs in publications [28]

2.5.1. Liquid Melting

Arc melting is a liquid melting technique that it is the most popular technique to produce HEAs. In this technique, all the constituent elements are mixed and homogenized in a liquid state and then it is cast into copper molds as shown in Figure 2.10, schematically. The homogeneity of the alloys in HEAs has major importance that the melting process is repeated many times to ensure the chemical homogeneity.

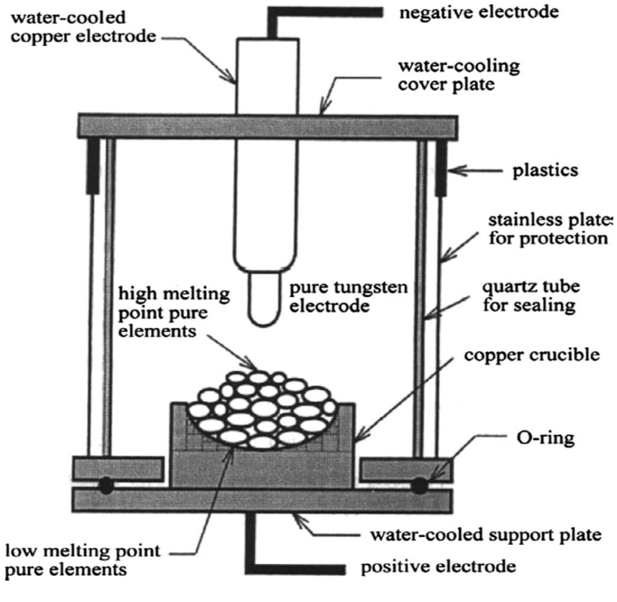

Figure 2.10. Schematic view of a typical arc-melter [5]

The torch temperature of arc melting is sufficiently high (>3000 °C) that all the candidate elements can be melted at these temperatures. However, the main drawback if this method is the vaporization problems of elements with low melting points such as Zn, and Mg. Due to the vaporization of these elements during the process, the overall chemical composition of the final alloy cannot be controlled precisely. When the elements with low melting points are required to use to produced HEAs, induction melting can be a good choice to overcome the vaporization problem [5], [28].

In the arc melting technique, a heterogeneous microstructure with segregations can be developed during solidification of the HEAs. The most common microstructure obtained in HEAs produced by arc melting is dendrite regions with interdendritic segregations [5], [27], [29]. Commonly, this kind of microstructure is observed when slow cooling rates are chosen during the solidification. Course dendrites occur in the alloy when slow cooling rates are applied, but when the cooling rates are increased (10^4 K/s) transformation of dendritic structure to fine dendritic and degenerated microstructure with further increasing cooling rates (10^6 K/s). Ultra-rapid solidification leads to the formation of ultra-fine disordered structures as shown in Figure 2.11 for $CuFeNiSi_{0.5}$ and $Al_{0.25}CuFeNiSi_{0.25}$ HEAs [30].

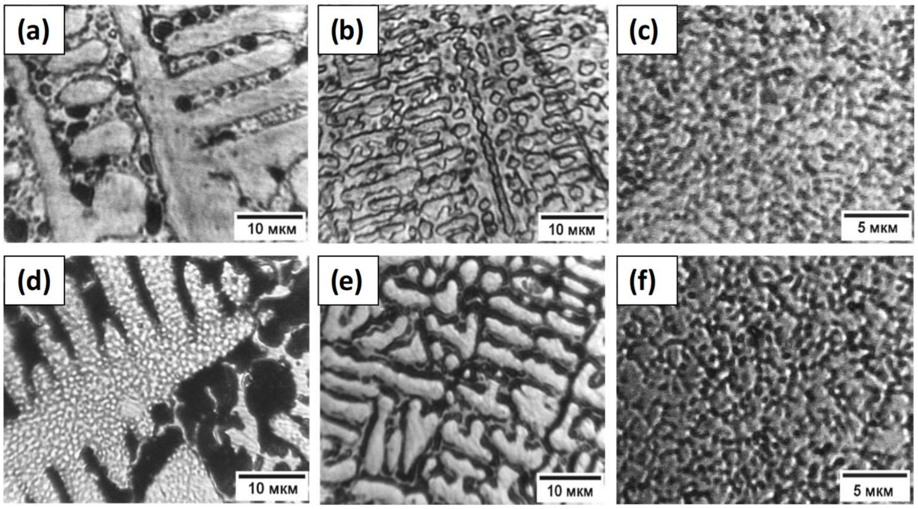

Figure 2.11. Microstructure of HEAs: $CuFeNiSi_{0.5}$ cooled at cooling rates, a) ~10^2, b) ~10^4, c) ~10^6 K/s and $Al_{0.25}CuFeNiSi_{0.25}$ cooled at cooling rates d) ~10^2, (e) ~10^4, (f) ~10^6 K/s [30]

A similar microstructure can also be seen when induction casting is used to produce HEAs. Singh et al. [29] show that decomposition occurs in AlCoCrCuFeNi HEA when the alloy is solidified slowly in the as-cast state. The cooling rate is 10-20 K/s in this case but when the cooling rate is increased to 10^6-10^7 K/s by splat quenching, the increasing cooling rates promote the formation of single solid solution phases as shown in Figure 2.12 [29].

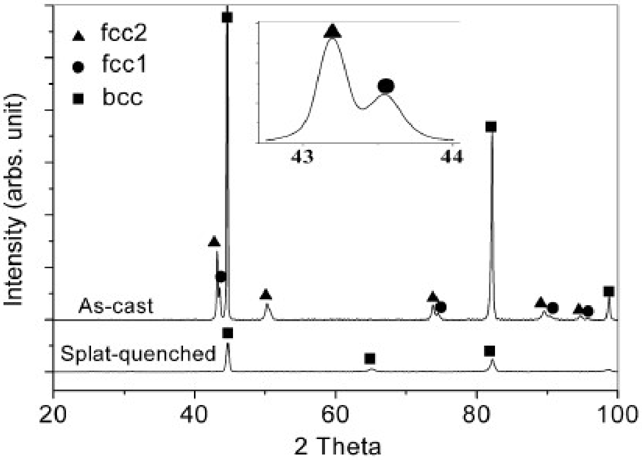

Figure 2.12. XRD patterns of as-cast and splat-quenched AlCoCrCuFeNi HEA [29]

2.5.2. Solid State Mechanical Alloying

The schematic view of the interaction between powder particles and balls in high energy ball milling technique is seen in Figure 2.13. Mechanical alloying is a powder processing technique that involves high energy ball milling of blended elements. This technique mainly consists of three steps. First of all, the pure elements are combined in a ball mill to decrease the particle size to very fine powders and to diffuse the species into each other. Secondly, hot isostatic pressing (HIP) is applied to obtain compressed and sintered powders. Finally, an additional heat treatment process can be applied to remove internal stresses that occurred during the cold compacting. Only 5 % of all HEAs are produced by a solid-state mechanical alloying method in the literature [5], [31].

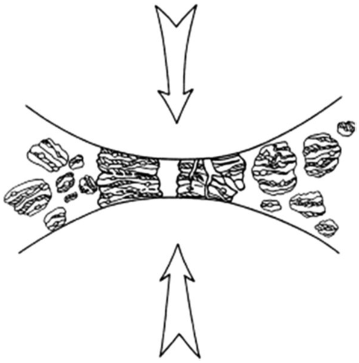

Figure 2.13. Interaction of powder particles and balls in high energy ball milling technique [28]

Wang et al. [32] prepared an equiatomic CoCrFeNiMnAl HEA by mechanical alloying and they investigated alloying behavior of the alloy. The process was applied from 6 h. to 60 h. durations with 6 h. intervals and the extracted powders for each period of the time are characterized by XRD. The results show that in the first milling period, the sample contains XRD patterns of alloying elements with decreasing intensity. When the milling period is extended to 60 h., a single solid solution phase is obtained as shown in Figure 2.14.

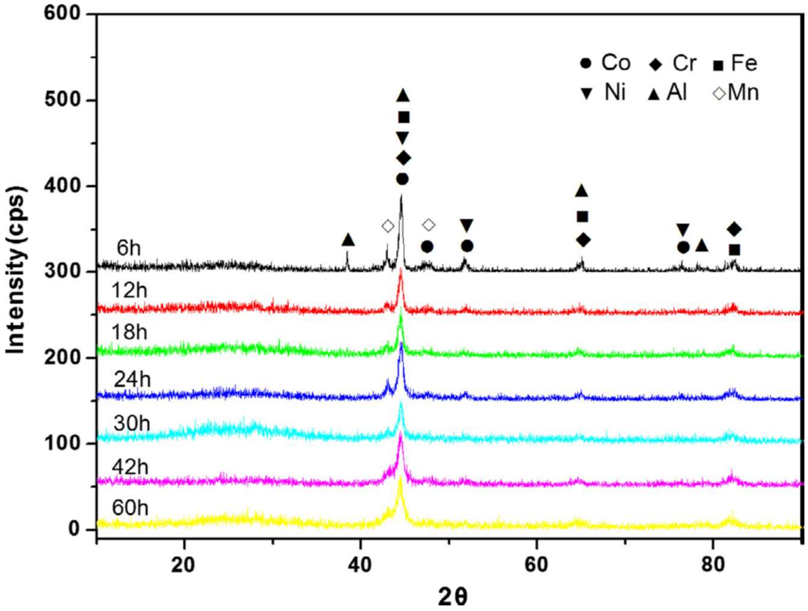

Figure 2.14. XRD patterns of ball milled CoCrFeNiMnAl HEA with different milling periods [32]

2.5.3. Gas State Mixing

Gas state mixing method involves various coating processes and almost 20 % of studies published on HEAs uses this this technique. The most popular methods for gas state mixing are magnetron sputtering and plasma nitriding. Researches apply these methods to coat thin HEA layers on the different substrate surfaces to enhance wear resistance, corrosion resistance and oxidation resistance of the surface [28].

The most common method for coating a substrate is sputter deposition. In this method, the atoms are sputtered by the bombarded charged gas ions then the substrate material is deposited with the target material as shown in Figure 2.15 (a). Another important method for coating applications is magnetron sputtering (Figure 2.15 (b)) which is based on applying electric and magnetic fields. Electric and magnetic fields are applied to increase the electron path length. The main advantage of this method is to obtain higher deposition rates at lower argon pressures [28].

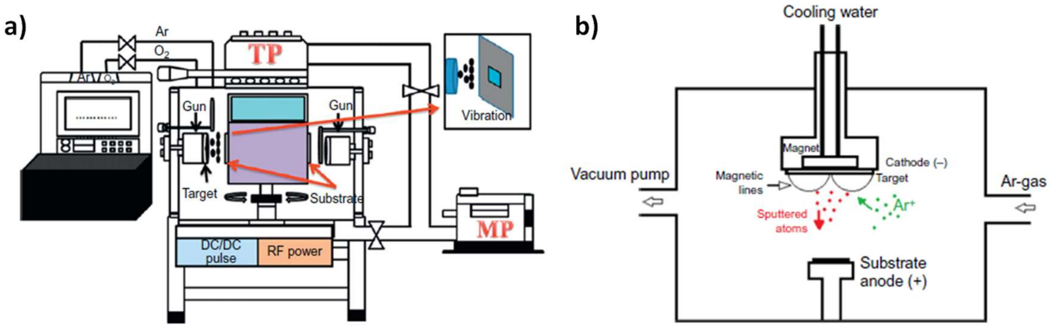

Figure 2.15. Schematic view of a) DC and RF sputtering, b) magnetron sputtering [28]

Gao et al. [33] used the magnetron sputtering technique to produce $CoCrFeNiAl_{0.3}$ HEA film on silicon substrates as shown in Figure 2.16 (a-c). In this study, a homogenous and smooth coating was performed on the substrate (Figure 2.16 (b)). The XRD pattern of the film (Figure 2.16 (c)) shows that the film consists of only a single FCC solid solution phase [33].

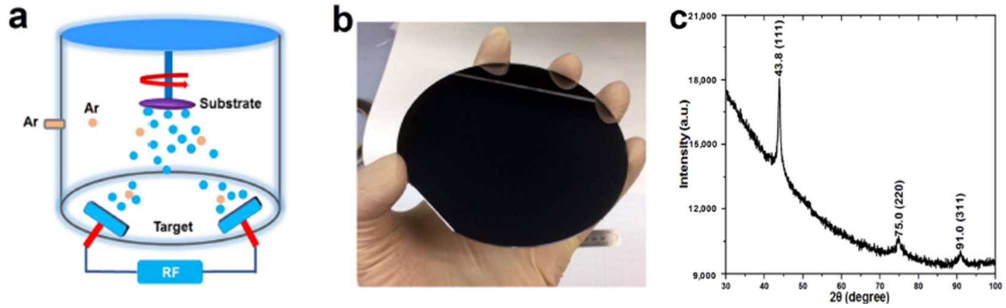

Figure 2.16. a) Schematic illustration of thin film $CoCrFeNiAl_{0.3}$ HEA production, b) $CoCrFeNiAl_{0.3}$ HEA on a silicon substrate, c) XRD pattern of $CoCrFeNiAl_{0.3}$ HEA film [33]

The mechanical and corrosion test results of $CoCrFeNiAl_{0.3}$ HEA film are shown in Figure 2.17. The nano-indentation test results of $CoCrFeNiAl_{0.3}$ HEA film show that it has superior mechanical properties with 201.4 GPa Young's modulus and 11.5 GPa hardness (Figure 2.17 (a)). Also, the potentiodynamic polarization test in 3.5 wt. % NaCl was applied on $CoCrFeNiAl_{0.3}$ HEA and it is observed that the corrosion resistance of the HEA film is better than 304 stainless steel at room temperature as seen in Figure 2.17 (b) [33].

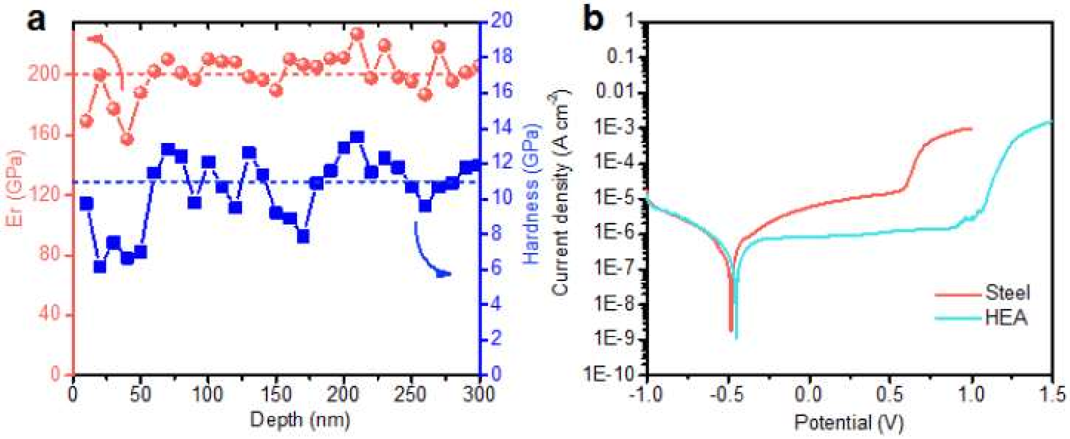

Figure 2.17. a) mechanical, b) corrosion test results of CoCrFeNiAl$_{0.3}$ HEA film [33]

2.6. Evolution of Lightweight High Entropy Alloys (LWHEAs)

Recently, there is a continuing interest in the development of HEAs such as improved structural [34], mechanical properties [35], corrosion [33], and electrical [36] behaviors. However, HEAs with lightweight along with high strength for advanced applications, there have only been a few reports of studies of lightweight high entropy alloys (LWHEAs). The primary aim of the studies is to produce LWHEAs with a density lower than 7.00 g/cm^3 [37]. The elements most frequently used in LWHEAs are the ones with lower densities such as Li (0.53 g/cm^3), Be (1.85 g/cm^3), B (2.46 g/cm^3), Mg (1.74 g/cm^3), Al (2.70 g/cm^3), Si (2.33 g/cm^3), Ti (4.51 g/cm^3) and Ca (1.55 g/cm^3). Most of these elements have higher chemical activity, larger atomic radius, an also larger difference in melting points and boiling points [38]. These properties cause difficulty in the design and production of LWHEAs. For example, Al and Ti elements tend to form ICs when they are mixed with transition metals. Moreover, although some multicomponent systems containing Li and Mg reported in the literature are defined as LWHEAs, in fact, various ICs are seen in their microstructures [37], [39]–[41]. The presence of these phases causes low strength and ductility in the LWHEAs [40], [42]. Thus, the design and development of LWHEAs alloys are more difficult than that of conventional HEAs.

Hommond et al. [39] produced AlFeMgTiZn LWHEA with a density of 4.34 g/cm^3 by mechanical alloying (MA) method. The elements used in the HEA have a broad range of melting and boiling points to be produced by conventional melt processing methods. These differences cause evaporation of significant quantities of the lower melting point elements during the melting of the HEAs [39], [43]. Therefore, a homogeneous LWHEA almost without a reduction of the elements is achieved by mechanical alloying after 10 h. of milling time [39].

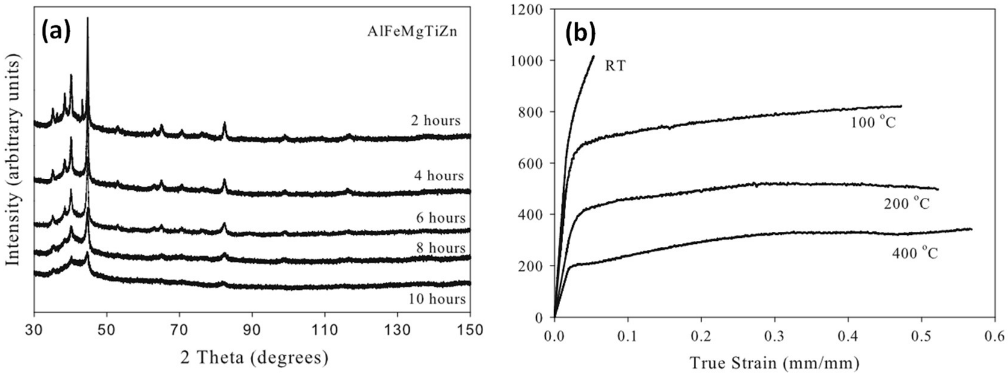

Figure 2.18. a) XRD patterns as a function of milling time, b) Compression stress-strain curves for AlFeMgTiZn LWHEA [39]

AlFeMgTiZn LWHEA has an only solid solution, they also have ICs in the final milling periods as seen in Figure 2.18 (a). It is shown in Figure 2.18 (b) that the LWHEA has a limited ductility in the as-milled state. However, the elongation is enhanced up to over 0.5 mm/mm upon annealing at 400 °C.

Youssef et al. [43] reported $Al_{20}Li_{20}Mg_{10}Sc_{20}Ti_{30}$ LWHEA with a density of 2.67 g/cm^3 using the mechanical alloying technique. The LWHEA has a single-FCC solid solution phase with nano-sized crystalline in as-milled conditions. Then, the as-milled phase in the LWHEA transformed to HCP phase upon annealing at 500 °C. The

LWHEA in as-cast and annealed conditions showed higher hardness values, 5.8 and 4.9 GPa, respectively [43].

It is clearly seen from the previous studies that the most common elements used to produce LWHEAs are Al, Mg, Be, Li, Sc, Ti and most of these elements have low melting and boiling points. Therefore, due to the evaporation problem during the casting techniques such as indication and arc melting, these alloys are commonly produced by mechanical alloying as pointed out in the literature [39], [43], [44]. However, there are many attempts to produce LWHEAs by melting and casting routes [41], [44]–[47].

Li et al. [41], [47] produced MgMnAlZnCu and $Mg_x(MnAlZnCu)_{100-x}$ (x: atomic percentage; x=20, 33, 43, 45.6 and 50 respectively) multicomponent systems by induction melting. Although these alloys have lower densities between 2.20 g/cm^3 and 5.06 g/cm^3, they do not have a single or dual solid solution phase as shown in Figure 2.19 (a, b).

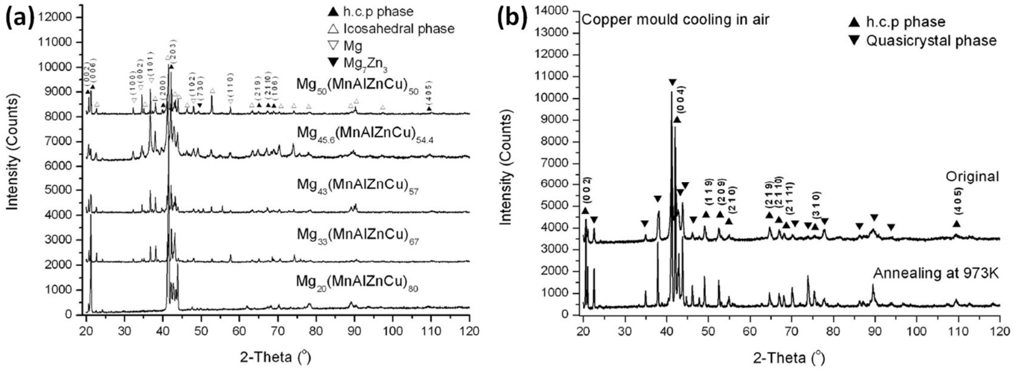

Figure 2.19. XRD patterns of a) $Mg_x(MnAlZnCu)_{100-x}$ (x=20, 33, 43, 45.6 and 50) and b) MgMnAlZnCu multicomponent systems [41], [47]

The formation of secondary phases directly affects the mechanical properties of the low-density multicomponent systems. Although such systems show higher hardness values around 450 HV, they exhibit lower fracture strength (<500 MPa) and also low ductility (<6 %) [41], [47].

Recently, due to the difficulty to produce HEAs with a single or dual solid solution, a new term so-called complex concentrated alloys (CCAs) [48], [49] is used for the multicomponent system that is not HEA. This term is also used for the LWHEAs because of the ICs forms during the production. Jia et al. [50] designed and produced novel $Al_{19.9}Li_{30}Mg_{35}Si_{10}Ca_5Y_{0.1}$ $Al_{15}Li_{35}Mg_{35}Ca_{10}Si_5$, $Al_{15}Li_{38}Mg_{45}Ca_1Si_1$, $Al_{15}Li_{35}Mg_{48}Ca_{0.5}Si_{1.5}$, and $Al_{15}Li_{39}Mg_{45}Ca_{0.5}Si_{0.5}$ CCAs by induction melting followed by casting into a copper mold. As shown in Figure 2.20 (a), more than four phases coexist in the $Al_{19.9}Li_{30}Mg_{35}Si_{10}Ca_5Y_{0.1}$ CCA. When the atomic amounts of Li and Mg elements were increased systematically, the phases with higher intensities were observed in the CCAs (Figure 2.20 (b-e)). Moreover, the mechanical properties of the CCAs were increased by increasing their Li and Mg content as seen in Figure 2.20 (f) [50]. Although higher yield strength (300 MPa), ductility (>60 %) and a very low density of 1.46 g/cm^3 is achieved for $Al_{15}Li_{39}Mg_{45}Ca_{0.5}Si_{0.5}$ [50], the atomic amount of the elements is far away from the basic definition of the HEAs.

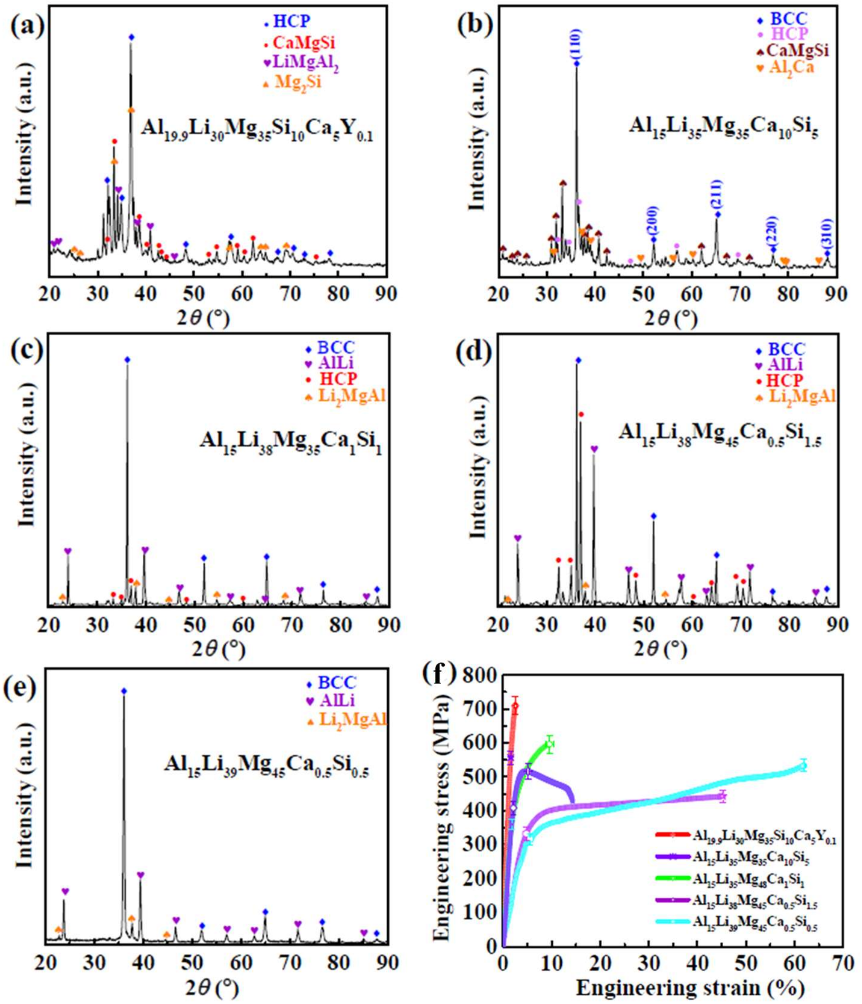

Figure 2.20. XRD patterns of a) $Al_{19.9}Li_{30}Mg_{35}Si_{10}Ca_5Y_{0.1}$, b) $Al_{15}Li_{35}Mg_{35}Ca_{10}Si_5$, c) $Al_{15}Li_{38}Mg_{45}Ca_1Si_1$, d) $Al_{15}Li_{35}Mg_{48}Ca_{0.5}Si_{1.5}$, e) $Al_{15}Li_{39}Mg_{45}Ca_{0.5}Si_{0.5}$; f) The compression stress-strain curves of these CCAs [50]

The results show that the production of LWHEAs with equiatomic or near equiatomic by casting method is a challenging field for HEAs. However, LWHEAs consist of Al-Ti-V-Cr elements that could be easily produced by melting and casting techniques [51]. Qiu et al. produced equiatomic AlTiVCr LWHEA (or MEA) with a density of 5.06 g/cm^3 by arc melting technique. They showed that the LWHEA had a single B2 (ordered BCC) phase in the XRD patterns [51]. The presence of such pure ordered phases in the structure make the metals very brittle with low ductility values [52], [53].

CHAPTER 3

EXPERIMENTAL PROCEDURE

3.1. Introduction

This thesis involves the production of lightweight high entropy alloys (LWHEAs) with robust mechanical properties. It is aimed to produce LWHEAs with sufficiently higher strength values, and lighter as compared to the steel parts used in the automotive industry. The primary critical reference value has been taken as the density of steel parts used in the automotive industry (~7.86 g/cm^3). In this thesis, LWHEA has been called for the HEAs with densities lower than the density of the steel. Another critical criterion for element selection is the cost. In the light of these criteria, the main elements selected in this study are Li, B, Mg, Ti, V, Cr, Mn, Al, and Si. These elements are shown in the Periodic Table in Figure 3.1. Because of the toxicity of Be and high costs of Sc elements, these elements are not considered in the study. At least five principal elements are combined within the range of 5-35 at.% to produce LWHEA solid solution. In the following steps of the study, additional elements such as Cu and Ni are used to produce medium entropy alloys (MEAs) with four principal elements to obtain the desired properties in terms of strength and ductility.

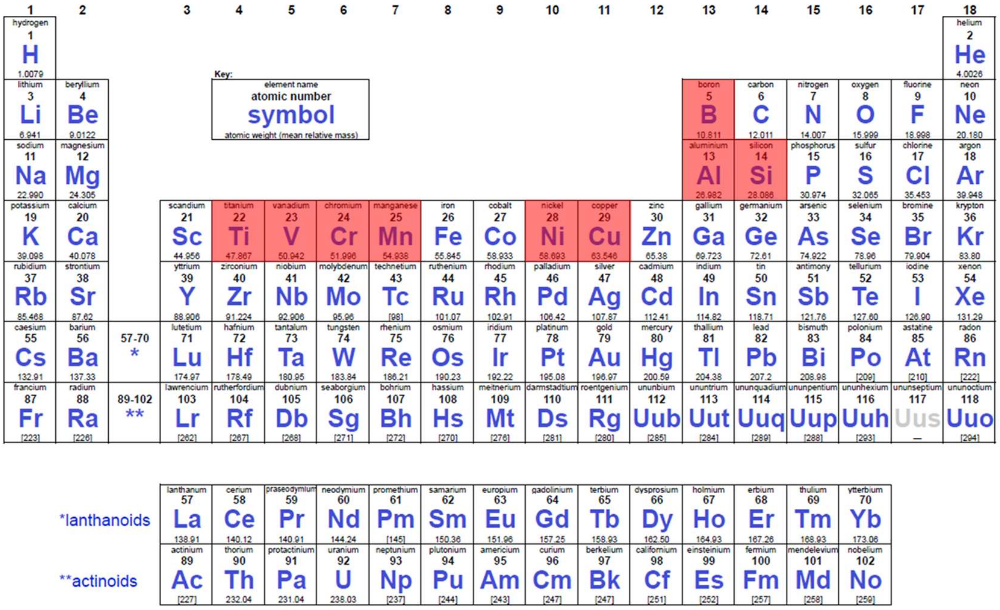

Figure 3.1. The elements used to produce LWHEAs

3.1.1. Design of LWHEA

The main consideration to design new HEAs are the melting temperature, density, and strength of the resultant alloys. After the selection of elements based on these essential criteria, the most critical step is to determine the elements to produce HEA from the selected elements. In this step, empirical calculations and computational methods are used to determine the best combination among the candidate elements and their compositions.

3.1.1.1. Empirical Calculation Methods

The critical thermodynamic parameters used to define the conditions of solid solutions in HEAs are given in Chapter 2. It is obvious that ΔS_{mix} and ΔH_{mix} parameters are two critical factors to predict solid solution formation in a multicomponent system. In addition to these parameters, Yang et al. [54] defined a new parameter, which is **Ω**.

$$\Omega = \frac{T_m \Delta S_{mix}}{|\Delta H_{mix}|} \qquad \text{Equation 3.1}$$

In this equation, T_m is a useful term due to the formation of phases near the melting temperature of the alloys that it is adopted to entropy term. The hypothetical value of Tm is calculated according to the rule of the mixture as shown below [54]:

$$T_m = \sum_{i=1}^{n} c_i \, (T_m)_i \qquad \text{Equation 3.2}$$

In addition to general thermodynamic criteria which are $\Delta S_{mix} > 13.38$ J/ K mol, $\delta < 6.6$ and -10 kJ/mol $< \Delta H_{mix} < 5$ kJ/mol, Ω term is a critical point to predict solid solution formation of a multi-component system. If $\Omega \geq 1.1$, the contribution of T_m ΔS_{mix} will be higher that entropically stabilized alloys could be produced [54]. These empirical calculations are used to design LWHEAs. VEC is tried to arrange higher than 6.87 to avoid the formation of brittle BCC phases. However, when VEC is between 6.87 and 8, FCC+BCC composite phases will occur that a ductile HEA with high strength could be produced. However, the main challenge to obtain FCC phases in LWHEA is low VECs in light elements. Because of this limitation, rather than FCC phases, BCC and FCC+BCC are more probable phases for the LWHEAs. In this manner, the HEAs with BCC and FCC+BCC phases are produced in the present study.

3.1.2. Computational Methods

Because of the limitation in analytical calculations, there is an increasing interest in computational modeling of HEAs. In this respect, Thermo-Calc TCHEA2: TCS High entropy alloy database and MedeA-VASP 5.2 software are used to predict solid solution formation of candidate elements.

3.1.2.1. CALPHAD Simulation

CALPHAD method adopted to Thermo-Calc software with TCHEA2 database is used to predict the phases with respect to composition and temperature. This software makes it possible to estimate the resulting properties from structural and compositional dependence of the HEAs. Therefore, chosen HEAs based on the thermophysical calculations are simulated by Thermo-Calc. An example phase diagram constructed for AlTiVCr HEA by Thermo-Calc software is shown in Figure

3.2. If both thermophysical calculation and Thermo-Calc simulation give the same outputs, the HEAs are simulated by VASP to construct an atomic arrangement in a box.

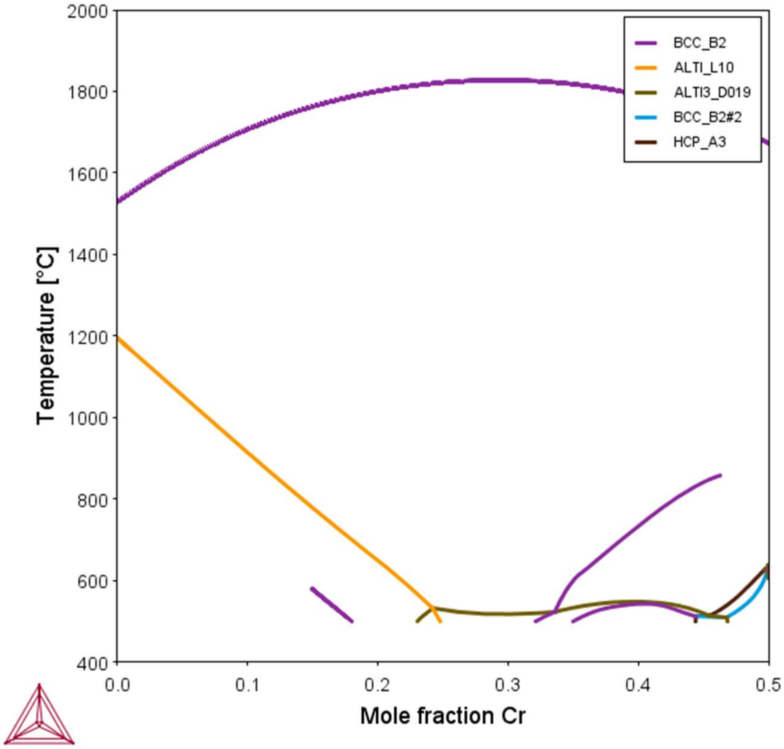

Figure 3.2. A typical example phase diagram for AlTiVCr HEA

3.1.2.2. Vienna Ab initio Simulation Package (VASP) Simulations

VASP is used to determine the properties of the final crystal structures of the alloys after solidification. The software provides a crystal structure under equilibrium conditions that it is performed to predict the final atomic distribution and crystal structure of the HEAs without experimental studies. An output data can be seen in Figure 3.3.

The temperature scale is chosen as a calculation parameter in order to be able to determine the crystal structure and atomic positions when the alloy is solidified from the liquid state to the room temperature. Theoretical melting points are adopted from thermophysical calculations and/or Thermo-Calc results. The initial temperature of the liquid is chosen above 150 K of the exact T_m (T_m+150 K) to ensure the liquid phase. The effects of the magnetic moments of the elements, used in the simulation, on the crystal structure have been underestimated. Default molecular dynamics parameter which is 4.0 femtoseconds is selected as the simulation time interval. If the periods below this value are selected, it would be difficult to find the exact equilibrium phase of the alloys. Therefore, the simulation time periods equal to or above 4.0 femtoseconds should be chosen to have more precise results. However, further increasing the simulation time will increase the total simulation time dramatically. If a box with 500 atoms is chosen, the simulation may take around a month with a very high-performance computer. Thus, 4.0 femtoseconds is chosen as an optimum default simulation time interval in the present study. The number of maximum geometric step is chosen as 30 to find a crystal structure with minimum energy. Although further increasing the simulation step gives more stable phases, it will increase the total simulation time.

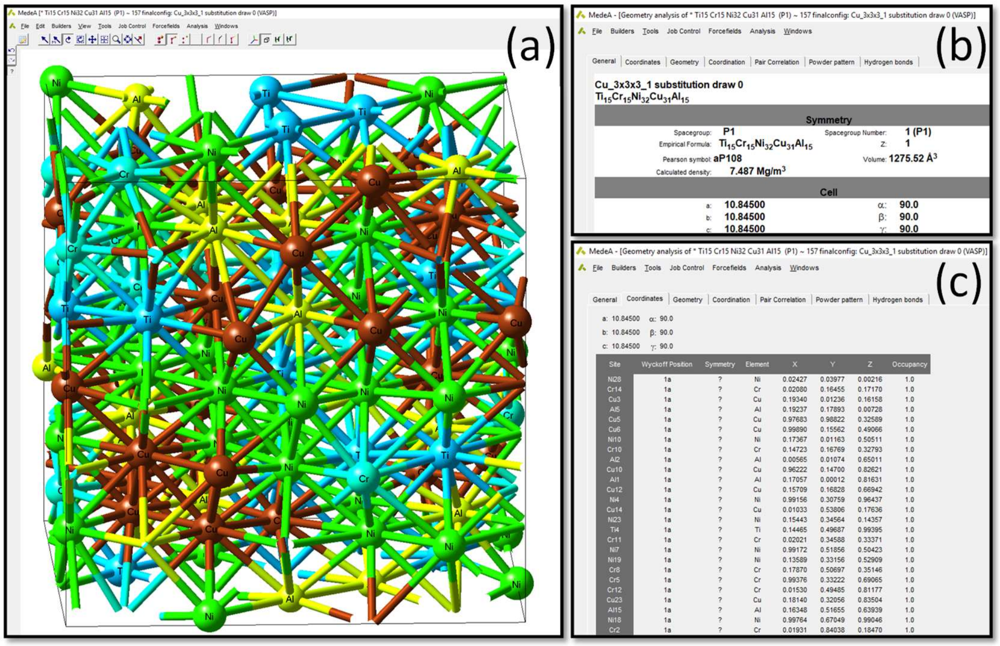

Cu_3x3x3_1 substitution draw 0
$Ti_{15}Cr_{15}Ni_{32}Cu_{31}Al_{15}$

Symmetry

Spacegroup: P1
Spacegroup Number: 1 (P1)
Empirical Formula: $Ti_{15}Cr_{15}Ni_{32}Cu_{31}Al_{15}$
Z: 1
Pearson symbol: aP108
Volume: 1275.52 Å^3
Calculated density: 7.487 Mg/m^3

Cell

a: 10.84500
α: 90.0
b: 10.84500
β: 90.0
c: 10.84500
γ: 90.0

a: 10.84500 α: 90.0
b: 10.84500 β: 90.0
c: 10.84500 γ: 90.0

Site	Wyckoff Position	Symmetry	Element	X	Y	Z	Occupancy
Ni28	1a	?	Ni	0.02427	0.03977	0.00216	1.0
Cr14	1a	?	Cr	0.02080	0.16455	0.17170	1.0
Cu3	1a	?	Cu	0.19340	0.01236	0.16158	1.0
Al5	1a	?	Al	0.19237	0.17893	0.00728	1.0
Cu5	1a	?	Cu	0.97683	0.98822	0.32589	1.0
Cu6	1a	?	Cu	0.99890	0.15562	0.49066	1.0
Ni10	1a	?	Ni	0.17367	0.01163	0.50511	1.0
Cr10	1a	?	Cr	0.14723	0.16769	0.32793	1.0
Al2	1a	?	Al	0.00565	0.01074	0.65011	1.0
Cu10	1a	?	Cu	0.96222	0.14700	0.82621	1.0
Al1	1a	?	Al	0.17057	0.00012	0.81631	1.0
Cu12	1a	?	Cu	0.15709	0.16828	0.66942	1.0
Ni4	1a	?	Ni	0.99156	0.30759	0.96437	1.0
Cu14	1a	?	Cu	0.01033	0.53806	0.17636	1.0
Ni23	1a	?	Ni	0.15443	0.34564	0.14357	1.0
Ti4	1a	?	Ti	0.14465	0.49687	0.99395	1.0
Cr11	1a	?	Cr	0.02021	0.34588	0.33371	1.0
Ni7	1a	?	Ni	0.99172	0.51856	0.50423	1.0
Ni19	1a	?	Ni	0.13589	0.33156	0.52909	1.0
Cr8	1a	?	Cr	0.17870	0.50697	0.35146	1.0
Cr5	1a	?	Cr	0.99376	0.33222	0.69065	1.0
Cr12	1a	?	Cr	0.01530	0.49485	0.81177	1.0
Cu23	1a	?	Cu	0.18140	0.32056	0.83504	1.0
Al15	1a	?	Al	0.16348	0.51655	0.63939	1.0
Ni18	1a	?	Ni	0.99764	0.67049	0.99046	1.0
Cr2	1a	?	Cr	0.01931	0.84038	0.18470	1.0

Figure 3.3. An example screenshot image of MedeA software a) A simulated box consists of 108 atoms, b) Symmetry and cell parameters, c) Atomic coordinates

The most promising LWHEAs are identified by using computational methods. Afterward, the selected alloys are produced experimentally to compare the theoretical and experimental results of LWHEAs.

3.2. Production Methods

LWHEAs are produced using high purity raw materials (≥99.9 at.%) in the form of pieces and shots by mixing appropriate amounts of the elements identified by the thermophysical calculations and computational methods. The accuracy of the composition has significant importance for HEAs. Because of this reason, each element has been weighted carefully with at least three digits and then they are combined for alloying. Two major production methods are used in the present study; arc melting and induction melting techniques.

3.2.1. Arc-Melting

The selected LWHEAs are prepared by arc melting of pure elements in a high-purity argon atmosphere to avoid the oxidation. Edmund Bühler Arc-melter MAM-1 is used with the suction casting stage as shown in Figure 3.4 (a-c). This system is the most proper technique to produce alloys with small amounts of raw materials for preliminary experiments. The torch temperature of the system is 3500 °C that lets us melt the elements with higher melting points. This temperature could be arranged by tuning the applied voltage. Low voltages are used for elements with low melting points and it is increased with increasing melting points of the elements.

In this technique, the melting chamber is flashed by argon gas to remove the air present in the chamber. This procedure repeated three times. Then, the alloys are re-melted at least three times and reversed for each step to ensure chemical homogeneity. Finally, a homogenous alloy with around 2 gr weight is obtained for suctions casting. Suction casting stage is combined with the melting stage in this device as seen in Figure 3.4 (b). The suction stage and copper mold are cooled with water that the effect of cooling rates on the alloys could be investigated. Also, the diameter of copper molds in Figure 3.4 (c) changes from 1 mm to 5 mm with 0.5 intervals that the cooling rates decrease with increasing diameters. Therefore, rapidly solidified samples can be produced by using the molds with smaller diameters. When the molds are filled with the alloy, samples up to 30 mm height and 1-5 mm diameters could be produced.

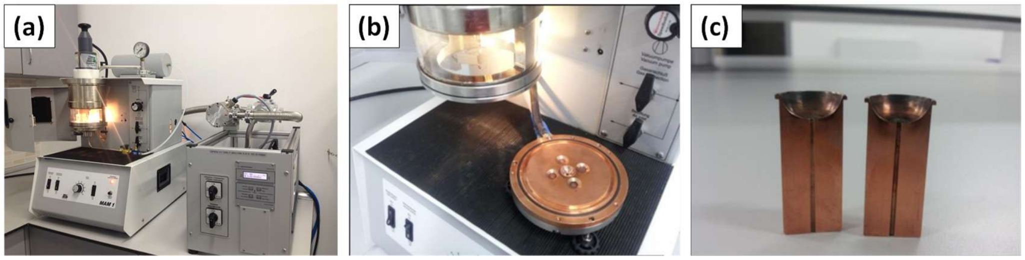

Figure 3.4. a) Edmund Bühler Arc-melter MAM-1, b) Suction casting stage, c) Cylindrical copper mold

3.2.2. Induction Casting

The capacity of the arc-melter is deficient that only subsize samples could be produced by this method. Moreover, the high torch temperature may not be suitable for elements with low melting points because of the vaporization problem. In this case, induction melting is the most proper technique to overcome these challenges. Indutherm MC 15+ induction melting device (Figure 3.5 (a)) is used in the experiments to produce the most promising LWHEA. The temperature of the device to melt the elements could be arranged by tuning the power applied to the system. The melting process is carried out under a high purity argon atmosphere. During the melting process, the melt is also stirred by the magnetic field that it leads to obtain chemically homogenized alloy with just one step. The melted alloys are cast into a copper mold (Figure 3.5 (b)) with a 5 mm diameter and 80 mm height. The final sizes of the samples produced by the induction casting technique are sufficiently large that it will be easier to investigate HEAs mechanically.

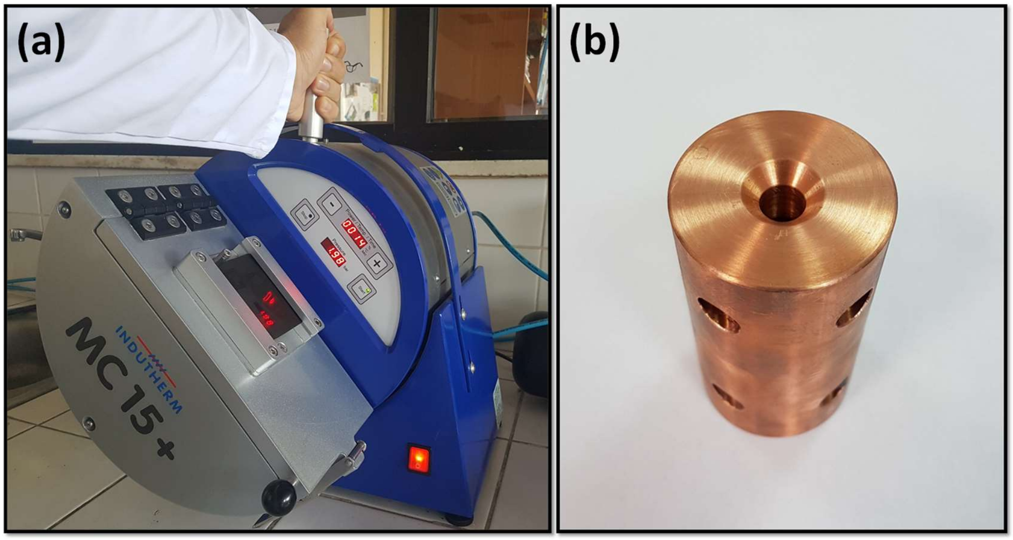

Figure 3.5. a) MC 15 Induction melter, molds adapted to the melter, b) copper mold

3.2.3. Heat Treatment

The as-cast LWHEAs are homogenized in a tube furnace up to 1150 °C under vacuum (~10^{-2} mbar pressure) followed by furnace cooling. The homogenization temperature and period are chosen based on the Thermo-Calc results, and similar studies reported in the literature.

3.3. Characterization Techniques

3.3.1. X-ray Diffraction (XRD)

The structure of the samples is identified by XRD technique. It is the most critical step of characterization for the present study. The samples are determined whether they have solid solution HEA phases or not. If the samples contain single or dual solid solution phases, detailed analyses are performed. First of all, Rigaku D/Max-2200 diffractometer with Cu-K_α radiation of a wavelength of 1.54056 Å is used to determine phases. Data are collected between 10° and 100° with 2°/min scanning rate and 0.02° step size. Also, in-situ high-temperature XRD (HT-XRD) analysis are performed by Anton Paar HTK 16N High-Temperature Chamber adopted to Rigaku D/Max-2200 diffractometer. The XRD equipment does not have a monochromator optic device and hence the K_α-2 diffractions are suppressed by DIFFRAC.EVA software.

3.3.2. Electron Microscopy

SEM micrographs are used to determine the morphology and distributions of the phases in the samples. Also, Energy Dispersive X-ray Spectrometry (EDS) analysis is applied to check the chemical composition of the samples. FEI 430 NanoSEM-30 kV Field Emission Scanning Electron Microscope (FESEM) equipped with an energy dispersive X-ray spectrometer (EDAX SSD Apollo10 Detector) is used for the microstructural and elemental examination. For SEM investigation, samples are ground up to 2000 grit Si papers then polished with 6 and 1-micron diamond paste, respectively. Polished samples are etched in the aqua regia (a mixture of HNO_3 and HCl in a molar ratio of 1:3) between 15 and 120 seconds.

The selected samples are investigated by JEOL JEM-2100F 200 kV Transmission Electron Microscope (TEM). The samples are prepared through Focus Ion Beam (FIB) microscope technique to be investigated under TEM.

3.3.3. Mechanical Testing

The room temperature compression tests of the as-cast and homogenized alloys are investigated by Instron 5582 universal testing machine. The test performed according to ASTM E9-09 standards (Standard Test Methods of Compression Testing of Metallic Materials at Room Temperature) with 10^{-4} strain rate. The cylindrical samples with 3 and 4 mm diameter are subjected to the mechanical test. At least 3 samples are used for each set of the test to increase the accuracy of the tests. The yield stresses are determined by taking into account the offset yield point (proof stress) as 0.2 %.

A high-speed tabletop precision cutter is used to arrange the sample sizes for the compression test, followed by grinding. The top and bottom of the samples are well parallelized that require for the test.

3.3.4. Microhardness Measurements

The hardnesses of the specimens are measured from side to side with the Vickers microhardness (HV) test. Shimadzu-2 Micro Hardness Tester with a diamond pyramid indenter is used under 4.903 N (0.5 kgf) force. The mean hardness values are taken by averaging at least 6 measurements on each sample.

CHAPTER 4

DESIGN AND PRODUCTION OF HEAs CONSIST OF LOW DENSITY ELEMENTS

In this chapter, studies regarding to novel LWHEAs are represented. The LWHEAs are designed based on the thermophysical calculation and VASP simulations. The LWHEAs are produced by casting and detailed structural and mechanical characterization are performed on the samples.

4.1. Design and Characterization of AlTiVCrMnBx (x = 0, 0.3, 0.6, 1.0) LWHEAs

The elements are initially chosen based on density, abundance and costs. As a result, AlTiVCrMn has been chosen as a precursor LWHEA. Boron (B) element is gradually added (from 0 to 1.0) to AlTiVCrMn LWHEA to investigate the effect of B on the properties of the LWHEA. At first, the thermophysical parameters of the LWHEAs are calculated and shown in Table 4.1. Although B addition decreases the density of the LWHEA from 5.34 g/cm^3 to 5.06 g/cm^3, a dramatic increase in δ is observed from 4.53 (%) to 12.11 (%). The lower atomic radius of B (87 pm) compare to Al (118 pm), Cr (166 pm), V (171 pm), Si (111 pm) and Mn (161 pm) atoms causes the increase of δ parameter. As previously stated in literature [55], [5], if the δ parameter is higher than 6.6 (%) value single or dual solution HEAs are not expected. Also, large negative ΔH_{mix} values are seen with increasing atomic amount of B. This situation promotes the formation of intermetallic compounds (ICs). ΔS_{mix} of the system increases with increasing B content due to increasing type and number of atoms affecting the entropy of the system [7]. However, ΔS_{mix} of the LWHEAs are equal or higher than the theoretical lower limit of ΔS_{mix} [7] (13.38 kJ/mol.K) to be defined as a HEA. Further increase in ΔS_{mix} does not have a dramatic effect to produce HEAs. The VEC value of the alloys decreases from 5 to 4.67 with increasing B content due to lower individual VEC value of B atoms. If the VEC value of the system is lower than 6.87, it promotes the formation of HEA with BCC phases [17]. Therefore, the expected dominant phase is BCC for the AlTiVCrMn LWHEAs consist of B. The increasing amounts of B in the alloy prevent the formation of a single BCC phase and promote ICs formation along with BCC phase due to the higher atomic size differences.

Table 4.1. Thermophysical calculations of LWHEAs consist of Al, Ti, V, Cr, Mn and B elements

LWHEAs	Density (g/cm^3)	δ (%)	ΔH_{mix} (kJ/mol)	VEC	ΔS_{mix} (kJ/mol.K)	T_m (K)
AlTiVCrMn	5.34	4.53	-14.88	5	13.38	1735
$AlTiVCrMnB_{0.1}$	5.31	6.05	-34.66	4.96	13.92	1751
$AlTiVCrMnB_{0.3}$	5.25	8.13	-33.07	4.89	14.43	1782
$AlTiVCrMnB_{0.6}$	5.16	10.22	-30.92	4.79	14.78	1825
AlTiVCrMnB	5.06	12.11	-28.44	4.67	14.9	1874

VASP simulation of AlTiVCrMnB LWHEA is shown in Figure 4.1. The simulation initiated just above the melting point of the system (T_m+50 K) and cooled down to room temperature. The final simulation box is shown in Figure 4.1 (a). The corresponding XRD pattern of the box shown in Figure 4.1 (b) is simulated based on the atomic positions of each atom in the box and the simulated XRD pattern consists of BCC and ICs. The simulation outputs reveal that there is a well agreement between thermophysical calculations and VASP simulation in terms of the phases of the LWHEA.

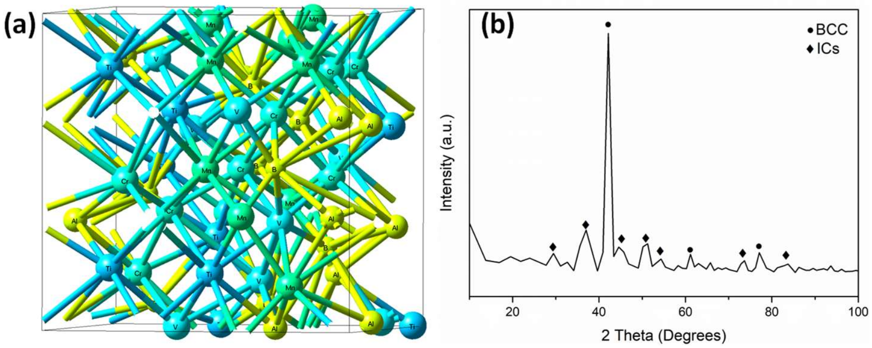

Figure 4.1. VASP simulation of AlTiVCrMnB LWHEA a) 3x3x3 simulation box, b) Simulated XRD pattern based on the atomic position in the box

The simulated AlTiVCrMnB$_X$ (x = 0, 0.3, 0.6, 1.0) LWHEAs are then produced by arc melting and suction casting method with 3 mm cylindrical copper mold. XRD patterns of the cylindrical LWHEAs with 3 mm diameters are shown in Figure 4.2. It is seen in the figure that AlTiVCrMn LWHEA has a pure BCC crystal structure. However, minor ICs form together with the main BCC phase with the addition of B. The XRD patterns of the LWHEAs well agree with the predicted phases from thermophysical calculations (Table 4.1).

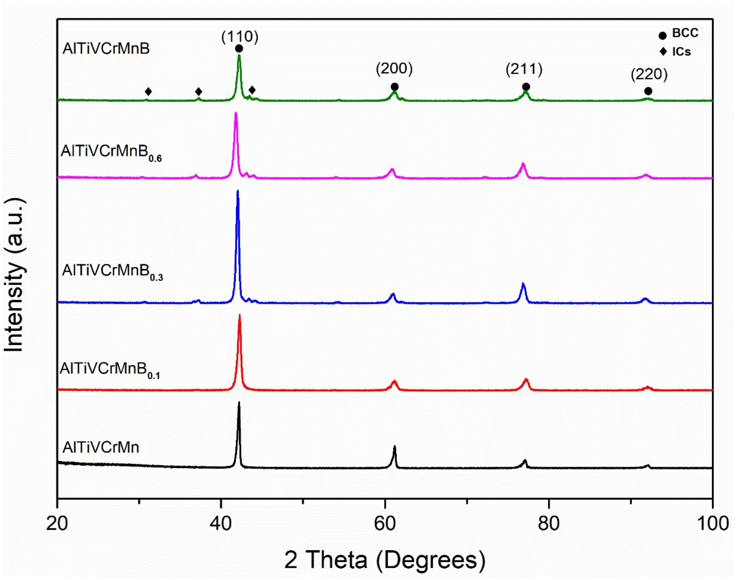

Figure 4.2. XRD patterns of AlTiVCrMnB$_X$ (x = 0, 0.3, 0.6, 1.0) LWHEAs

Vickers hardness values of AlTiVCrMnB$_x$ (x = 0, 0.3, 0.6, 1.0) LWHEAs are shown in Figure 4.3. It is seen from the XRD patterns (Figure 4.2), AlTiVCrMnB$_X$ (x = 0, 0.3, 0.6, 1.0) LWHEAs have a dominant ordered BCC (B2) phase with its characteristic (100) reflection and ICs. The nature of the B2 phases is very hard and brittle. The ductility of these phases is limited as compared to disordered solid solution phases [56]–[58]. Also, disordered BCC solid solutions have relatively higher hardness and lower ductility because of the small number of slip systems in BCC [59]. Therefore, the presence of ordered and disordered BCC phases deteriorates the mechanical properties and causes brittleness in the HEAs. A similar trend can be seen for the ICs. As seen in Figure 4.2, the amount of ICs increase with increasing B content in AlTiVCrMnB$_x$ LWHEAs. The effect of both B2 and ICs cause increasing brittleness and hardness in the LWHEAs. The effect of increasing ICs on hardness is shown in Figure 4.3. The hardness of the LWHEAs increases from 564 (±4) HV to 901 (±11) HV with increasing B content. The increasing hardness values can be also attributed to the increasing lattice distortion in the LWHEAs with higher B content. It is seen from thermophysical calculations (Table 4.1) that the increasing B content also increases the atomic size difference of the lattice that causing higher lattice distortion, gradually. In the case of higher atomic size differences, the atoms are pinned in their preferred lattice site that causes lower energy levels in the lattice. Also, each solute atom in the lattice acts as an obstacle for the dislocation movement [62]. These effects result in an increase in resistance to plastic deformation and higher hardness values.

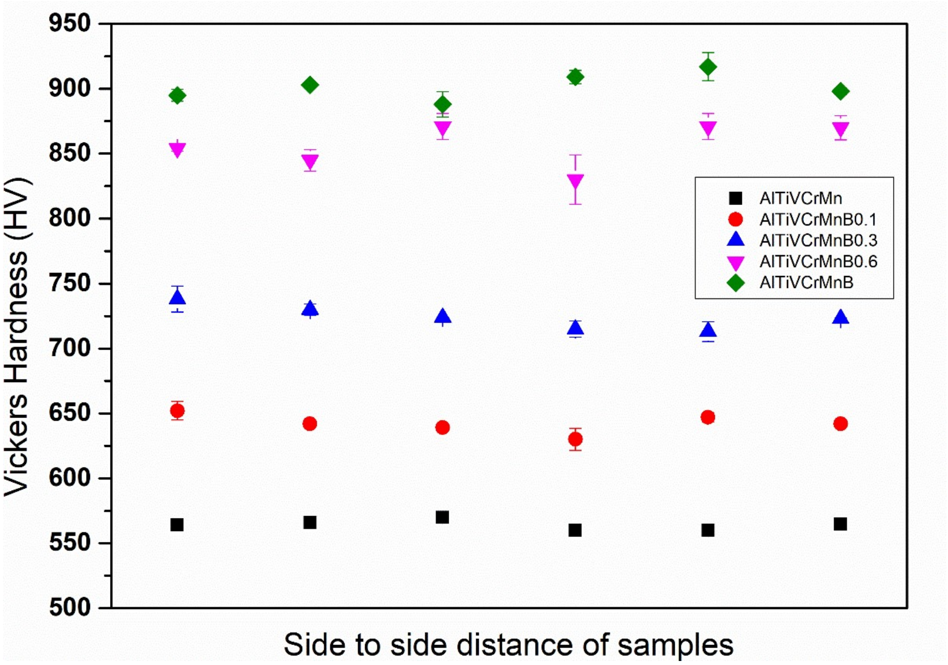

Figure 4.3. Hardness values of AlTiVCrMnB$_X$ (x = 0, 0.3, 0.6, 1.0) LWHEAs

4.2. Design and Characterization of AlTiVCrSi and AlTiVCrMnSi LWHEAs

Thermophysical properties of the AlTiVCrB, AlTiVCrSi, and AlTiVCrMnSi HEAs designed among low-density elements are shown in Table 4.2. The densities of these HEAs are between 4.26 and 4.68 g/cm^3 and they can be called LWHEAs.

Table 4.2. Thermophysical calculations of AlTiVCrB, AlTiVCrSi and AlTiVCrMnSi LWHEAs

LWHEAs	Density (g/cm^3)	δ (%)	ΔH_{mix} (kJ/mol)	VEC	ΔS_{mix} (kJ/mol.K)	T_m (K)	Expected Crystal Structure
AlTiVCrB	4.62	13.27	-31.68	4.2	13.38	1946	BCC
AlTiVCrSi	4.26	4.82	-37.92	4.4	13.38	1768	BCC
AlTiVCrMnSi	4.68	4.45	-34.22	4.83	14.9	1726	BCC

XRD patterns of AlTiVCrB, AlTiVCrSi and AlTiVCrMnSi LWHEAs produced by arc melting are given in Figure 4.4. It is seen in the figure that the dominant phase in the LWHEAs is BCC and increasing amount of Si in the LWHEAs promotes the formation of ICs. Although texture can be an effective parameter on the intensities of the peaks, the general trend shows that replacement B with Si in the AlTiVCrB LWHEA causes a relative increase in the intensities of ICs as seen in Figure 4.4. This situation well agrees with the thermophysical calculations given in Table 4.2 when B is replaced with Si in AlTiVCrB LWHEA, ΔH_{mix} value decreases from -31.68 kJ/mol to -37.92 kJ/mol. It is known that larger negative ΔH_{mix} values promote the formation of ICs [15]. Also, the addition of Si causes B2 phase formation (BCC-2) in the alloy.

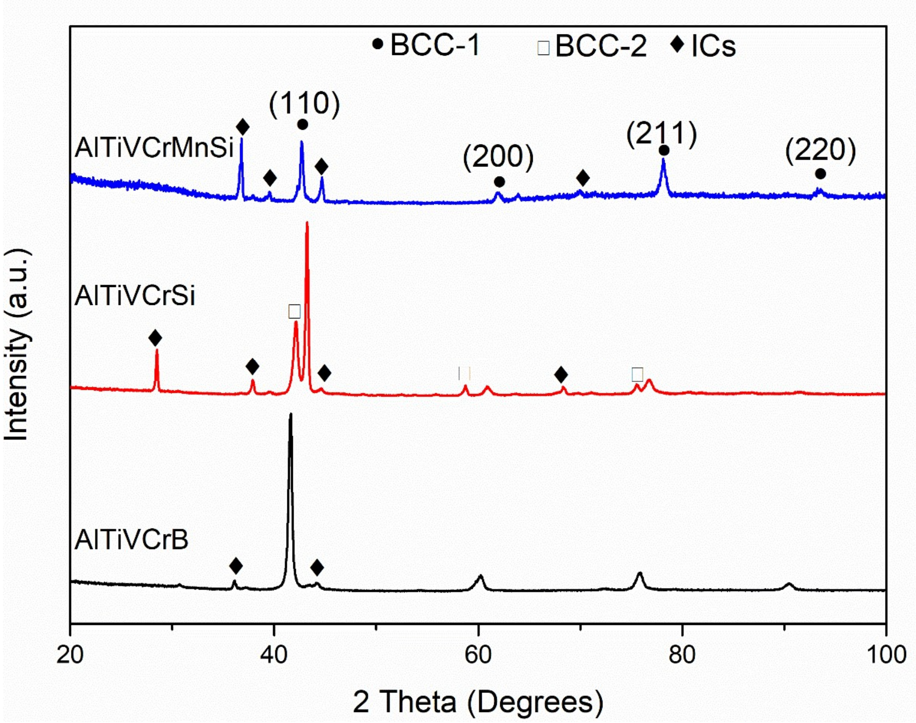

Figure 4.4. XRD patterns of AlTiVCrB, AlTiVCrSi, and AlTiVCrMnSi LWHEAs

When equiatomic Mn added to AlTiVCrSi LWHEA the relative intensities of ICs increase for AlTiVCrMnSi LWHEA as seen in Figure 4.4. The thermophysical parameters of AlTiVCrMnSi are given in Table 4.2. The atomic size difference (δ %)

is higher than the 6.6 limit of HEA formation region [60]. Also, similar to AlTiVCrSi LWHEA, AlTiVCrMnSi LWHEA has larger negative ΔH_{mix} value that increases the formation of ICs. Guo et al. [9] pointed out that, although solid solution phases form either slightly positive or insignificantly negative ΔH_{mix}, ICs can form in the intermediate conditions.

Table 4.3. EDS analyses of AlTiVCrSi, AlTiVCrMnSi and AlTiVCrB LWHEAs

LWHEAs	**at. %**						
	Al	**Ti**	**V**	**Cr**	**Mn**	**Si**	**B**
AlTiVCrSi	19.7	20.2	19.3	19.5	-	21.3	-
AlTiVCrMnSi	14.5	16.5	17.1	17.6	17.4	16.9	-
AlTiVCrMnB	16.5	17.6	17.1	16.7	15.5	-	Balance

Energy dispersive spectroscopy (EDS) analysis of AlTiVCrB, AlTiVCrSi and AlTiVCrMnSi LWHEAs produced by arc melting are given in Table 4.3. The amount of B in AlTiVCrB LWHEA could not be measured due to its lower atomic number [61]. On the other hand, B peak is seen in the EDS spectrum as shown in Figure 4.5.

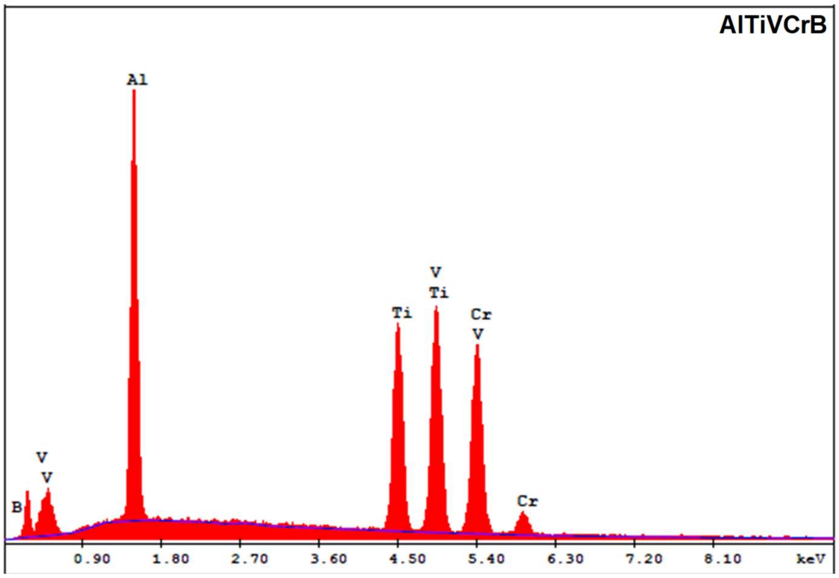

Figure 4.5. EDS spectrum of AlTiVCrB LWHEAs

As seen in Table 4.3, the final composition of AlTiVCrSi and AlTiVCrMnSi LWHEAs slightly deviate as compared to their initial state. However, these differences in the composition do not significantly affect the properties of the LWHEAs. Thermophysical properties of the LWHEAs are calculated based on the EDS analyses (Table 4.3) to verify this situation. The overall EDS analysis of the AlTiVCrSi and AlTiVCrMnSi LWHEAs corresponds to $Al_{19.7}Ti_{20.2}V_{19.3}Cr_{19.5}Si_{21.3}$ and $Al_{14.5}Ti_{16.5}V_{17.1}Cr_{17.6}Mn_{17.4}Si_{16.9}$, respectively. When the initial thermophysical properties of designed LWHEAs (Table 4.2) and the corresponding alloys produced by arc melting (Table 4.4) are compared, negligible differences are seen for all the calculations. These minor differences do not affect the expected crystal structure and phases in the LWHEAs.

Table 4.4. Thermophysical calculations of AlTiVCrSi and AlTiVCrMnSi LWHEAs based on the EDS analyses

LWHEAs	Density (g/cm^3)	δ (%)	ΔH_{mix} (kJ/mol)	VEC	ΔS_{mix} (kJ/mol.K)	T_m (K)	Expected Crystal Structure
$Al_{19.7}Ti_{20.2}V_{19.3}Cr_{19.5}Si_{21.3}$	4.22	4.83	-39.05	4.39	13.38	1765	BCC
$Al_{14.5}Ti_{16.5}V_{17.1}Cr_{17.6}Mn_{17.4}Si_{16.9}$	4.76	4.43	-33.94	4.9	14.88	1747	BCC

Scanning electron microscope (SEM) secondary electrons (SE) images of AlTiVCrB, AlTiVCrMnB, AlTiVCrSi, AlTiVCrMnSi LWHEAs are shown in Figure 4.6 and it is seen from XRD patterns of the LWHEAs (Figure 4.4) that they have ICs besides BCC solid solution phase. The main matrix phase of the AlTiVCrB LWHEA shows bright flower-like BCC dendrites (bright regions) and a small amount of ICs (dark regions) that distributed in the matrix as seen in Figure 4.6 (a). In the AlTiVCrMnB LWHEA, microstructure has high amounts of sharp phases (gray regions) and intergrain phases (dark regions) as shown in Figure 4.6 (b). It is known from the XRD pattern of AlTiVCrMnB LWHEA (Figure 4.4) that the alloy has mainly B2 phase with minor ICs. Therefore, the gray regions correspond to B2 phases whereas dark ones are ICs due to the low amount of dark regions. Similar microstructures are observed for

AlTiVCrSi (Figure 4.6 (c)) and AlTiVCrMnSi (Figure 4.6 (d)) LWHEAs. It is known from XRD patterns of the LWHEAs (Figure 4.4) that they have additional ICs and B2 structure in the matrix besides the disordered BCC phase. However, it is not possible to label each phase present in the alloys from the SEM images. An assumption can be done for the dark regions that the small amount of these regions may correspond to the BCC patterns which have smaller relative intensities as seen in Figure 4.4.

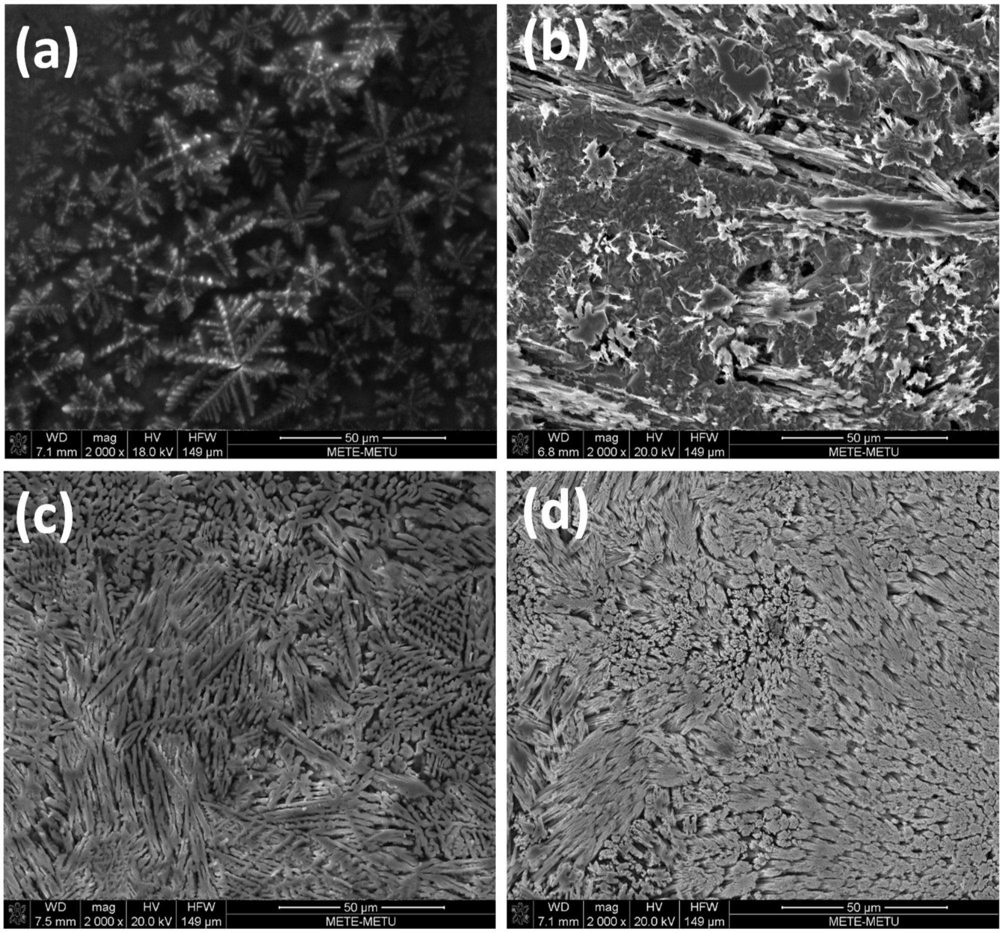

Figure 4.6. SEM images of as-cast LWHEAs (2000x) a) AlTiVCrB, b) AlTiVCrMnB, c) AlTiVCrSi, d) AlTiVCrMnSi

4.3. Design and Characterization of AlTiVCrMn, $Al_{35}Ti_{35}V_{20}Cr_5Mn_5$ and $Al_5Ti_5V_{20}Cr_{35}Mn_{35}$ LWHEAs

The LWHEAs consist of Al, Ti, V, Cr, and Mn are chosen in terms of density and thermophysical properties to produce LWHEAs with a single/dual solid solution. Our previous simulations and results show that AlTiVCrMn LWHEA has a single solid solution with a BCC crystal structure with a density of 5.34 g/cm^3. Therefore, this LWHEA is termed as LWHEA due to its unique structure and density. Also, the atomic amounts of Al, Ti, V, Cr, and Mn are changed to have lower and higher density limits under HEA formations criteria. Thus, $Al_{35}Ti_{35}V_{20}Cr_5Mn_5$ and $Al_5Ti_5V_{20}Cr_{35}Mn_{35}$ LWHEAs are designed with densities of 4.34 g/cm^3 and 6.57 g/cm^3, respectively. Thermophysical calculation results of the LWHEAs are given in Table 4.5. All the results are in the limit parameters [62] to form a solid solution for HEAs. VEC values of AlTiVCrMn, $Al_{35}Ti_{35}V_{20}Cr_5Mn_5$ and $Al_5Ti_5V_{20}Cr_{35}Mn_{35}$ LWHEAs are between 4.1 and 5.9. Therefore, the expected crystal structure of the LWHEAs is BCC due to their relatively low VEC values (<6.87).

Table 4.5. Thermophysical calculations of AlTiVCrMn, $Al_{35}Ti_{35}V_{20}Cr_5Mn_5$ and $Al_5Ti_5V_{20}Cr_{35}Mn_{35}$ LWHEAs

LWHEAs	Density (g/cm^3)	δ (%)	ΔH_{mix} (kJ/mol)	VEC	ΔS_{mix} (kJ/mol.K)	T_m (K)	Expected Crystal Structure
AlTiVCrMn	5.34	4.53	-14.88	5	13.38	1735	BCC
$Al_{35}Ti_{35}V_{20}Cr_5Mn_5$	4.34	3.96	-22.92	4.1	11.28	1618	BCC
$Al_5Ti_5V_{20}Cr_{35}Mn_{35}$	6.57	3.2	-3.96	5.9	11.28	1852	BCC

VASP simulations of AlTiVCrMn, $Al_{35}Ti_{35}V_{20}Cr_5Mn_5$ and $Al_5Ti_5V_{20}Cr_{35}Mn_{35}$ LWHEAs are shown in Figure 4.7, Figure 4.8, and Figure 4.9, respectively. VASP with molecular dynamics (MD) module is used in MedeA interface for these simulations. The initial temperatures of the simulations are chosen just above the melting points (in liquid phase) of the LWHEAs and they solidified to room temperature (298 K). Final atom positions are revealed for each LWHEA and the XRD patterns are simulated based on these atom positions. Simulated XRD patterns of AlTiVCrMn, $Al_{35}Ti_{35}V_{20}Cr_5Mn_5$ and $Al_5Ti_5V_{20}Cr_{35}Mn_{35}$ LWHEAs are shown in Figure 4.7 (c), Figure 4.8 (c), and Figure 4.9 (c), respectively. It is seen in the simulated XRD patterns that the final crystal structure of the LWHEAs is BCC. These results well agree with the phases predicted from thermophysical results (Table 4.5).

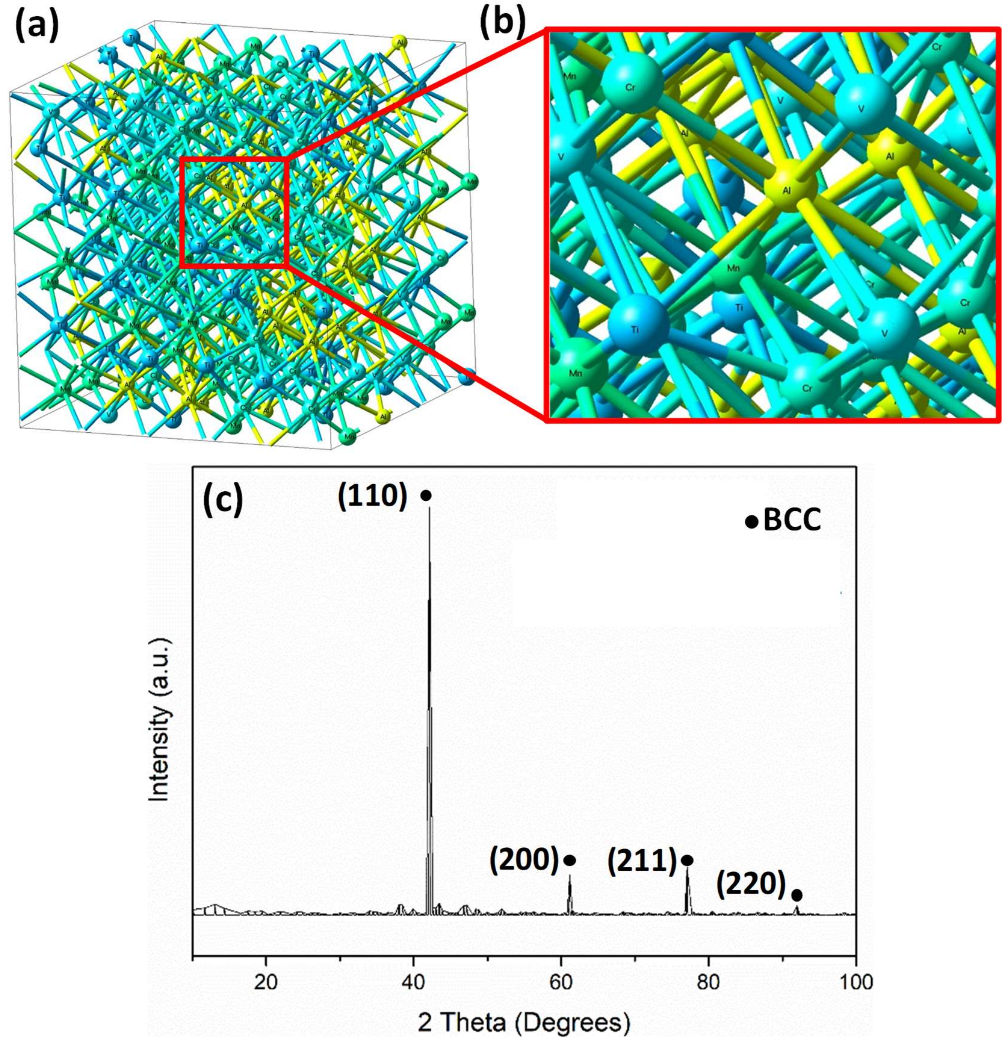

Figure 4.7. VASP simulation of AlTiVCrMn LWHEA; a) 4x4x4 simulation box, b) Zoom-in view of BCC crystal structure, c) Simulated XRD pattern based on atom positions obtained from VASP simulation

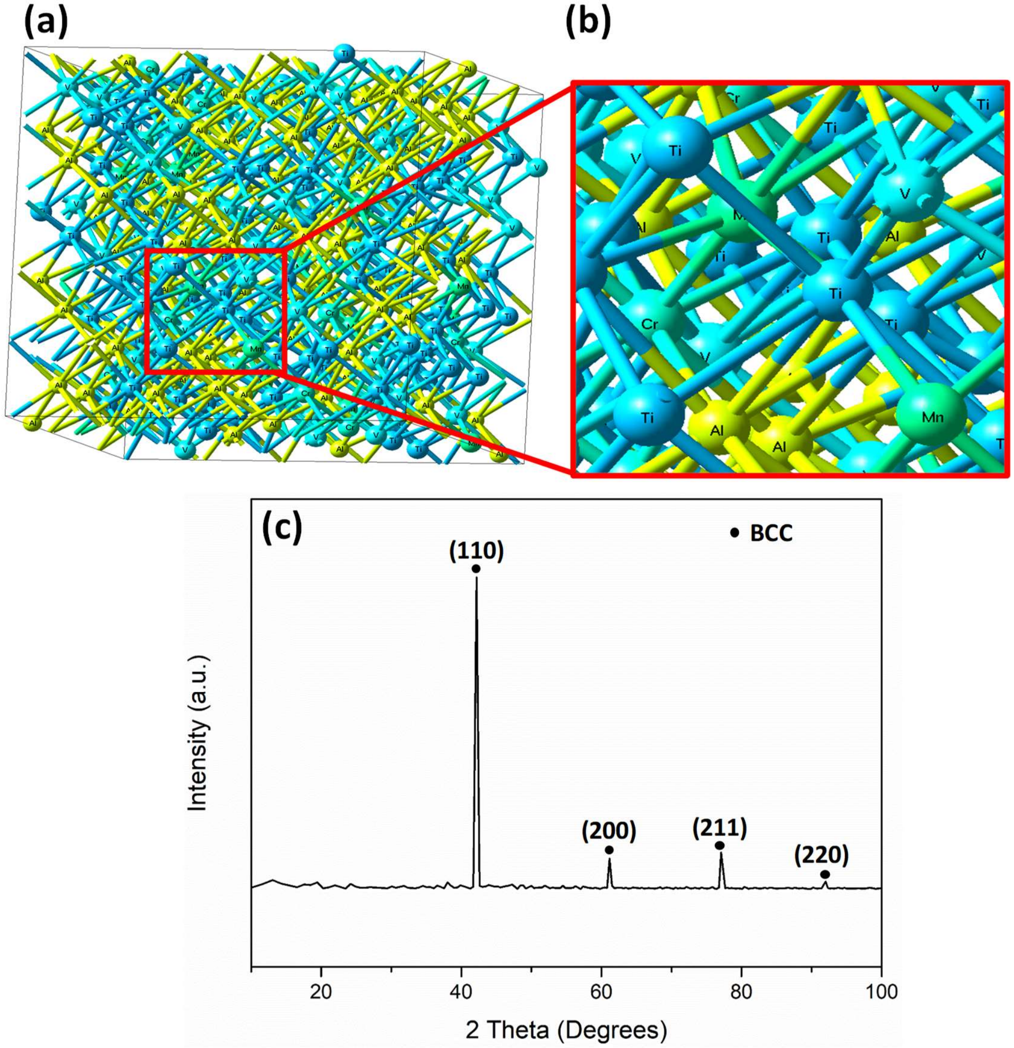

Figure 4.8. VASP simulation of $Al_{35}Ti_{35}V_{20}Cr_5Mn_5$ LWHEA; a) 4x4x4 simulation box, b) Zoom-in view of BCC crystal structure, c) Simulated XRD pattern based on atom positions obtained from VASP simulation

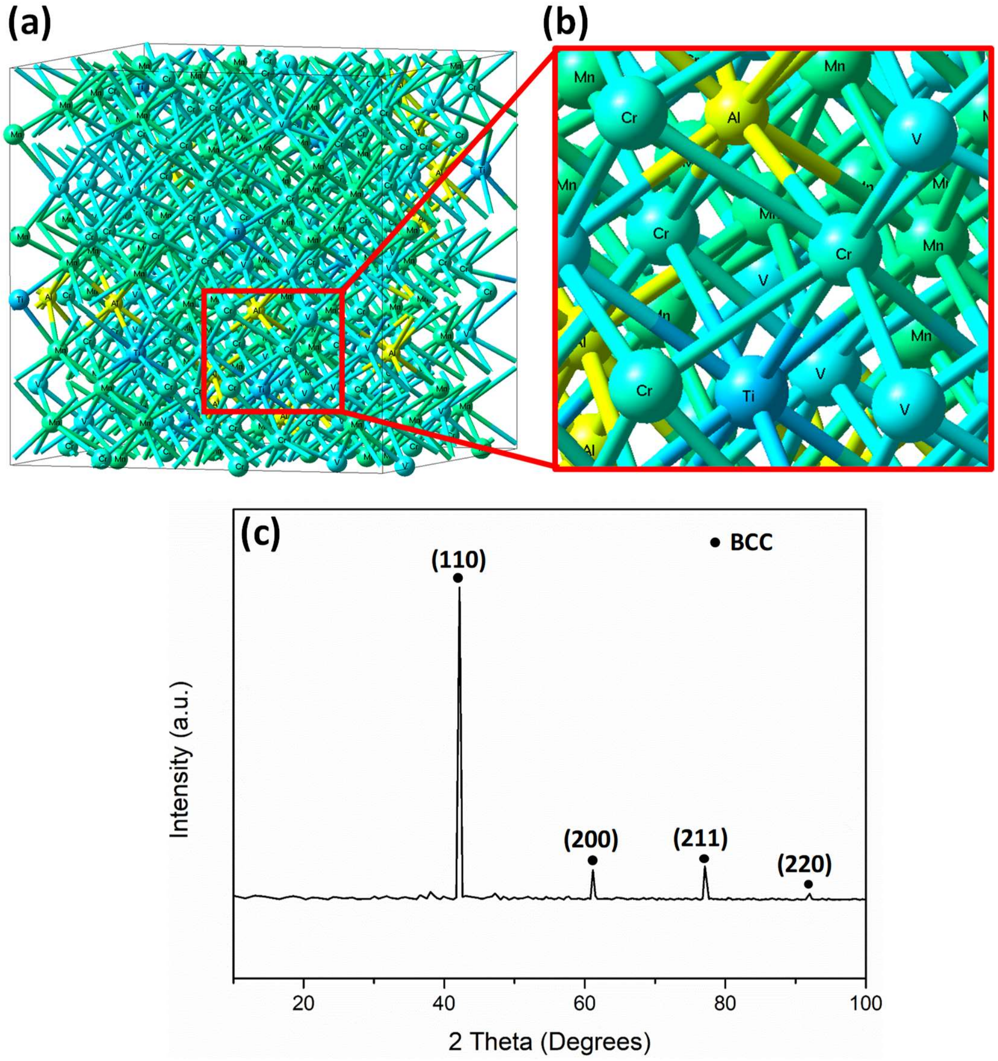

Figure 4.9. VASP simulation of $Al_5Ti_5V_{20}Cr_{35}Mn_{35}$ LWHEA; a) 4x4x4 simulation box, b) Zoom-in view of BCC crystal structure, c) Simulated XRD pattern based on atom positions obtained from VASP simulation

The thermophysical calculations and VASP simulation show that AlTiVCrMn, $Al_{35}Ti_{35}V_{20}Cr_5Mn_5$, and $Al_5Ti_5V_{20}Cr_{35}Mn_{35}$ LWHEAs are proper candidates to produce LWHEAs with single solid solutions (BCC) and low density to achieve the goals of the study. Therefore, these LWHEAs are chosen to produce and investigate experimentally. The LWHEAs are produced by arc melting and suction casting. A cylindrical copper mold with 4 mm diameter is used to produce samples with a cylindrical shape. The melting voltages are arranged to the low values to suppress the possible vaporizations of the pure elements. Also, the melting processes are performed under positive argon pressures to minimize the vaporizations. EDS analysis results of the LWHEAs are shown in Table 4.6.

Table 4.6. EDS analyses of AlTiVCrMn, $Al_{35}Ti_{35}V_{20}Cr_5Mn_5$, and $Al_5Ti_5V_{20}Cr_{35}Mn_{35}$ LWHEAs

LWHEAs	**at. %**				
	Al	**Ti**	**V**	**Cr**	**Mn**
AlTiVCrMn	21.1	21	20	19.4	18.4
$Al_{35}Ti_{35}V_{20}Cr_5Mn_5$	34.6	36.6	20	4.4	4.5
$Al_5Ti_5V_{20}Cr_{35}Mn_{35}$	4.8	5.4	20.1	34.8	34.9

As seen in Table 4.6, final compositions of AlTiVCrMn, $Al_{35}Ti_{35}V_{20}Cr_5Mn_5$, and $Al_5Ti_5V_{20}Cr_{35}Mn_{35}$ LWHEAs slightly deviate as compared to the initial alloy compositions. However, it is known that approximately 1-5 % of deviations in EDS is acceptable for this technique [63]. Also, Mn may oxidize [64] even at low oxygen pressures that may decrease Mn amount in the final alloy. Even so, the EDS analysis results of the LWHEAs are very close to the initial alloy compositions. These minor deviations may not affect the phases and properties of LWHEAs significantly. It is known that the formation of single solid solution phases may lie in a large field on the phase diagrams [24]. Thus, the same solid solution phases can be observed in some LWHEAs even for the minor deviations in the final compositions.

XRD patterns of AlTiVCrMn, $Al_{35}Ti_{35}V_{20}Cr_5Mn_5$, and $Al_5Ti_5V_{20}Cr_{35}Mn_{35}$ LWHEAs are seen in Figure 4.10. These LWHEAs have BCC phases without any secondary phases. The positions (diffraction angles) of AlTiVCrMn and $Al_{35}Ti_{35}V_{20}Cr_5Mn_5$ LWHEAs are very close to each other and they have lattice parameters with 3.035 Å, 3.033 Å, respectively. These experimental lattice parameters are very close to the theoretical lattice parameters obtained from VASP simulations (Figure 4.7 and Figure

4.8). However, the diffraction angles of $Al_5Ti_5V_{20}Cr_{35}Mn_{35}$ shift to the right-hand side as compared to the other LWHEAs. This means that the lattice shrinkage occurs in $Al_5Ti_5V_{20}Cr_{35}Mn_{35}$ LWHEA because of the smaller atomic radii of Cr and Mn atoms in the alloy. Thus, the lattice parameter of $Al_5Ti_5V_{20}Cr_{35}Mn_{35}$ LWHEA decreases to 2.922 Å due to the high amounts of Cr and Mn elements in the alloy.

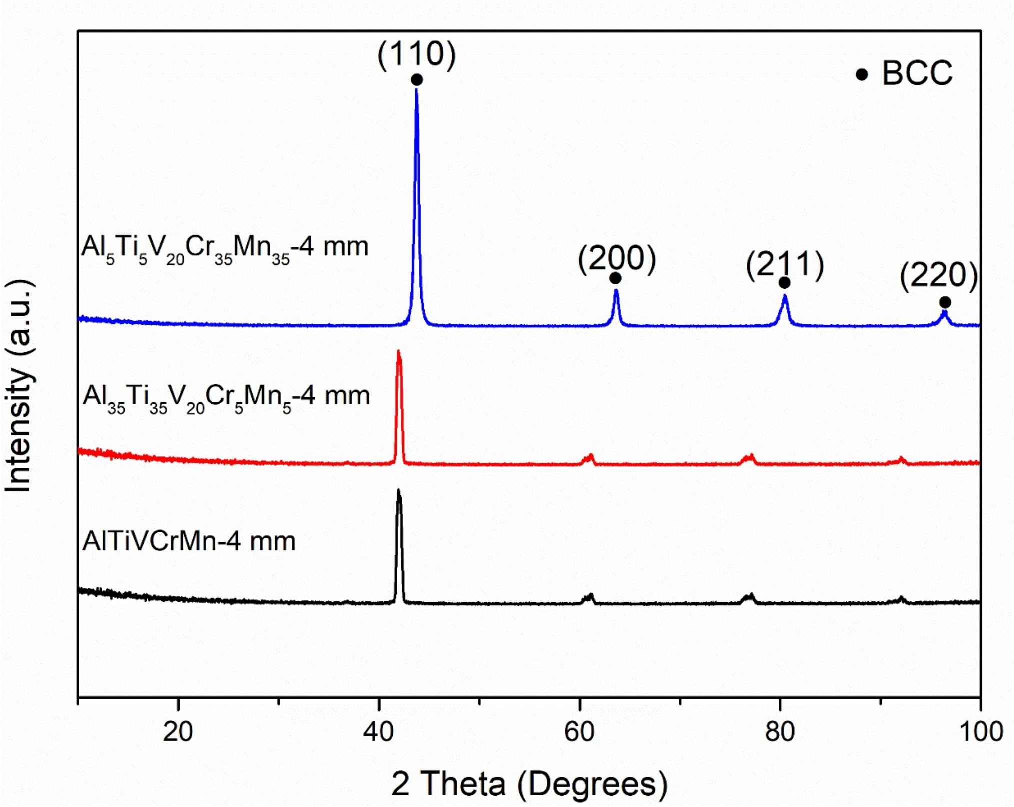

Figure 4.10. XRD patterns of AlTiVCrMn, $Al_{35}Ti_{35}V_{20}Cr_5Mn_5$, and $Al_5Ti_5V_{20}Cr_{35}Mn_{35}$ LWHEAs

Transmission electron microcopy (TEM) investigation is done on 4 mm $Al_{35}Ti_{35}V_{20}Cr_5Mn_5$ LWHEA rod as shown in Figure 4.11. High resolution TEM (HRTEM) images and Fast Fourier Transformation (FFT) image of the LWHEA is seen in Figure 4.11 (a), and Figure 4.11 (b), respectively. Each sets of planes in FFT is labeled as seen in Figure 4.11 (b). This analysis is done to reveal the missing ordered

(100) reflection for B2 phase which is not clear in the XRD patterns of the $Al_{35}Ti_{35}V_{20}Cr_5Mn_5$ LWHEA rod.

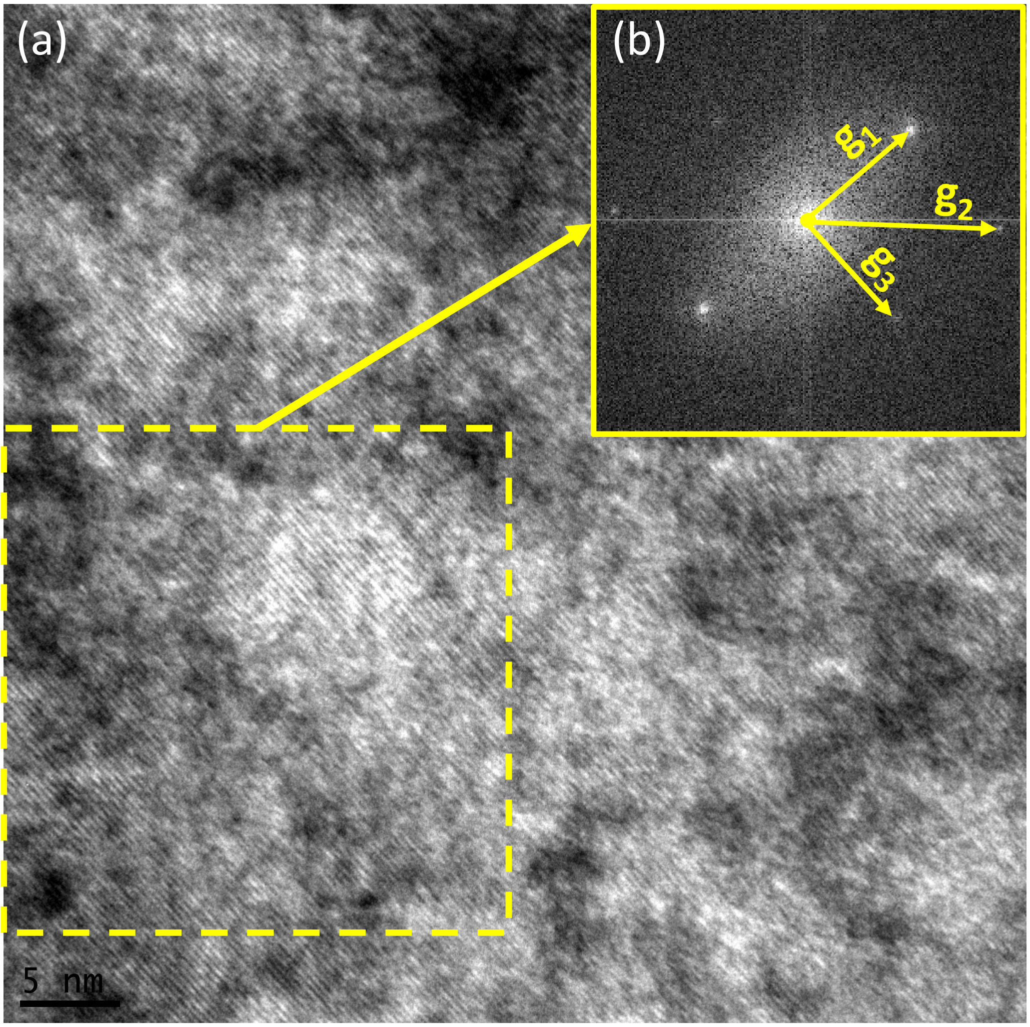

Figure 4.11. TEM images of 4 mm $Al_{35}Ti_{35}V_{20}Cr_5Mn_5$ LWHEA rod a) HRTEM image, b) FFT image of the HRTEM

The measured interplanar spacing (d spacing) distances are in the reciprocal space so their inverses are taken to convert it into real space. Therefore, the inverse FFTs are taken to measure d spacing values for each plane. The planes and corresponding d spacing values in $Al_{35}Ti_{35}V_{20}Cr_5Mn_5$ LWHEA rod are given in Table 4.7. Each individual d spacing values obtained in FFT analysis are matched with the d spacing values obtained from XRD based on the diffraction angles. After correlation between FFT and XRD analysis is done, it is observed that the first sets of the spots in FFT do not match with any d spacing values seen in XRD analysis. It is known that, if the amount of a phase is lower than approximately 1 vol. %, it may not possible to see it in XRD [65]. Therefore, it can be interrupted that 100 reflection in XRD is not seen due to the lower amount of 100 reflection in $Al_{35}Ti_{35}V_{20}Cr_5Mn_5$ LWHEA rod. These show the existence of 100 reflection in TEM analysis, although it is not clear in XRD results.

Table 4.7. Comparison of XRD diffraction angles, d spacing values with the corresponding d values obtained from TEM analysis

hkl	**TEM d spacing values (Å)**	**Corresponding d spacing values in XRD (Å)**	**XRD diffraction angles (2θ)**
100	3.145	-	-
110	2.272	2.146	42.06
200	1.531	1.528	60.54
211	-	1.243	76.56

SEM and OM images of AlTiVCrMn, $Al_{35}Ti_{35}V_{20}Cr_5Mn_5$, and $Al_5Ti_5V_{20}Cr_{35}Mn_{35}$ LWHEAs-cast into 4 mm water-cooled copper mold are shown in Figure 4.12. It is seen in the images that LWHEAs have a dendritic microstructure in the as-cast state. It is known that these types of materials have a brittle structure in as-cast state and ductility of the alloys can be improved by heat treatment processes [66].

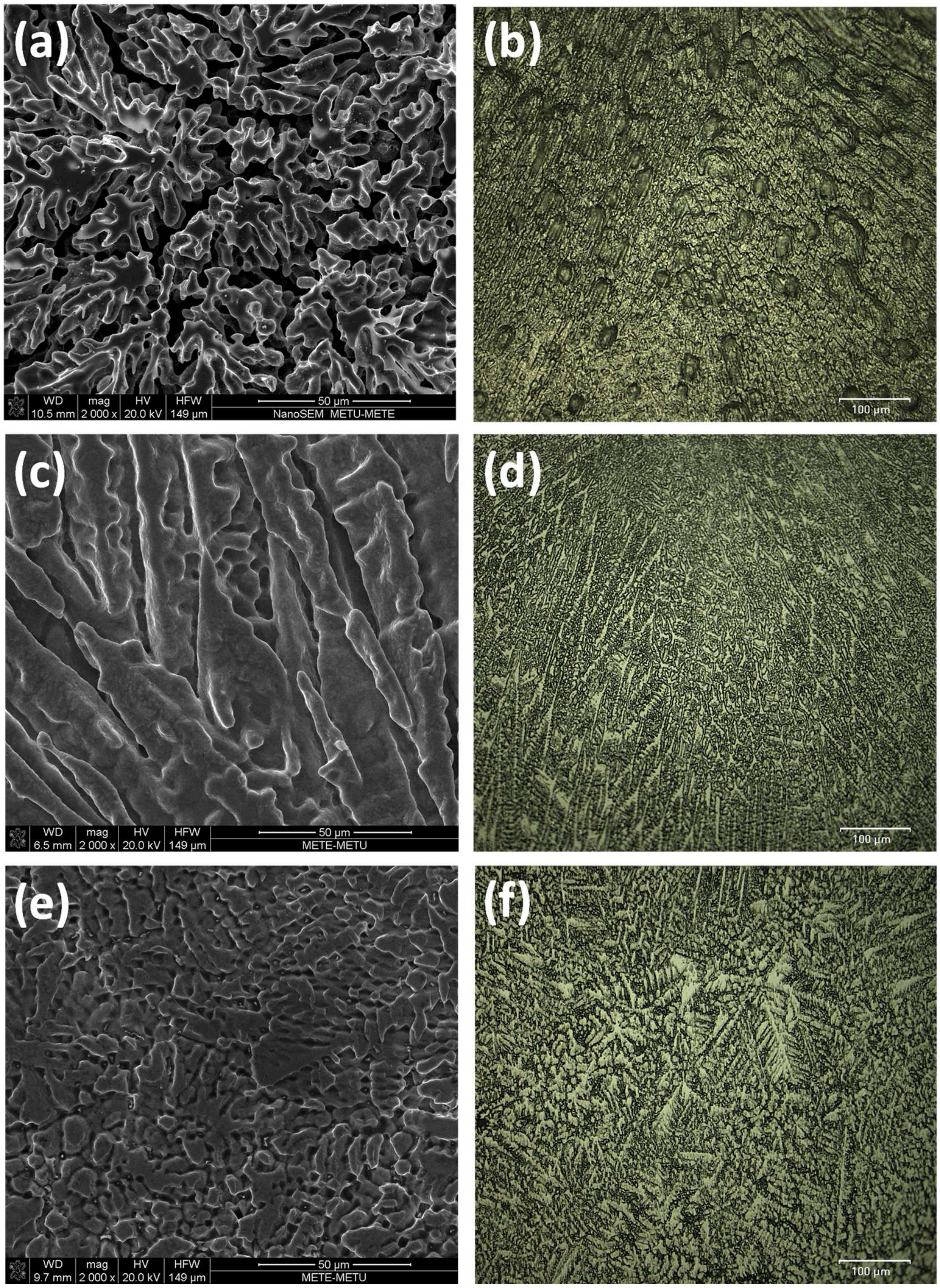

Figure 4.12. a) SEM (2000x), b) OM (500x) images of AlTiVCrMn LWHEA; c) SEM (2000x), d) OM (500x) images of $Al_{35}Ti_{35}V_{20}Cr_5Mn_5$ LWHEA; e) SEM (2000x), f) OM (500x) images of $Al_5Ti_5V_{20}Cr_{35}Mn_{35}$ LWHEA

Hardness values of 4 mm AlTiVCrMn, $Al_{35}Ti_{35}V_{20}Cr_5Mn_5$, and $Al_5Ti_5V_{20}Cr_{35}Mn_{35}$ cylindrical LWHEAs are given in Figure 4.13. The hardness values are taken from side to side of the specimens along the diameters. The average hardness values of AlTiVCrMn, $Al_{35}Ti_{35}V_{20}Cr_5Mn_5$, and $Al_5Ti_5V_{20}Cr_{35}Mn_{35}$ are 583 (±10), 552 (±4), 505 (±17) HV, respectively.

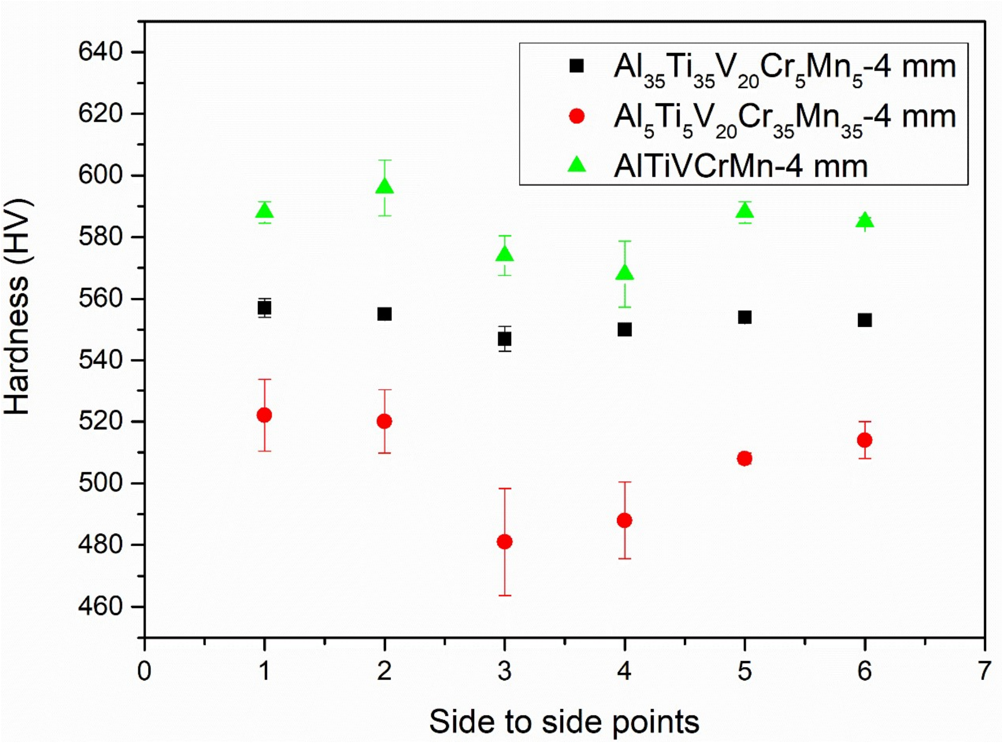

Figure 4.13. Hardness values of 4 mm AlTiVCrMn, $Al_{35}Ti_{35}V_{20}Cr_5Mn_5$, and $Al_5Ti_5V_{20}Cr_{35}Mn_{35}$ cylindrical LWHEAs

AlTiVCrMn LWHEA fractures while it is cast to copper mold as seen in Figure 4.14 (a) that shows a very brittle nature. Compression test is applied to the AlTiVCrMn LWHEA to reveal the fracture behavior. However, the LWHEA fracture even at low compression pressures Figure 4.14 (b). Thus, a compression stress/strain profile could not be obtained for the AlTiVCrMn LWHEA.

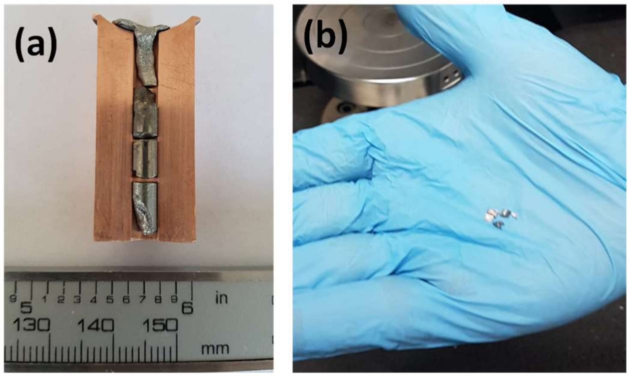

Figure 4.14. Fracture of AlTiVCrMn LWHEA a) after it is cast to 4 mm copper mold, b) while compression test is applied

Compression stress-strain curves of $Al_{35}Ti_{35}V_{20}Cr_5Mn_5$ and $Al_5Ti_5V_{20}Cr_{35}Mn_{35}$ 4 mm cylindrical LWHEAs are given in Figure 4.15. Although $Al_5Ti_5V_{20}Cr_{35}Mn_{35}$ LWHEA fracture at low-stress values, $Al_{35}Ti_{35}V_{20}Cr_5Mn_5$ LWHEA has maximum 387 MPa stress value. Elastic modulus of the $Al_{35}Ti_{35}V_{20}Cr_5Mn_5$ LWHEA is 28 GPa whereas $Al_5Ti_5V_{20}Cr_{35}Mn_{35}$ LWHEA is 26 GPa with its low mechanical values. Thus, $Al_{35}Ti_{35}V_{20}Cr_5Mn_5$ is the most promising LWHEA with its relatively good mechanical properties and low density (4.34 g/cm^3).

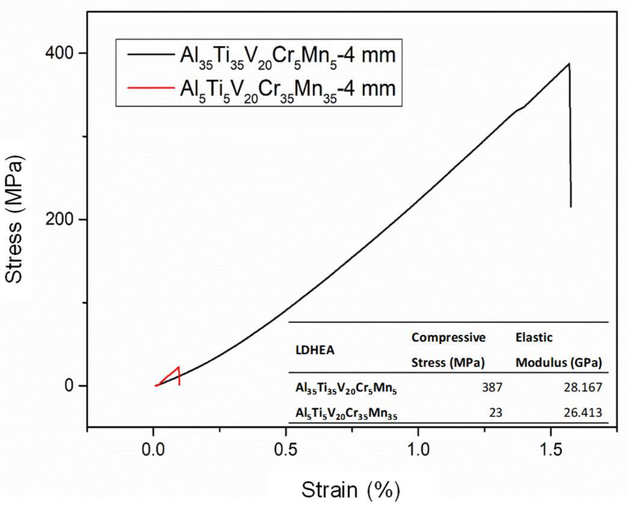

LDHEA	Compressive Stress (MPa)	Elastic Modulus (GPa)
$Al_{35}Ti_{35}V_{20}Cr_5Mn_5$	387	28.167
$Al_5Ti_5V_{20}Cr_{35}Mn_{35}$	23	26.413

Figure 4.15. Compression stress-strain curves of 4 mm $Al_{35}Ti_{35}V_{20}Cr_5Mn_5$ and $Al_5Ti_5V_{20}Cr_{35}Mn_{35}$ LWHEAs

Fracture surfaces of AlTiVCrMn, $Al_{35}Ti_{35}V_{20}Cr_5Mn_5$, and $Al_5Ti_5V_{20}Cr_{35}Mn_{35}$ LWHEAs after compression test are seen in Figure 4.16. A catastrophic failure is observed in the fracture analysis of AlTiVCrMn LWHEA as shown in Figure 4.16 (a). However, transgranular brittle fracture (cleavage) is seen for $Al_{35}Ti_{35}V_{20}Cr_5Mn_5$ (Figure 4.16 (b)) and $Al_5Ti_5V_{20}Cr_{35}Mn_{35}$ (Figure 4.16 (c)) LWHEAs. When the fracture surfaces are investigated in detail, river patterns are seen in $Al_{35}Ti_{35}V_{20}Cr_5Mn_5$ LWHEA that cracking started from a grain boundary whereas $Al_5Ti_5V_{20}Cr_{35}Mn_{35}$ LWHEAs has fine faceted cleavage. These characteristic fracture surfaces are also seen in BCC containing AlCoCrCuFeNi HEAs. Ghassemali et al. [67] observed transgranular crack propagation throughout the BCC grains in dual-phase AlCoCrFeNi HEA. A similar trend is also pointed out by Roy et al. [68]. The transgranular fracture behavior is attributed to the BCC grains in the matrix and at the grain boundary interrupted as an obstacle for the crack propagation [67]. Therefore, the fractography of $Al_{35}Ti_{35}V_{20}Cr_5Mn_5$ and $Al_5Ti_5V_{20}Cr_{35}Mn_{35}$ LWHEAs (Figure 4.16 (b, c)) shows higher strength in the intergrains as compared to the grains that causing a transgranular fracture.

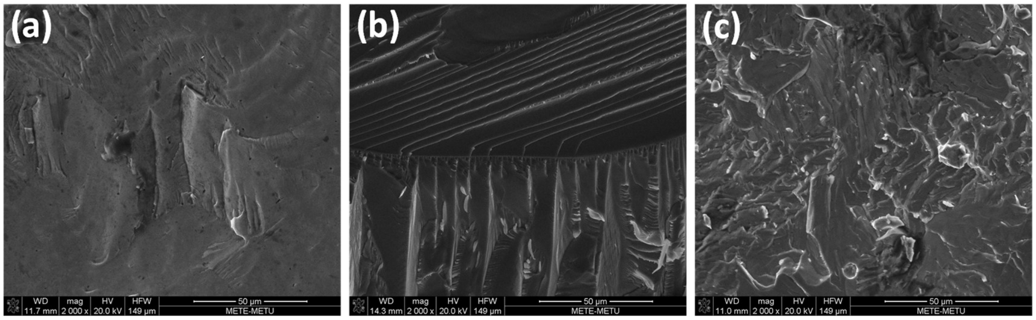

Figure 4.16. Fracture surfaces of a) AlTiVCrMn, b) $Al_{35}Ti_{35}V_{20}Cr_5Mn_5$ and c) $Al_5Ti_5V_{20}Cr_{35}Mn_{35}$ LWHEAs after compression test

Differential thermal analysis (DTA) analysis was performed on 4 mm AlTiVCrMn, $Al_{35}Ti_{35}V_{20}Cr_5Mn_5$ and $Al_5Ti_5V_{20}Cr_{35}Mn_{35}$ LWHEAs to reveal the possible phase transformations and measure melting points of the LWHEAs. The specimens are heated up to 1300 °C in a nitrogen gas environment with a 10 °C/min heating rate.

DTA curves of the LWHEAs are shown in Figure 4.17. DTA curves of the LWHEAs are similar to each other without any peaks. These curves indicate that there is not any phase transformation or melting up to 1300 °C in the LWHEAs.

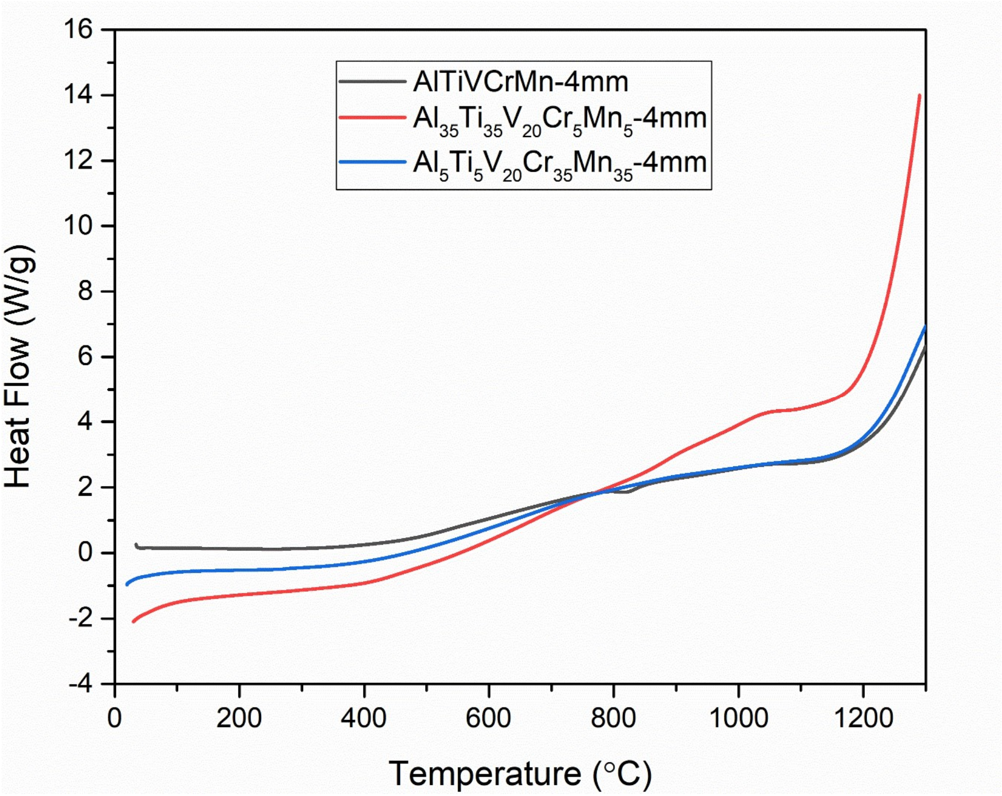

Figure 4.17. DTA curves of 4 mm AlTiVCrMn, $Al_{35}Ti_{35}V_{20}Cr_5Mn_5$ and $Al_5Ti_5V_{20}Cr_{35}Mn_{35}$ LWHEAs

Heat treatment processes are applied to increase the mechanical properties of the most promising LWHEA which is 4 mm cylindrical $Al_{35}Ti_{35}V_{20}Cr_5Mn_5$ LWHEA. The LWHEA is heat-treated at 1000 °C for 12 h. and 24 h. duration under a vacuum environment (10^{-2} mbar) in a tube furnace. XRD patterns of heat-treated samples are shown in Figure 4.18. It is seen in the figure that secondary phases (ICs) take place at elevated temperatures. The relative intensities of ICs for 24 h. are higher than 12 h. at 1000 °C. Thus, the amount of the secondary phases increases with increasing annealing time at 1000 °C. However, the intensities of BCC phases for both annealing times are dramatically higher than ICs.

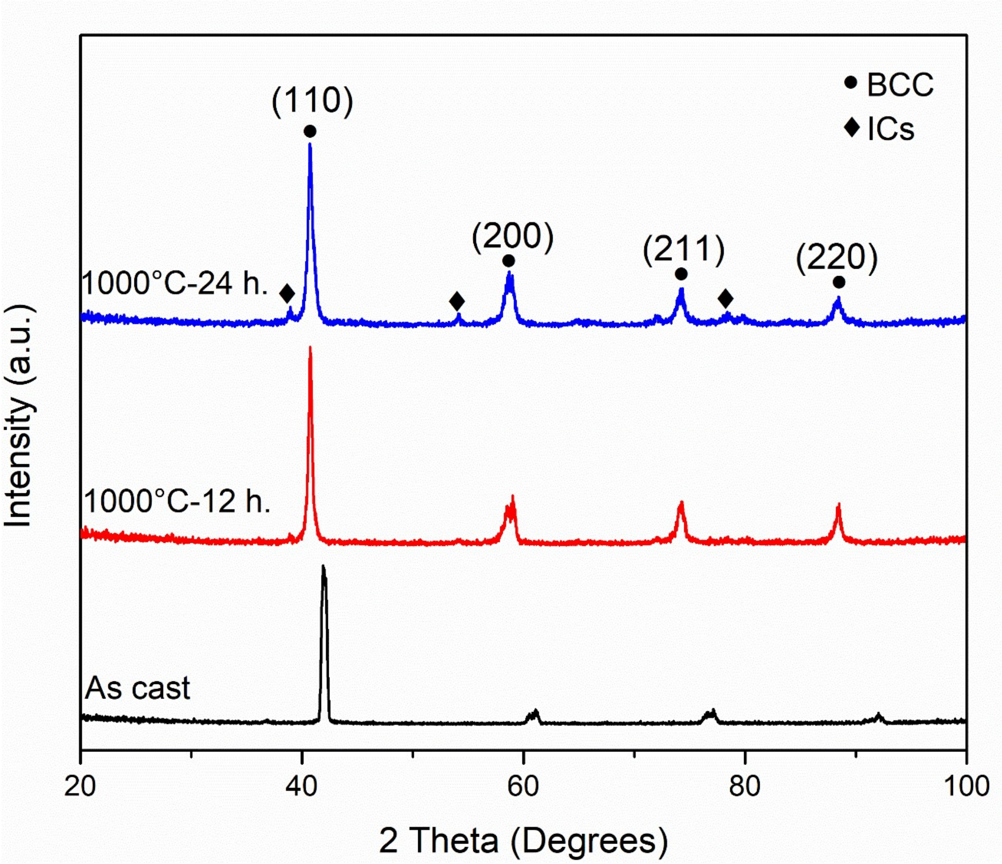

Figure 4.18. XRD patterns of heat-treated $Al_{35}Ti_{35}V_{20}Cr_5Mn_5$ LWHEA

The diffraction angles of BCC 4 mm $Al_{35}Ti_{35}V_{20}Cr_5Mn_5$ LWHEA phases shift to the left-hand side after the annealing at 1000 °C as seen in Figure 4.18. This means that an extension in crystal structure occurs after annealing. This situation may take place due to the rejection of the atoms with relatively small atomic radii such as Al and Mn. The rejected atoms form secondary phases (ICs) besides BCC phases. Thus, it is predicted that the most probable ICs are the compounds of Al and Mn elements.

Based on the prediction done by thermophysical calculations, as shown in Table 4.5, the expected (equilibrium) phases are observed for the 4 mm $Al_{35}Ti_{35}V_{20}Cr_5Mn_5$

LWHEA heat-treated at 1000 °C for 24 h. Thus, these samples are chosen to compare their as-cast and heat-treated conditions and further investigations are done on them.

SEM and OM investigation of 4 mm $Al_{35}Ti_{35}V_{20}Cr_5Mn_5$ LWHEA for as-cast and heat-treated at 1000 °C for 24 h. conditions are performed. The corresponding images are shown in Figure 4.19. As-cast 4 mm $Al_{35}Ti_{35}V_{20}Cr_5Mn_5$ LWHEA has dendritic microstructure substantially (Figure 4.19 (a) and (b)). This dendritic morphology is removed by the annealing process as seen in Figure 4.19 (c, d). After the heat treatment, fine canals are observed in the microstructure along with large grains. The amount of the fine canals is very low as compared to the matrix phase and it is known from the XRD patterns that (Figure 4.18) 4 mm $Al_{35}Ti_{35}V_{20}Cr_5Mn_5$ LWHEA has minor ICs and major BCC phase. Therefore, it can possible to match these canals with the ICs in the XRD patterns whereas large grains (matrix) corresponds to the BCC phase.

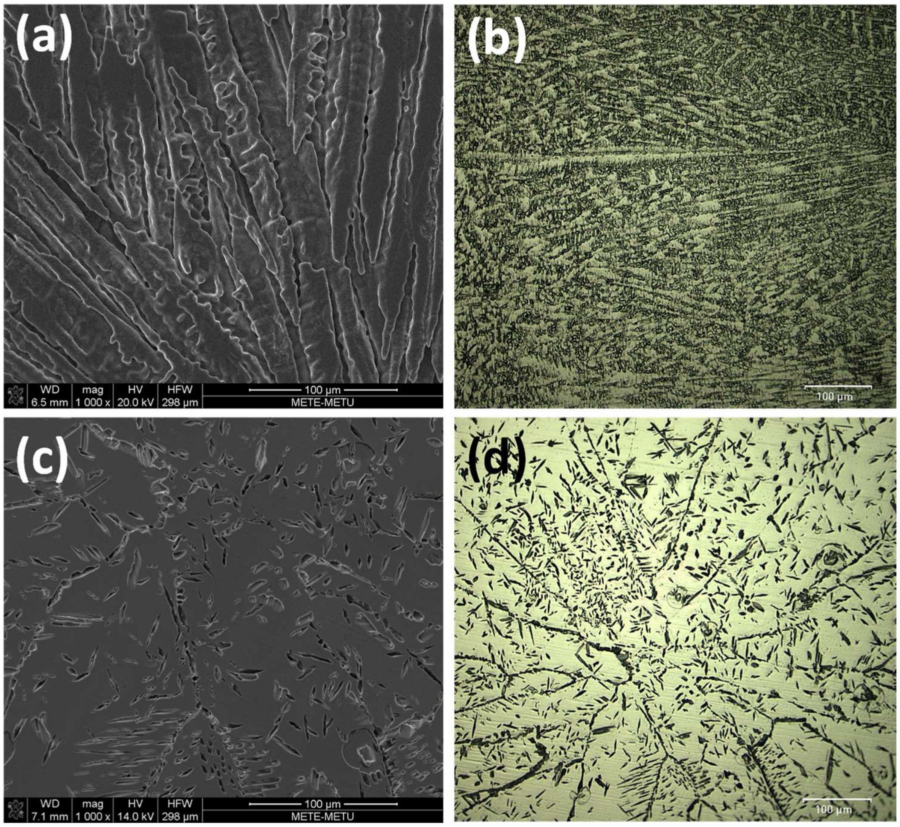

Figure 4.19. As-cast a) SEM (1000x), b) OM (500x); Heat treated at 1000 °C for 24 h. c) SEM (1000x), d) OM (500x) images of 4 mm cylindrical $Al_{35}Ti_{35}V_{20}Cr_5Mn_5$ LWHEA

Hardness profiles of as-cast and heat-treated (1000 °C for 24 h.) of 4 mm $Al_{35}Ti_{35}V_{20}Cr_5Mn_5$ LWHEA are given in Figure 4.20. The hardness values are taken from corner to corner of the cylindrical samples. The average hardnesses of as-cast and heat-treated 4 mm $Al_{35}Ti_{35}V_{20}Cr_5Mn_5$ LWHEA are 505 (±4) and 552 (±17) HV, respectively. It is seen that the average hardness of the heat-treated sample is lower than the as-cast samples. The morphological distribution of the dendritic structure is more dominant to increase the hardness of the samples over the ICs.

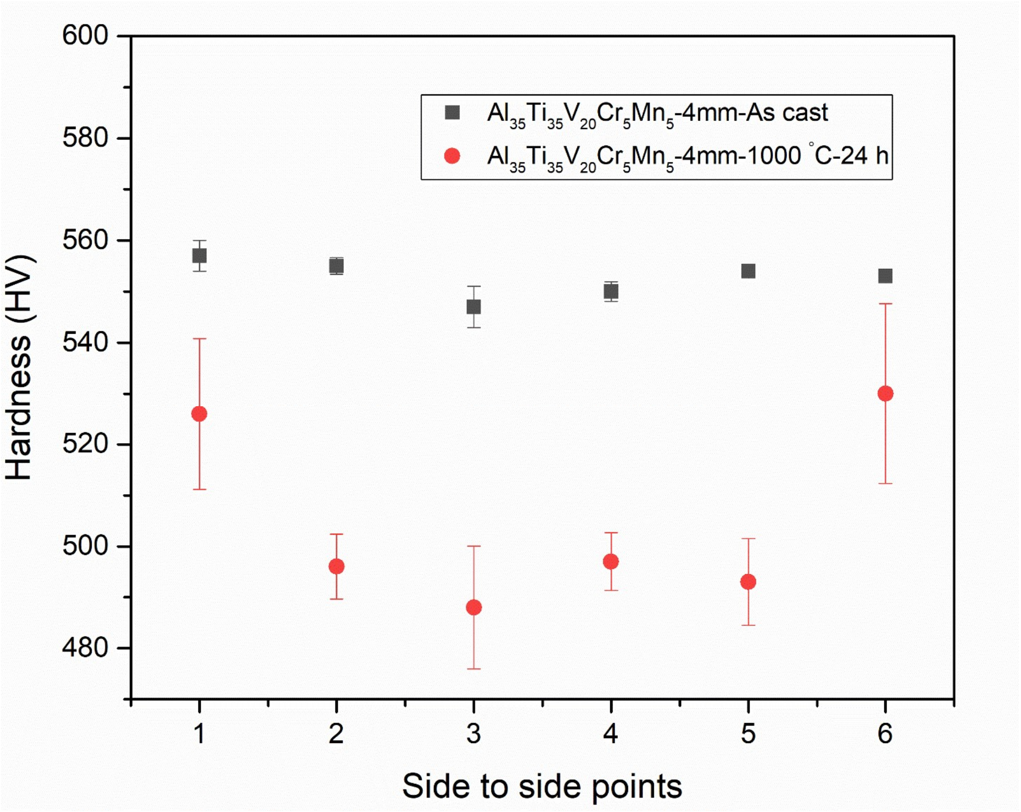

Figure 4.20. Hardness values of as-cast and heat-treated 4 mm cylindrical $Al_{35}Ti_{35}V_{20}Cr_5Mn_5$ LWHEA

Compression stress-strain curves of as-cast and heat-treated (1000 °C for 24 h) 4 mm cylindrical $Al_{35}Ti_{35}V_{20}Cr_5Mn_5$ LWHEA is seen in Figure 4.21. As-cast and heat-treated samples have 386 and 357 MPa fracture strength; 29 and 26 GPa elastic modulus, respectively. The samples have the same (approximately 1.6%) fracture strain. However, decrease in hardness (Figure 4.20), fracture strength and elastic modulus indicate that 4 mm $Al_{35}Ti_{35}V_{20}Cr_5Mn_5$ LWHEA can be softened by heat treatment processes. Therefore, the ductility of the $Al_{35}Ti_{35}V_{20}Cr_5Mn_5$ LWHEA can be improved by optimizing heat treatment processes.

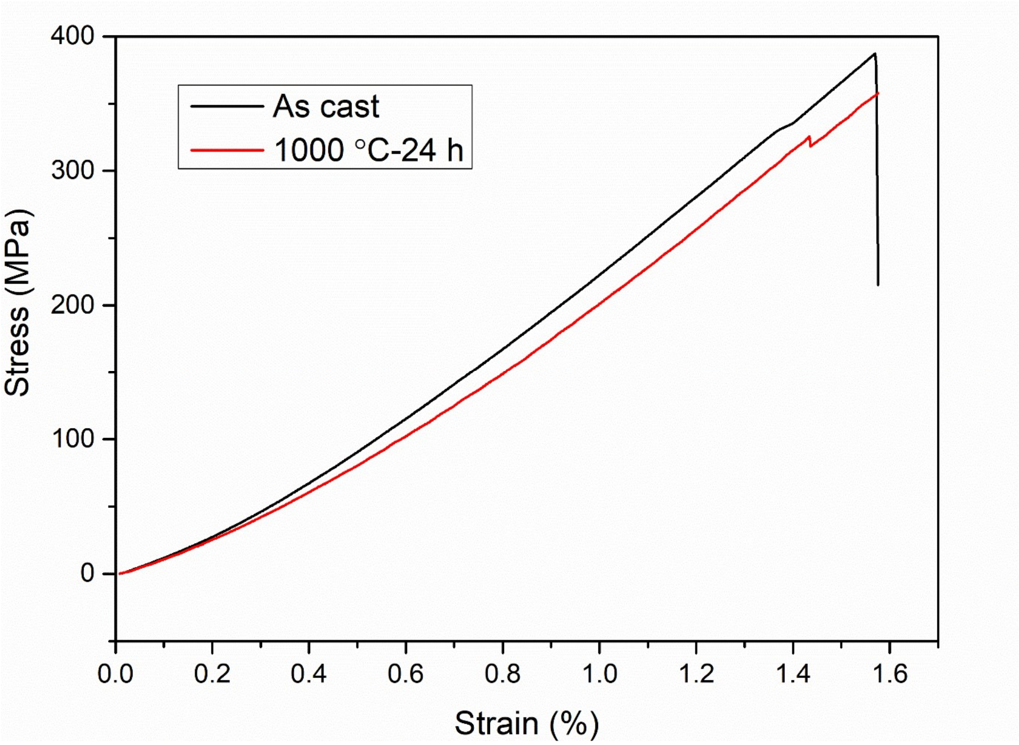

Figure 4.21. Compression stress-strain curves of as-cast and heat-treated 4 mm cylindrical $Al_{35}Ti_{35}V_{20}Cr_5Mn_5$ LWHEA

SEM secondary electron (SE) analysis of $Al_{35}Ti_{35}V_{20}Cr_5Mn_5$ LWHEA after the compression test is given in Figure 4.22. Characteristics of transgranular brittle fractures are seen in the images and river patterns present along the grains.

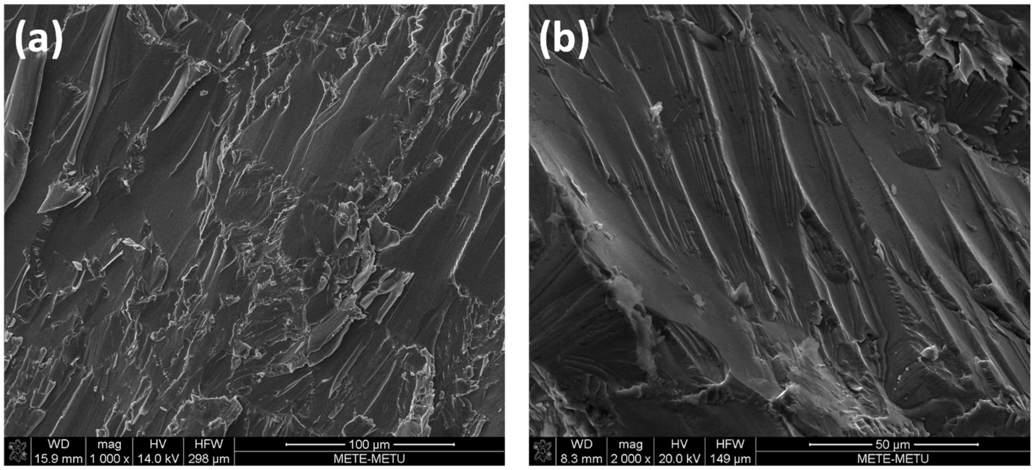

Figure 4.22. Fracture surface of 4 mm cylindrical $Al_{35}Ti_{35}V_{20}Cr_5Mn_5$ LWHEA after compression test

4.4. Conclusion

In this part of the study, $AlTiVCrMnB_x$ (x=0, 0.3, 0.6, 1.0), AlTiVCrSi, AlTiVCrMnSi, AlTiVCrMn, $Al_{35}Ti_{35}V_{20}Cr_5Mn_5$, $Al_5Ti_5V_{20}Cr_{35}Mn_{35}$ LWHEAs are designed by thermophysical calculations and Vienna Ab initio Simulation Package (VASP). The primary alloy design criterion is to produce LWHEAs that low-density elements such as B, Al, Si, and Ti are widely used. The LWHEAs are produced by arc-melter and their structural, mechanical properties are investigated. These LWHEAs are cast to 3 and 4 mm water-cooled cylindrical copper molds to investigate their structural and mechanical properties. Lower density value is obtained in $Al_{35}Ti_{35}V_{20}Cr_5Mn_5$ LWHEAs with a density of 4.34 g/cm^3 and heat treatment processes are applied to the $Al_{35}Ti_{35}V_{20}Cr_5Mn_5$ LWHEA to reveal the effect of heat treatment on structural and mechanical properties of the LWHEA. Although a sufficiently enough density is achieved in the LWHEAs, the results show that ordered BCC (B2) phase present in the LWHEAs that make them very brittle even at low forces.

CHAPTER 5

DESIGN AND PRODUCTION OF DUAL PHASE MEAs CONSIST OF Cu-Ni-Al-Ti ELEMENTS

5.1. Introduction

In some cases, single or dual solid solution phases can be achieved in multicomponent systems when the number of elements is less than 5. Yeh et al. [12] pointed out that a relatively higher configurational entropy (S_{conf}) between 1R (8.314 kJ/mol.K) and 1.5R (12.471 kJ/mol.K) can be achieved when the number of elements are less than 5. These systems are called medium entropy alloys (MEAs). The HEA and MEA systems generally form in single or dual FCC, BCC and HCP phases rather than multicomponent phases [9]–[12], [69] when the phases have higher S_{conf} values as compared to IC counterparts [7], [70].

It has been demonstrated that these new types of alloys have superior mechanical [71], magnetic [72], and thermal properties [73] as compared to their traditional equivalent. In terms of mechanical strength, single phase FCC HEAs are ductile but not sufficiently strong, on the other hand, single phase BCC HEAs are strong enough with low ductility. In that sense, novel HEAs with dual solid solution phases are adopted to further improve the mechanical properties [74]–[76]. In many cases, it is shown that the strength of the HEAs can be enhanced with BCC and FCC dual phases over single phase. For example, Gangireddy et al. [77] show that the yield strength of the $Al_xCoCrFeNi$ with single FCC phase has dramatically increased from 160 MPa to 830 MPa by inducing BCC phase. Li et al. [78] have developed a novel dual-phase high-entropy alloy (TRIPDP-HEA) by combining FCC and HCP phases to optimize the yield strength (350 MPa) and ductility (72 %) of the alloy. Also, Guo et al. [79] have investigated the structure and hardness properties of dual phase Co free $Al_xCrCuFeNi_2$

HEA. They report that the hardness of the BCC phase can be softened from 600 HV to 325 HV with its BCC and FCC dual phases. Moreover, the mechanical behavior of dual phase HEAs are also investigated at cryogenic [80] and high [81] temperatures. It is shown that the dual-phase AlCoCrFeNi HEA offers significant potential for high-temperature applications with its 1075 MPa yield strength and 29.3 % plastic strain at 873 K [81].

These studies all suggest that the dual solid solution phases rather than a single solid solution act better to achieve better mechanical properties. For the prediction of the HEA crystal structure, the VEC has been widely used. The predicted phases in the HEAs can be composed of a single to dual solid solution by adjusting the VEC values of the alloys [82]. The elements with low VEC values promote the formation of BCC phases, whereas high VEC values promote FCC phases. The medium-entropy-alloys have reduced configurational entropies at random states as compared to HEAs. On the other hand, they may even possess better mechanical properties with their quite simple crystal structure as compared to HEAs without any restriction of equiatomic or near-equiatomic compositions [83]. For instance, CrFeCoNi MEA has similar tensile behavior under various test temperatures compared to CrMnFeCoNi HEA [84]. while the reported CrCoNi MEA shows better yield and fracture strength over CrMnFeCoNi HEA [85]. Although similar thermodynamical criteria have been proposed, the effects of tuning VEC values to create single or dual phases have not been studied thoroughly in MEAs.

In this part, a series of $Cu_{20}Ni_{20}Al_{30}Ti_{30}$, $Cu_{25}Ni_{25}Al_{25}Ti_{25}$, $Cu_{34}Ni_{22}Al_{22}Ti_{22}$ and $Cu_{35}Ni_{25}Al_{20}Ti_{20}$ MEAs have been investigated. These alloys are designed and produced based on the VEC values to produce single BCC and BCC/FCC composite MEA structures. Cu and Ni elements are used due to their higher VEC values to form FCC phases, whereas Al and Ti are selected because of their low VEC values to promote BCC phases. These MEAs are then produced using suction casting and its structural and mechanical properties are investigated in details.

5.2. Design and Simulation of the MEAs

The alloys produced in this study consist of Cu, Ni, Al and Ti elements with VEC values of 11, 10, 3 and 4, respectively. If the VEC value of the alloys is less than 6.87 BCC, if it is higher than 8 FCC phase is predicted. On the other hand, if the VEC is between 6.87 and 8 BCC/FCC dual phase structure is expected. In that sense, among these elements, Cu and Ni promote FCC type of structure, Al and Ti promote BCC type of structure, based on their VEC values. VEC value of equiatomic $Cu_{25}Ni_{25}Al_{25}Ti_{25}$ MEA is found to be 7.00. This value is just above the critical lower limit of BCC and FCC composite structure region. While it is far from complete and reliable, VEC criterion is helpful in some aspects of alloy design. It requires comprehensive experimental evaluations to verify the concept [86]. Therefore, our experimental results are also compared with the VEC based structure prediction to reveal its reliability.

The other critical parameters for MEAs are; i. atomic size difference (δ) which is expected to be less than 6.6 and ii. enthalpy of mixing (ΔH_{mix}). In most of the previous studies, ΔH_{mix} was reported being between - 22 kJ/mol and 7 kJ/mol for single solid solutions [14], [15]. Critical thermophysical parameters calculated for Cu-Ni-Al-Ti MEA are shown in Table 5.1.

Table 5.1. Thermophysical parameters MEAs

MEAs	Density (g/cm^3)	δ (%)	ΔH_{mix} (kJ/mol)	VEC	ΔS_{mix} (kJ/mol.K)	T_m (°C)	VEC Predicted Phase(s)
$Cu_{20}Ni_{20}Al_{30}Ti_{30}$	6.49	6.93	-26.24	6.30	11.36	1207	BCC
$Cu_{25}Ni_{25}Al_{25}Ti_{25}$	7.00	7.16	-23.25	7.00	11.53	1207	BCC+FCC
$Cu_{34}Ni_{22}Al_{22}Ti_{22}$	7.29	7.00	-18.64	7.48	11.36	1201	BCC+FCC
$Cu_{35}Ni_{25}Al_{20}Ti_{20}$	7.46	6.99	-17.60	7.75	11.29	1209	BCC+FCC

As shown in Table 5.1, VEC values of the $Cu_{25}Ni_{25}Al_{25}Ti_{25}$, $Cu_{34}Ni_{22}Al_{22}Ti_{22}$, and $Cu_{35}Ni_{25}Al_{20}Ti_{20}$ MEAs are 7.00, 7.48 and 7.75, respectively. Increasing the amounts of Cu and Ni in the MEAs promotes the formation of FCC structure. In that sense, atomic amounts of Cu, Ni, Al and Ti atoms can be arranged to have a series of MEAs with various amounts of BCC and FCC phases. For this purpose, $Cu_{20}Ni_{20}Al_{30}Ti_{30}$, MEA is produced to represent BCC structure; $Cu_{25}Ni_{25}Al_{25}Ti_{25}$, $Cu_{34}Ni_{22}Al_{22}Ti_{22}$, and $Cu_{35}Ni_{25}Al_{20}Ti_{20}$ are produced to represent dual BCC and FCC composite structure.

Thermo-Calc software is used to simulate the solidification path for $Cu_{20}Ni_{20}Al_{30}Ti_{30}$, $Cu_{25}Ni_{25}Al_{25}Ti_{25}$, $Cu_{34}Ni_{22}Al_{22}Ti_{22}$, and $Cu_{35}Ni_{25}Al_{20}Ti_{20}$ MEAs. The corresponding solidification products were simulated using equilibrium stepping calculation to predict the relative amounts of primary and secondary phases that solidify from the liquid.

Mole fractions of the solid phases with respect to temperature are shown in Figure 5.1. The equilibrium stepping calculation for $Cu_{20}Ni_{20}Al_{30}Ti_{30}$ shows ordered BCC (B2) and intermetallic Laves phases (C14 Laves) at lower temperatures as seen in Figure 5.1 (a). The ICs predicted in the simulation should be correlated to the relatively low ΔH_{mix} which is calculated to be -26.24 kJ/mol $Cu_{20}Ni_{20}Al_{30}Ti_{30}$. These values are calculated based on the binary ΔH_{mix} values given in Table 5.2 [87]. The predicted range for a single solid solution is given as -22 kJ/mol$<\Delta H_{mix}<7$ kJ/mol [14], [15]. Therefore, $Cu_{20}Ni_{20}Al_{30}Ti_{30}$ MEA is expected to contain ICs in their as-cast conditions. On the other hand, the simulation of $Cu_{25}Ni_{25}Al_{25}Ti_{25}$ MEA (Figure 5.1 (a)) has a single BCC phase at lower temperatures without ICs due to relatively increasing ΔH_{mix} value.

Table 5.2. Chemical enthalpy of mixing ΔH_{mix} (kJ/mol) of the atom pairs [87]

	Cu	**Ni**	**Al**	**Ti**
Cu	0	4	-1	-9
Ni		0	-22	-35
Al			0	-30
Ti				0

The equilibrium stepping calculation of $Cu_{34}Ni_{22}Al_{22}Ti_{22}$ and $Cu_{35}Ni_{25}Al_{20}Ti_{20}$ MEAs are given in Figure 5.1 (c, d), respectively. In both cases, FCC and BCC composite phase mixtures are present after solidification. The amount of FCC phase is higher in $Cu_{35}Ni_{25}Al_{20}Ti_{20}$ MEA (Figure 5.1 (d)) as compared to $Cu_{34}Ni_{22}Al_{22}Ti_{22}$ MEA (Figure 5.1 (c)). This is in good agreement with the statement of having more FCC concerning the increase in VEC due to higher Cu and Ni amounts. Equilibrium stepping calculations do not predict any formation of ICs for $Cu_{34}Ni_{22}Al_{22}Ti_{22}$ and $Cu_{35}Ni_{25}Al_{20}Ti_{20}$. The calculated ΔH_{mix} values for $Cu_{34}Ni_{22}Al_{22}Ti_{22}$ and $Cu_{35}Ni_{25}Al_{20}Ti_{20}$ (Table 5.1) are well above the expected range for IC formation.

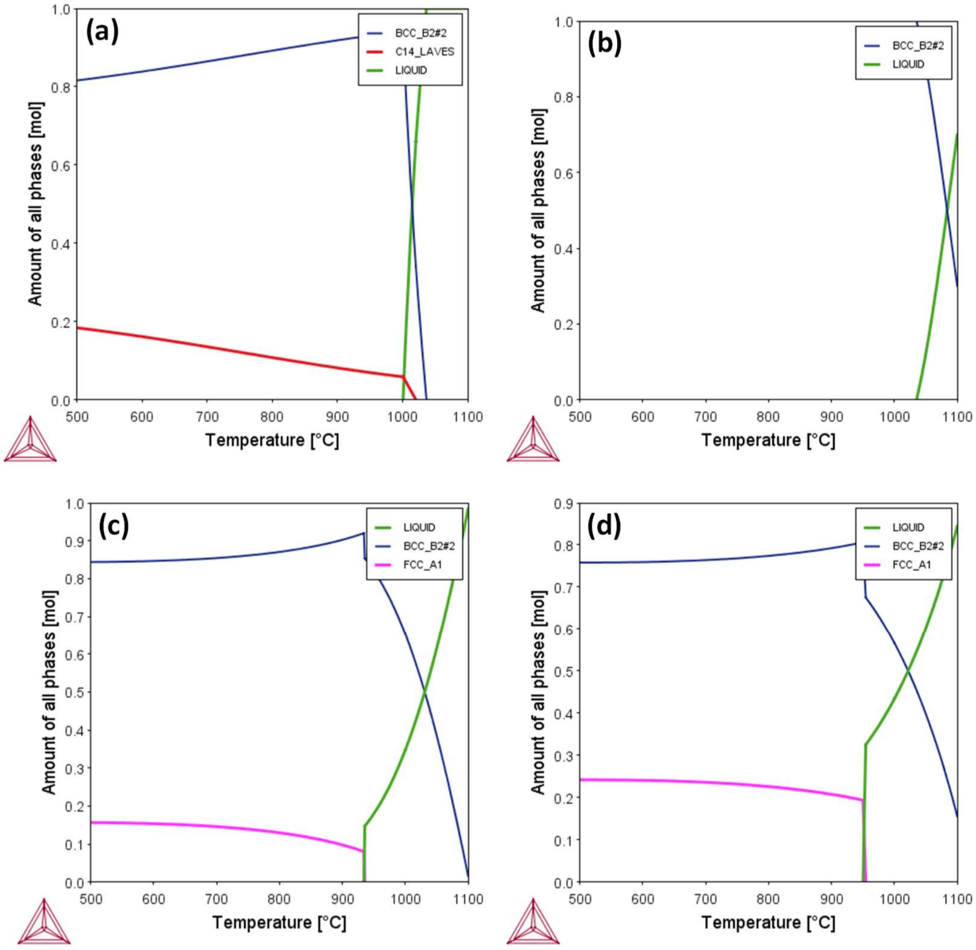

Figure 5.1. Equilibrium stepping calculation of a) $Cu_{20}Ni_{20}Al_{30}Ti_{30}$, b) $Cu_{25}Ni_{25}Al_{25}Ti_{25}$, c) $Cu_{34}Ni_{22}Al_{22}Ti_{22}$, d) $Cu_{35}Ni_{25}Al_{20}Ti_{20}$ MEAs

5.3. Experimental Analyses of the MEAs

5.3.1. Structural Characterization at Room Temperature

XRD patterns of $Cu_{20}Ni_{20}Al_{30}Ti_{30}$, $Cu_{25}Ni_{25}Al_{25}Ti_{25}$, $Cu_{34}Ni_{22}Al_{22}Ti_{22}$, and $Cu_{35}Ni_{25}Al_{20}Ti_{20}$ MEAs are shown in Figure 5.2. The $Cu_{20}Ni_{20}Al_{30}Ti_{30}$ MEA consists of BCC and AlNiTi IC phases. This result verifies the equilibrium stepping calculation of the MEA (Figure 5.1 (a)) for this specific composition. The low mixing enthalpy of $Cu_{20}Ni_{20}Al_{30}Ti_{30}$ MEA (-26.24 kJ/mol) promotes the formation of ICs. The increase in Cu and Ni content results in the formation of single BCC and later dual BCC and FCC structures. These results are again in good agreement with equilibrium stepping calculation simulations. The increasing amount of Cu and Ni elements in the $Cu_{34}Ni_{22}Al_{22}Ti_{22}$ and $Cu_{35}Ni_{25}Al_{20}Ti_{20}$ MEAs increase the VEC value as indicated in Table 5.1. Higher VEC values (>6.87) stabilizes FCC phases with BCC phases [17]. Therefore, these MEAs have BCC and FCC phase mixtures as shown in Figure 5.2.

The calculated lattice parameter of the BCC phase in Cu-Ni-Al-Ti MEAs decreases from 2.973 Å to 2.942 Å when the amounts of Cu and Ni elements in the MEAs are increased. The lattice parameter of the FCC phase follows a similar trend changing its values from 3.651 to 3.630 Å. This is due to the lattice parameter regression in MEA solid solutions as a result of the cocktail effect observed in MEAs [13], [18].

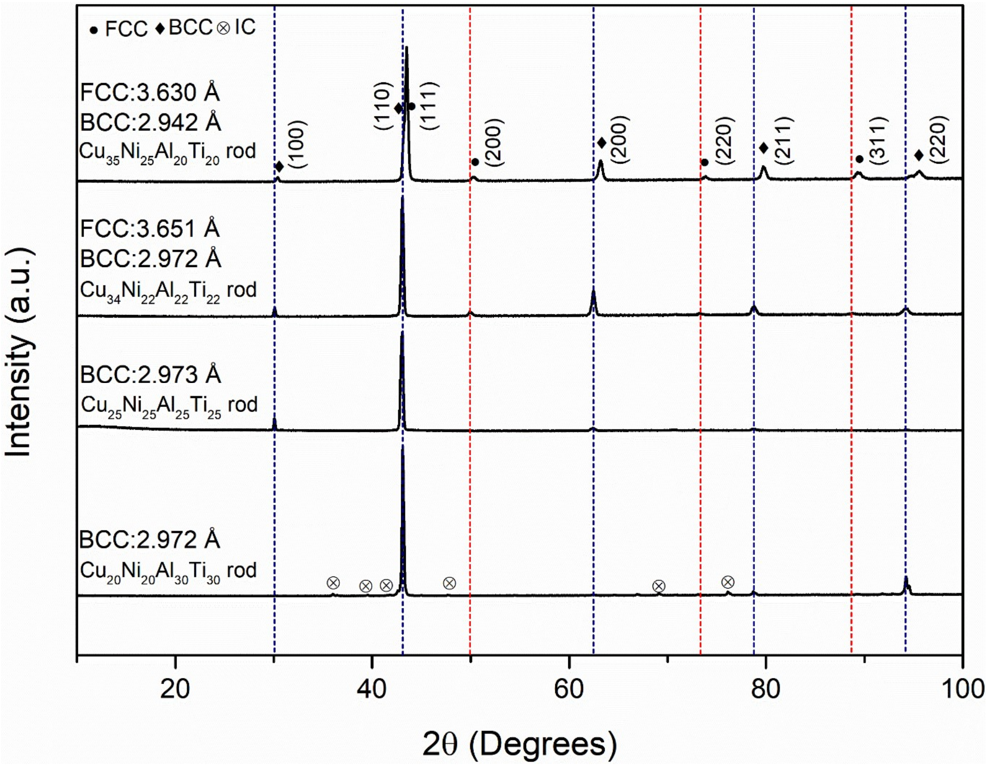

Figure 5.2. XRD patterns of $Cu_{20}Ni_{20}Al_{30}Ti_{30}$, $Cu_{25}Ni_{25}Al_{25}Ti_{25}$, $Cu_{34}Ni_{22}Al_{22}Ti_{22}$ and $Cu_{35}Ni_{25}Al_{20}Ti_{20}$ MEAs

5.3.2. Mechanical Properties

The average hardness value of 3 mm as-cast $Cu_{20}Ni_{20}Al_{30}Ti_{30}$ MEA rod is 734 HV (±9). This alloy consists of BCC and AlNiTi IC according to XRD analyses. The presence of these two phases makes the alloy hard and brittle. Similar behavior is also observed in $Cu_{25}Ni_{25}Al_{25}Ti_{25}$ with a hardness value of 693 (±12).

The average hardness values of these MEAs are decreased with increasing Cu and Ni content. The hardness for $Cu_{34}Ni_{22}Al_{22}Ti_{22}$ and $Cu_{35}Ni_{25}Al_{20}Ti_{20}$ are measured as 537 HV (±13) and 427 HV (±6), respectively. The decrease in hardness values should be related to the formation of a relatively soft FCC phase.

$Cu_{20}Ni_{20}Al_{30}Ti_{30}$ and $Cu_{25}Ni_{25}Al_{25}Ti_{25}$ MEAs fracture easily without any ductility even at low pressures. Consequently, it is not possible to perform a compression test out of these specimens. The corresponding fracture surface of $Cu_{20}Ni_{20}Al_{30}Ti_{30}$ and $Cu_{25}Ni_{25}Al_{25}Ti_{25}$ MEAs are shown in Figure 5.4 (a), (b), and (c), (d), respectively.

The results of compression tests are shown in Figure 5.3. It is seen in the figure that the stress value of $Cu_{34}Ni_{22}Al_{22}Ti_{22}$ MEA is close to 184 MPa with 1.3 % strain. The lower strain values originate from the BCC crystal structure of the MEA. It is not possible to define an elastic limit for this alloy due to its very brittle structure. However, it is seen Figure 5.3 that $Cu_{35}Ni_{25}Al_{20}Ti_{20}$ suction-cast MEA rods have sufficient strain to define the elastic limit. The strain value of $Cu_{35}Ni_{25}Al_{20}Ti_{20}$ MEA rods is 13 %. The yield and fraction stresses of the alloy under compression are determined as 820 and 1338 MPa, respectively.

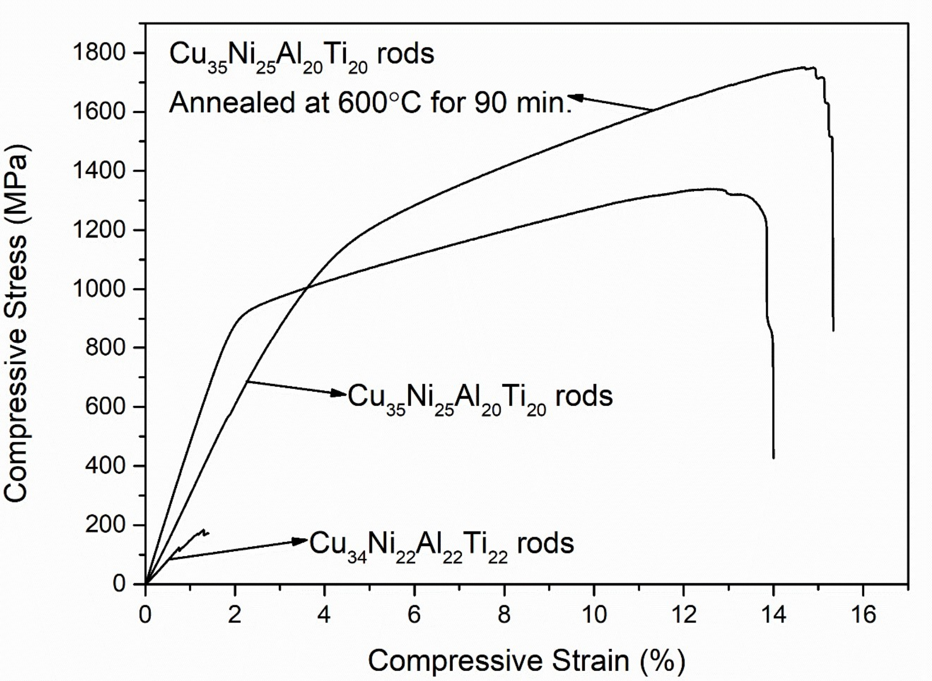

Figure 5.3. Compression test results of 3 mm $Cu_{34}Ni_{22}Al_{22}Ti_{22}$ and $Cu_{35}Ni_{25}Al_{20}Ti_{20}$ MEA rods

The fracture surfaces of the $Cu_{20}Ni_{20}Al_{30}Ti_{30}$, $Cu_{34}Ni_{22}Al_{22}Ti_{22}$, and $Cu_{35}Ni_{25}Al_{20}Ti_{20}$ MEAs after compression test are shown in Figure 5.4. $Cu_{20}Ni_{20}Al_{30}Ti_{30}$ MEA has a brittle nature due to the distorted BCC phases with low slip systems and ICs in the alloy. The samples fracture easily even at low forces in the compression tests with the river lines by cleavage mode. From the fracture surface of the MEA (Figure 5.4 (a, b)) it is seen that the faceted regions are surrounded by the river lines. A similar fracture nature can be often seen in amorphous materials [88].

FCC phases beside BCCs are induced into the $Cu_{34}Ni_{22}Al_{22}Ti_{22}$ MEA by decreasing the atomic amounts of Al and Ti atoms as seen in Figure 5.1 and Figure 5.2. The fracture surface of this MEA is shown in (Figure 5.4 (c, d)). A cleavage mode dominated fracture is seen in the sample with lenticular dimples and tear edges. This type of fracture surface is seen in previous studies [89].

The fracture surface $Cu_{35}Ni_{25}Al_{20}Ti_{20}$ MEAs is shown in Figure 5.4 (e, f). The sample has mainly two regions: cleavages and dimples. The cleavage regions are colored with gray color, whereas dimples are whitish. Zoom-in view of the fracture surface (Figure 5.4 (f)) shows that the sample has dimples and tear edges with the characteristic appearance of ductile MEAs [88]. These regions with dimples correspond to the FCC phases in the samples due to their higher slip system compared to BCC phases. In other words, FCC phases have more ductility than BCC ones [31, 32]. Therefore, it is possible to match the ductile regions with the FCC phases present in the $Cu_{35}Ni_{25}Al_{20}Ti_{20}$ MEA.

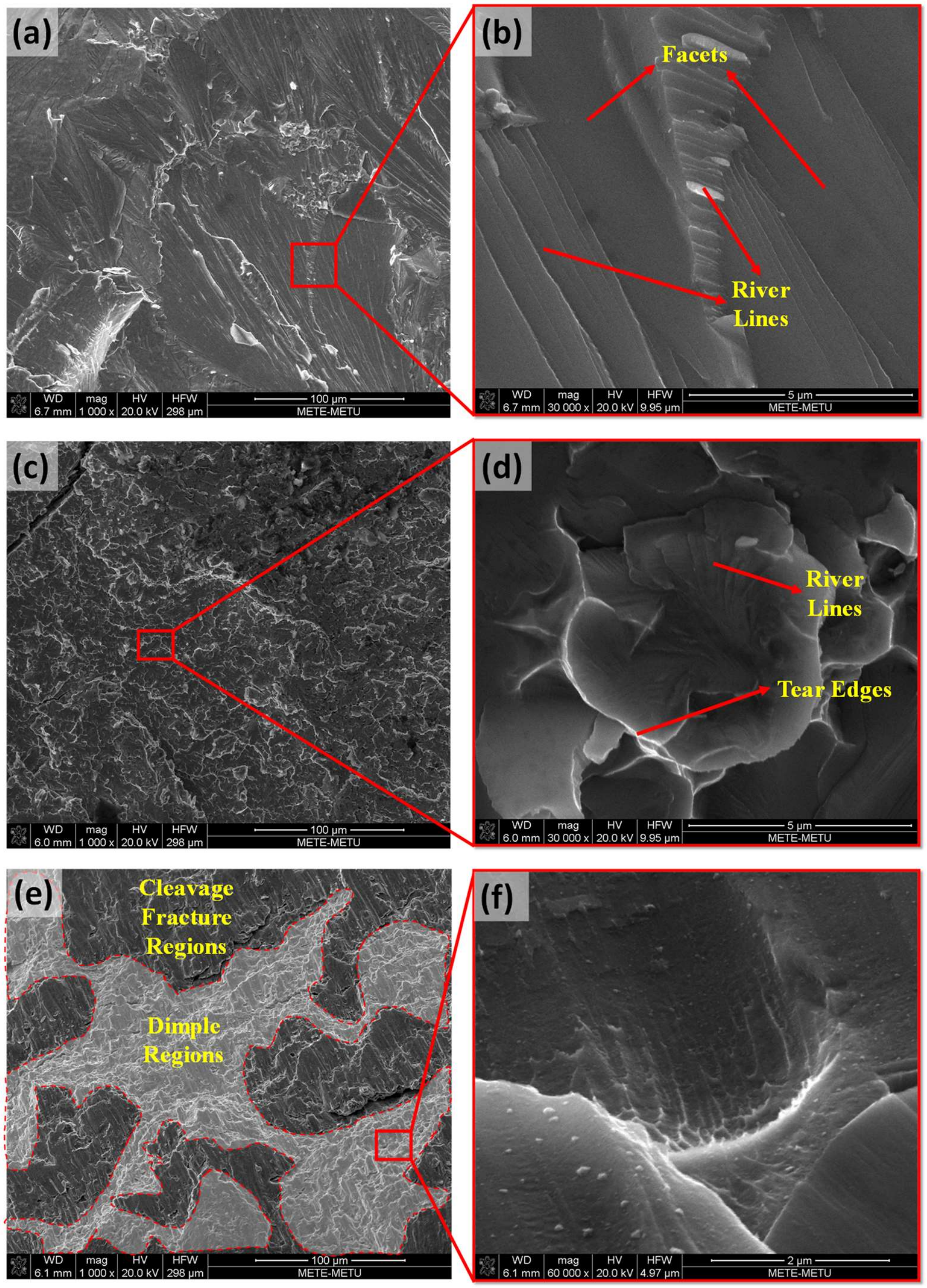

Figure 5.4. SEM image of fracture surface of 3 mm suction-cast rods; a) $Cu_{20}Ni_{20}Al_{30}Ti_{30}$ MEA (1000x), b) $Cu_{20}Ni_{20}Al_{30}Ti_{30}$ MEA (30000x), c) $Cu_{34}Ni_{22}Al_{22}Ti_{22}$ MEA (1000x), d) $Cu_{34}Ni_{22}Al_{22}Ti_{22}$ MEA (30000x), e) $Cu_{35}Ni_{25}Al_{20}Ti_{20}$ (1000x) MEA, f) $Cu_{35}Ni_{25}Al_{20}Ti_{20}$ (60000x) MEA

It seen in Figure 5.3 that $Cu_{35}Ni_{25}Al_{20}Ti_{20}$ MEA has better mechanical properties in terms of strength and ductility over the $Cu_{20}Ni_{20}Al_{30}Ti_{30}$, $Cu_{34}Ni_{22}Al_{22}Ti_{22}$ MEAs. Thus, this MEA is further investigated structurally and mechanically.

The microstructure of the 3 mm $Cu_{35}Ni_{25}Al_{20}Ti_{20}$ MEA suction-cast rods from corner to center are shown in Figure 5.5 (a) and (b), respectively. It can be clearly seen that the corner of the cylindrical samples which is in contact with cold Cu mold has fine dendrites due to local rapid solidification conditions. However, the fine dendrites slightly transform into the course dendrites and almost equiaxed grains at the center due to decreased cooling rates. As shown in Figure 5.5, two phases are present in the 3 mm $Cu_{35}Ni_{25}Al_{20}Ti_{20}$ MEA rod samples with bright and dark contrasts. The existence of two phases observed in optical microscope images is also confirmed with XRD results of the MEA (Figure 5.2). The phases observed in the optical microscope correspond to BCC and FCC dual solid solution. As seen in the XRD pattern (Figure 5.2), the integrated intensity ratios of BCC phases are higher than FCC phases. Moreover, it can be revealed that the ratios of the bright field are higher than the dark one in the optical microscope images. Therefore, it can be concluded that the bright and dark fields in Figure 5.5 correspond to BCC and FCC phases, respectively.

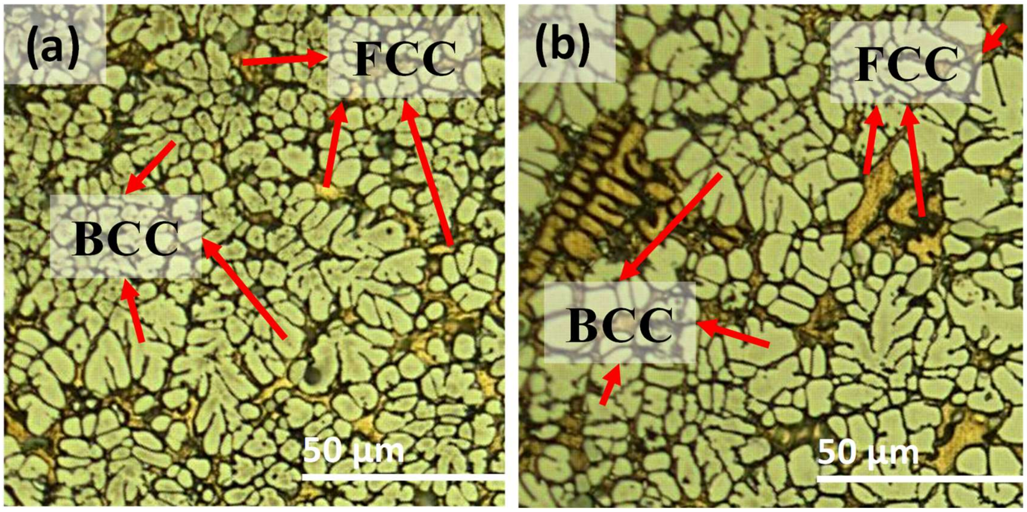

Figure 5.5. Optical microscope images (1000x) of 3 mm $Cu_{35}Ni_{25}Al_{20}Ti_{20}$ MEA suction-cast rods c) corner, d) center

EDS mapping and compositional analysis of the $Cu_{35}Ni_{25}Al_{20}Ti_{20}$ MEA are given in Figure 5.6. The MEA has two phases: grains and intergrains as seen in Figure 5.6 (a). High amount of Cu is segregated (Figure 5.6 (b, c)) in the intergrain regions, whereas grains are Cu-lean (Figure 5.6 (d-f)). The intergrain regions correspond to FCC phases as shown in Figure 5.5 with the help of XRD analysis (Figure 5.2). VEC value of the intergrain regions are calculated based on the EDS analysis of these regions (Figure 5.6 (b)). Calculated VEC value of the intergrain regions is 8.8. This value is higher than the critical FCC formation limit of the MEAs. Therefore, the expected phase of the intergrain regions because of the 8.8 VEC value, well agrees with the experimental analyses. The same calculations are performed for the grains based on the EDS analysis. The calculated VEC value of the grain regions are 6.85 which very close to upper limit of BCC formation limit. Therefore, this value proves that grains correspond to BCC phases.

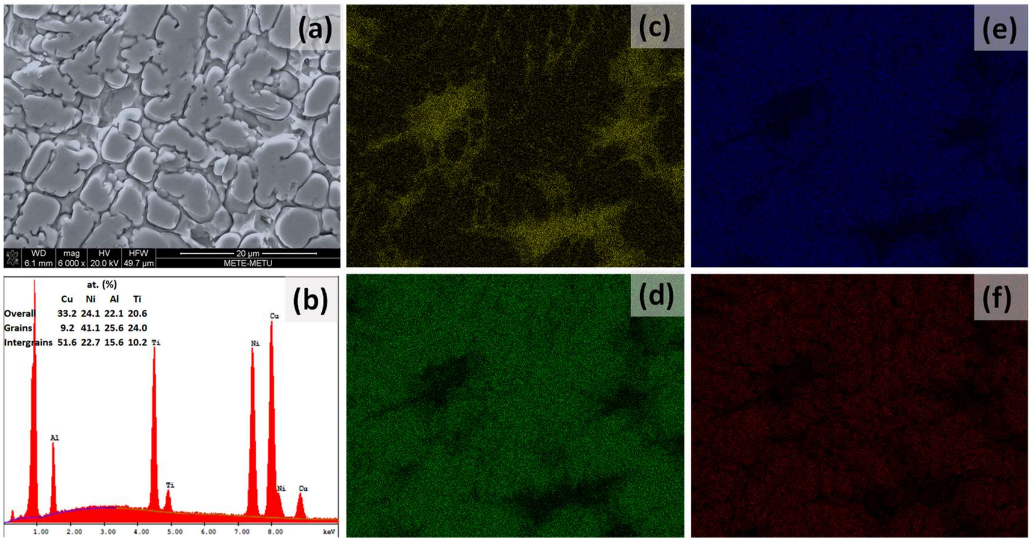

at. (%)

	Cu	Ni	Al	Ti
Overall	33.2	24.1	22.1	20.6
Grains	9.2	41.1	25.6	24.0
Intergrains	51.6	22.7	15.6	10.2

Figure 5.6. a) SEM image (6000x), b) Overall EDS spectrum, distribution of c) Cu, d) Al, e) Ni, f) Ti elements for $Cu_{35}Ni_{25}Al_{20}Ti_{20}$ MEA

Crystal lattices of the MEAs are distorted due to the different types of atoms in the structure [91]. Therefore, annealing can be done for stress relieve [92]. This process affects the mechanical properties of the MEAs. We have done annealing on the most promising $Cu_{35}Ni_{25}Al_{20}Ti_{20}$ MEA in terms of structural properties. The annealing temperature is decided based on the in-situ XRD analyses (Figure 5.8). In-situ XRD analyses reveal that the formation of ICs and grain growth occurs in a temperature interval of over 600 °C. We have chosen this critical temperature for annealing for 90 min. duration. The annealing time is the same as the total in-situ XRD analysis time at 600 °C to well discuss the results.

SEM image of 3 mm $Cu_{35}Ni_{25}Al_{20}Ti_{20}$ MEA rod of after annealing at 600 °C for 90 min. is Figure 5.7 (a). The microstructure has almost the same morphology as-cast $Cu_{35}Ni_{25}Al_{20}Ti_{20}$ MEA 3 mm rod in terms of grain size and shape of the dendrites. It can be interpreted from compression tests (Figure 5.3) that only stress relief is achieved 600 °C for 90 min. because of the increasing fracture strength and ductility.

The compression test result of the annealed $Cu_{35}Ni_{25}Al_{20}Ti_{20}$ MEA rods is shown in Figure 5.3. The sample has a yield point of around 791 MPa and maximum stress value up to 1750 MPa with 15 % ductility. The yield point of the annealed sample is close to the as-cast state. However, maximum stress is dramatically higher than as-cast state due to the strain hardening of the softened samples by removing the stresses during annealing.

The fracture surface of the $Cu_{35}Ni_{25}Al_{20}Ti_{20}$ MEA annealed 600 °C for 90 min. is shown in Figure 5.7 (b, c). The sample has a fracture surface with river lines, dimples and tear edges. The river lines cause due to the brittle BCC phases in the matrix, whereas dimples and tear edges are due to the ductile FCC phases. This fracture behavior is similar to the as-cast $Cu_{34}Ni_{22}Al_{22}Ti_{22}$ and $Cu_{35}Ni_{25}Al_{20}Ti_{20}$ MEAs. However, high amounts of the tear edges are observed in the annealed samples because of the stress relief.

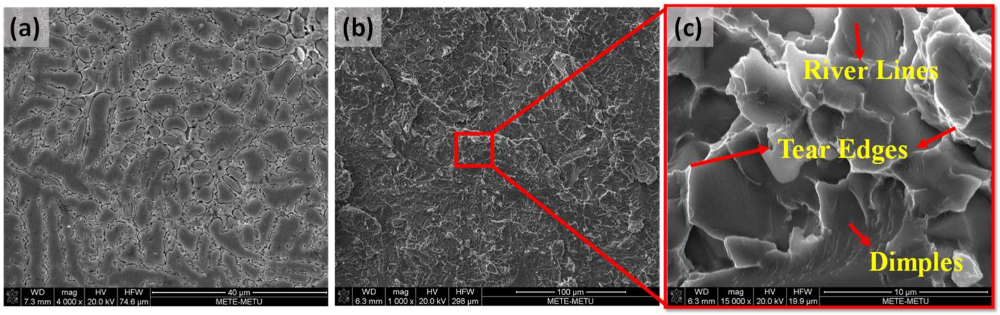

Figure 5.7. SEM images of $Cu_{35}Ni_{25}Al_{20}Ti_{20}$ MEA a) annealed at 600 °C for 90 min. (4000x), b) fracture surface after compression test (1000x), c) Zoom-in view of the fracture surface (15000x)

5.3.3. In-situ High-Temperature XRD Analyses of $Cu_{35}Ni_{25}Al_{20}Ti_{20}$ MEA

The phase stability in $Cu_{35}Ni_{25}Al_{20}Ti_{20}$ MEA rods is further analyzed using XRD with in-situ high-temperature attachment. The corresponding in-situ XRD results are shown in Figure 5.8 (a). It can be seen that 3 mm $Cu_{35}Ni_{25}Al_{20}Ti_{20}$ MEA rods consist of BCC and FCC phases with minor ICs at room temperature in as-cast form. Although the grain sizes of each phase increase with increasing temperatures, there is not any phase transformation in $Cu_{35}Ni_{25}Al_{20}Ti_{20}$ MEA up to 600 °C. After 600 °C, Bragg's reflections of ICs (with very low intensities) are started to appear on the XRD.

The broadening of the peaks at room temperature is quite higher than high-temperature XRD peaks. The sharpness of the peaks increases with increasing temperature due to the growth of the grains by thermal annealing [93]. This also results in the deconvolution of overlapping BCC(110) and FCC(111) at higher temperatures.

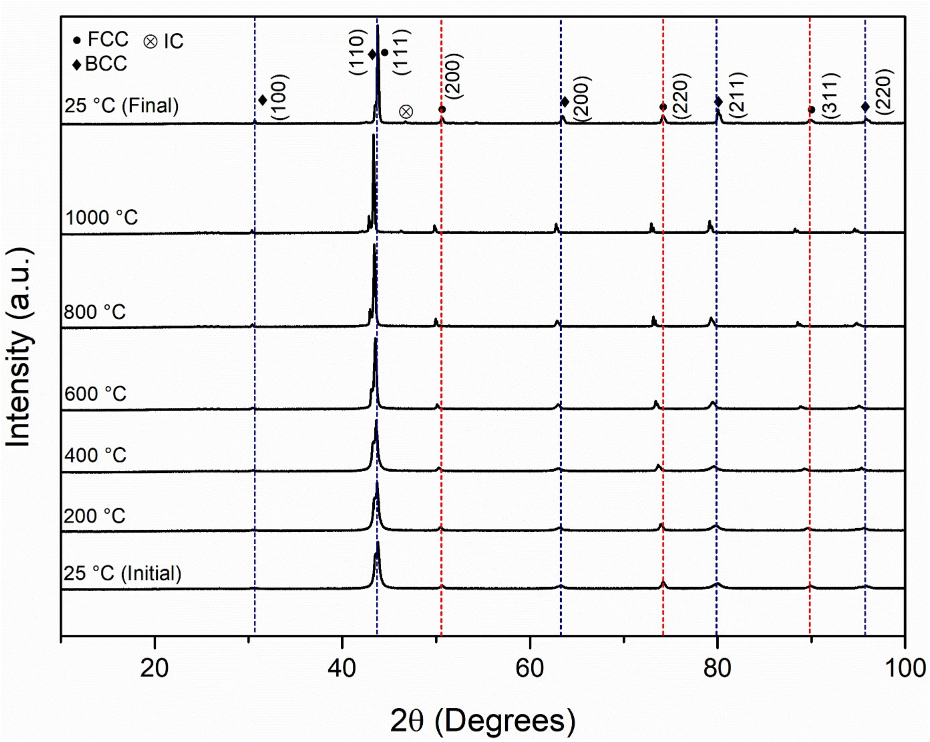

Figure 5.8. In-situ high temperature XRD analysis of 3-mm Cu_{35}Ni25$Al_{20}Ti_{20}$ MEA rod

5.4. Conclusion

In this chapter, a series of Cu-Ni-Al-Ti MEAs are designed using thermophysical calculations and Thermo-Calc software with Scheil simulation module then produced by suction casting. The MEAs are designed based on their ability to form single BCC and BCC/FCC dual-phase composite structures according to VEC values. The structural, mechanical and high-temperature stability of the produced MEAs are investigated.

The experimental results show that $Cu_{20}Ni_{20}Al_{30}Ti_{30}$ and $Cu_{25}Ni_{25}Al_{25}Ti_{25}$ MEAs have BCC phase, while $Cu_{34}Ni_{22}Al_{22}Ti_{22}$ and $Cu_{35}Ni_{25}Al_{20}Ti_{20}$ have BCC and FCC composite structure. The average hardness values of as-cast 3 mm $Cu_{20}Ni_{20}Al_{30}Ti_{30}$, $Cu_{25}Ni_{25}Al_{25}Ti_{25}$, $Cu_{34}Ni_{22}Al_{22}Ti_{22}$, and $Cu_{35}Ni_{25}Al_{20}Ti_{20}$ MEA rods are 734 (±9), 693 (±12), 537 (±13), and 427 HV (±6), respectively. Also, compression tests are applied on the MEAs to investigate their mechanical behaviors. Although $Cu_{20}Ni_{20}Al_{30}Ti_{30}$, $Cu_{25}Ni_{25}Al_{25}Ti_{25}$ MEAs fracture easily at low pressures, the mechanical properties of the $Cu_{34}Ni_{22}Al_{22}Ti_{22}$ MEA rods are increased to 184 MPa compressive stress with 1.3 % compressive strain. Moreover, 840 MPa compressive stress and 13 % compressive strain are achieved in $Cu_{35}Ni_{25}Al_{20}Ti_{20}$ MEA rods with relatively higher amounts of Cu and Ni elements.

The mechanical performance of extremely brittle $Cu_{25}Ni_{25}Al_{25}Ti_{25}$ was significantly improved by introducing FCC interdendritic region through adjusting the VEC values. The ductile FCC structure act as a glue phase between relatively brittle BCC dendrite resulting in improved ductility. This strategy of creating dual BCC/FCC phase composite MEAs represent an effective alloying technique for industrial applications.

CHAPTER 6

EFFECT OF V AND Cr ELEMENTS ON THE PROPERTIES OF DUAL PHASE LWHEAs

6.1. Introduction

Cr is commonly used in HEAs to improve their mechanical properties such as hardness, yield strength, and compressive strength [94]–[96]. The relatively small atomic radius of Cr that causes solid-solution strengthening [97], tendency to form high volume fraction of the hard σ phase [94] and its grain refinement effect [98] make it critical to use in HEAs. V is also preferred to improve the hardness and strength of the HEAs [99]–[101]. Effect of V can be divided into three groups [102]; phase transformations [100], solid-solution strengthening [99], and precipitation strengthening [100]. Therefore, the novel $Cu_{25}Ni_{25}Al_{18}Ti_{16}V_{16}$, $Cu_{29}Ni_{29}Al_{14}Ti_{14}V_{14}$, $Cu_{25}Ni_{25}Al_{18}Ti_{16}Cr_{16}$, and $Cu_{29}Ni_{29}Al_{14}Ti_{14}Cr_{14}$ LWHEAs are designed to investigate the effect of Cr and V elements on the properties of the LWHEAs. The Cu and Ni contents are increased systematically to increase the VEC value of the LWHEAs due to the influence of this critical value on the formation of the FCC phase amounts [17]. The thermophysical results of these LWHEAs are given in Table 6.1.

Table 6.1. Thermophysical parameters $Cu_{25}Ni_{25}Al_{18}Ti_{16}V_{16}$, $Cu_{29}Ni_{29}Al_{14}Ti_{14}V_{14}$, $Cu_{25}Ni_{25}Al_{18}Ti_{16}Cr_{16}$, and $Cu_{29}Ni_{29}Al_{14}Ti_{14}Cr_{14}$ LWHEAs

LWHEAs	Density (g/cm^3)	δ (%)	ΔH_{mix} (kJ/mol)	VEC	ΔS_{mix} (kJ/mol.K)	T_m (°C)	VEC Predicted Phase(s)
$Cu_{25}Ni_{25}Al_{18}Ti_{16}V_{16}$	6.20	6.50	-17.76	7.23	13.21	1323	BCC+FCC
$Cu_{29}Ni_{29}Al_{14}Ti_{14}V_{14}$	6.61	6.41	-15.41	7.77	12.84	1327	BCC+FCC
$Cu_{25}Ni_{25}Al_{18}Ti_{16}Cr_{16}$	6.36	6.61	-14.70	7.39	13.21	1318	BCC+FCC
$Cu_{29}Ni_{29}Al_{14}Ti_{14}Cr_{14}$	6.76	6.44	-12.41	7.91	12.84	1322	BCC+FCC

Relatively lower density values up to 6.20 g/cm^3 are calculated for the HEAs to consist of V as compared to LWHEAs with Cr element as seen in Table 6.1. These values are just above the density of relatively LWHEAs indicated in the literature [103]–[105]. All the ΔH_{mix} values for the LWHEAs are between -12.41 and -17.76 kJ/mol that is in a sufficient range to produce the alloys without ICs as indicated in the previous studies [16], [17]. A similar critical range is seen in δ (%) of the LWHEAs that is proposed to be less than 8.5% [106]. These two parameters let us define the alloys as the HEA. The systematic increase in the VECs is seen with respect to the higher amount of Cu and Ni elements due to their higher individual VEC values [106]. Therefore, a higher amount of FCC phases is expected in BCC and FCC composite structures based on these increasing VECs.

6.2. Experimental Analyses of the LWHEAs

6.2.1. $Cu_{25}Ni_{25}Al_{18}Ti_{16}V_{16}$ and $Cu_{29}Ni_{29}Al_{14}Ti_{14}V_{14}$ LWHEAs

XRD analyses results of the $Cu_{25}Ni_{25}Al_{18}Ti_{16}V_{16}$ and $Cu_{29}Ni_{29}Al_{14}Ti_{14}V_{14}$ LWHEAs are given in Figure 6.1. As seen in the figure, the LWHEAs have BCC and FCC composite phases with a higher amount of FCC based on their relative intensities. The FCC phases are also increased as the Cu and Ni content are increased for the $Cu_{29}Ni_{29}Al_{14}Ti_{14}V_{14}$. Also, the relative intensity of BCC(100) ordered Bragg's reflection decrease in $Cu_{29}Ni_{29}Al_{14}Ti_{14}V_{14}$ as compared to the $Cu_{25}Ni_{25}Al_{18}Ti_{16}V_{16}$ LWHEA. It is expected to have better mechanical properties with higher ductility when the reflection of ordered phases is decreased. Ma et al. investigated the effect of BCC/B2 phase on the mechanical properties of $Al_xNiCoFeCr$ HEA. They revealed that the amount of BCC/B2 phase was decreased with a decreasing amount of Al. They observed 255 MPa yield strength and ductility value was increased from 14 % to value without fracture under compressive load [53].

It is shown in Figure 6.1 that the lattice parameters of the LWHEAs decrease for both BCC and FCC phases with increasing Cu and Ni amounts due to their relatively lower atomic radii in the alloy. The lattice parameters of phases decrease from 2.961 Å to

2.946 Å for the BCC and from 3.636 Å to 3.626 Å for FCC phase. The decrease in lattice parameters is attributed to the change of the alloying composition as seen in CoCrFeNi HEAs [107].

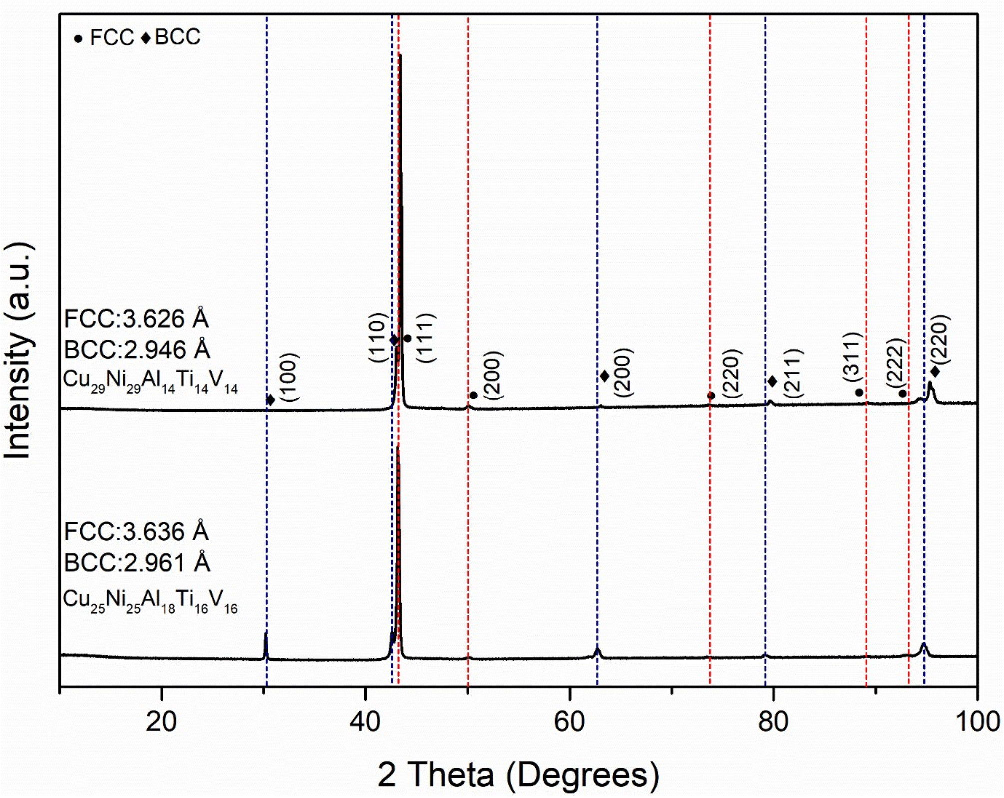

Figure 6.1. XRD pattern of 3 mm $Cu_{25}Ni_{25}Al_{18}Ti_{16}V_{16}$, and $Cu_{29}Ni_{29}Al_{14}Ti_{14}V_{14}$ LWHEA rods

The simulated phase diagram of the $Cu_{25}Ni_{25}Al_{18}Ti_{16}V_{16}$ LWHEA by Thermo-Calc software is given in Figure 6.2 (a). The LWHEA has BCC-1, BCC-2 and FCC phases up to a temperature around 990 °C and liquid phase are seen just above this temperature. Therefore, the annealing temperature is chosen just below 950 °C to prevent the melting. The homogeneous suction cast rods are milled in a high energy ball milling device (SPEX) to be able to use these samples in the powder diffraction attachment Anton Paar HTK 16N high-temperature module adapted to Bruker Advanced D8 XRD machine. The HT-XRD results of the $Cu_{25}Ni_{25}Al_{18}Ti_{16}V_{16}$

LWHEA are shown in Figure 6.2 (b). The initial room temperature (25 °C) XRD analysis shows that the sample has BCC-1, BCC-2, and FCC phases. Also, the broad peaks are seen in this pattern that indicating the decrease in the grain size due to the ball milling. When the temperature is increased to 950 °C, the peaks of the phases are seen explicitly with the decreasing broadening (increasing sharpness and intensity) in the peaks that showing an increase in the grain size upon in-situ annealing. The same phases which are BCC-1, BCC-2 and FCC are observed at this temperature, which agrees well with the simulated phase diagram. Also, no phase transformation is seen up to 950 °C. The final room temperature XRD pattern after cool down from 950 °C shows that $Cu_{25}Ni_{25}Al_{18}Ti_{16}V_{16}$ LWHEA preserve its high-temperature phases without any phase transformation.

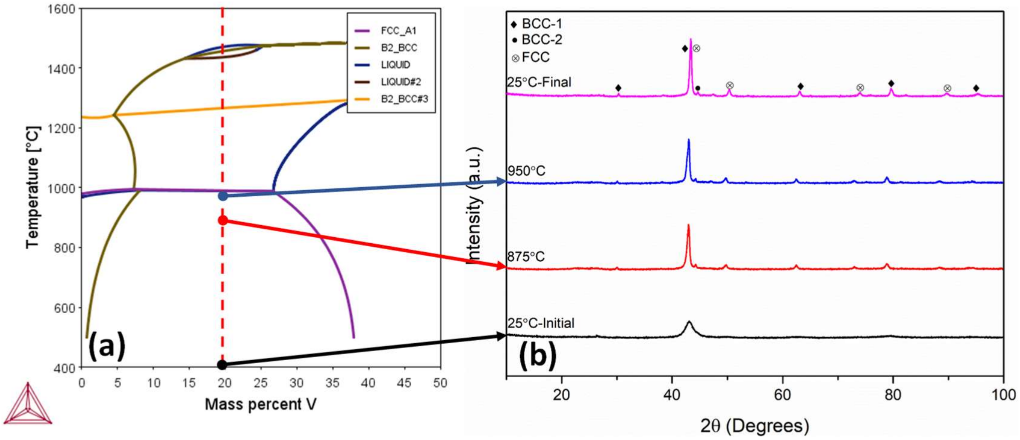

Figure 6.2. a) Simulated phase diagram, and b) high-temperature XRD analysis of $Cu_{25}Ni_{25}Al_{18}Ti_{16}V_{16}$ LWHEA

EDS mapping of as-cast 3 mm $Cu_{25}Ni_{25}Al_{14}Ti_{14}V_{14}$ rod without etching is shown in Figure 6.3. It is seen in Figure 6.3 (a) that the LWHEA consist of mainly two regions: grains and intergrains. Cu element is segregated in the grain boundaries with some amount of the other elements (Figure 6.3 (b)) due to its positive ΔH_{mix}. The EDS analysis of this region reveals that it includes Cu element over 80 % at. On the other hand, approximately 12 % at. of Cu is seen in the grains with the balanced distribution of the Ni, Al, Ti, and V elements, as seen in Figure 6.3 (c-f). Although the compositional changes are seen in the microstructure of the LWHEA, these deviations promote the formation of the FCC phase. Pradeep et al. [108] reported that the mechanical properties in terms of strength and ductility can be improved by dual phase HEAs. Therefore, the formation of secondary phases in the LWHEAs can enhance the ductility of the samples.

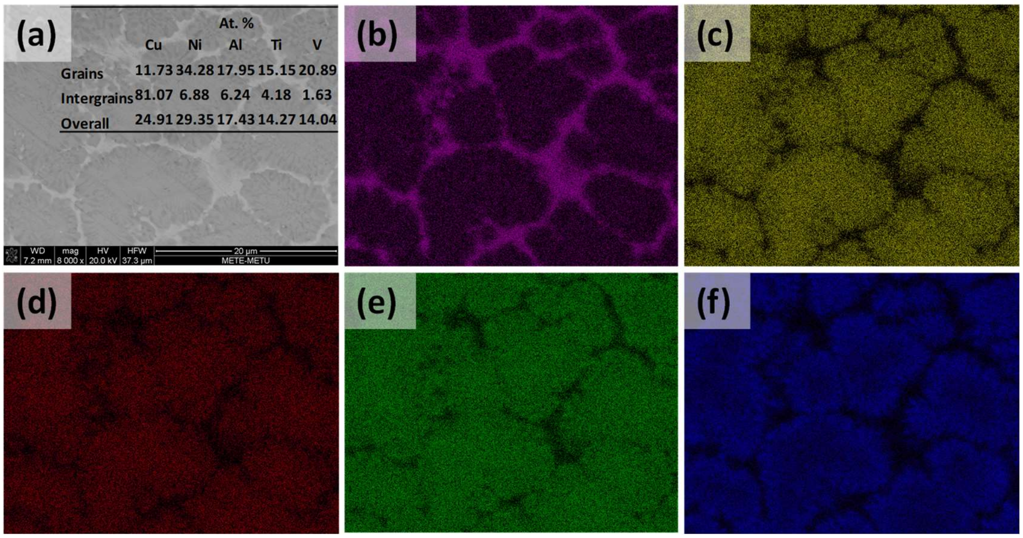

	At. %				
	Cu	Ni	Al	Ti	V
Grains	11.73	34.28	17.95	15.15	20.89
Intergrains	81.07	6.88	6.24	4.18	1.63
Overall	24.91	29.35	17.43	14.27	14.04

Figure 6.3. 3 mm unetched $Cu_{25}Ni_{25}Al_{18}Ti_{16}V_{16}$ LWHEA a) SEM image (8000x), distribution of b) Cu, c) Ni, d) Al, e) Ti, f) V

SEM images of $Cu_{25}Ni_{25}Al_{18}Ti_{16}V_{16}$ and $Cu_{29}Ni_{29}Al_{14}Ti_{14}V_{14}$ LWHEAs in as-cast conditions and heat-treated at 950 °C for 2 h. are shown in Figure 6.4. It is seen in the figures that grain growth is observed in the LWHEAs upon annealing. Also, the secondary gray phases are accumulated in the grains and grain boundaries for the heat-treated $Cu_{25}Ni_{25}Al_{18}Ti_{16}V_{16}$ (Figure 6.4 (b)) and $Cu_{29}Ni_{29}Al_{14}Ti_{14}V_{14}$ (Figure 6.4 (d)) LWHEAs. It is known from the as-cast microstructure of $Cu_{25}Ni_{25}Al_{18}Ti_{16}V_{16}$ LWHEA that mainly Cu is segregated in the grain boundaries. Thus, a higher amount of the Cu segregation is expected into intergrains upon annealing. As seen in Figure 6.4 (b, c), some voids with a size of lower than 1 μm present in the grains in both $Cu_{25}Ni_{25}Al_{18}Ti_{16}V_{16}$ and $Cu_{29}Ni_{29}Al_{14}Ti_{14}V_{14}$ LWHEAs. These voids are seen due to the gray phases observed in the grains. Our experimental results show that the Cu-rich intergrains (Figure 6.3 (b)) are more reactive as compared to Cu-lean grains (Figure 6.3 (a)) against aqua regia. Therefore, it can be interpreted that the voids correspond to Cu-rich regions similar to intergrains.

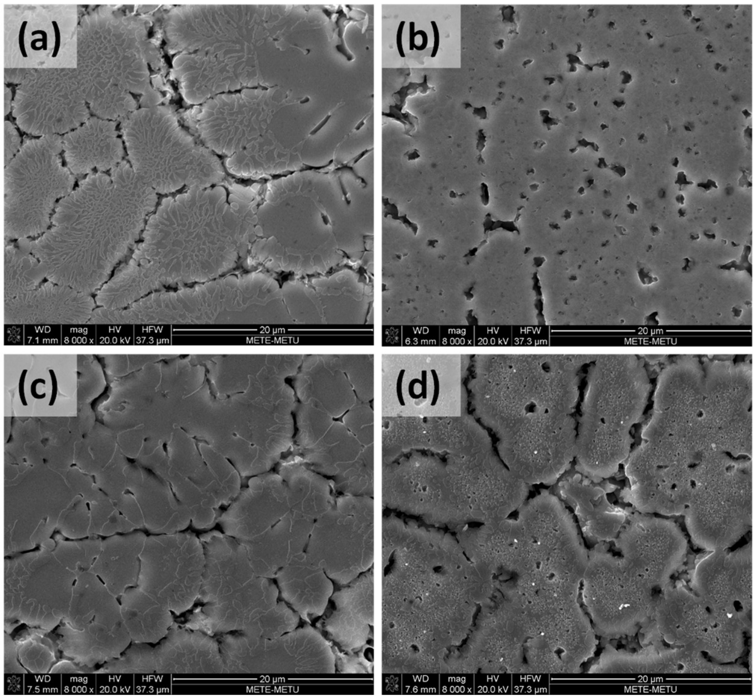

Figure 6.4. a) $Cu_{25}Ni_{25}Al_{18}Ti_{16}V_{16}$-as-cast, b) $Cu_{25}Ni_{25}Al_{18}Ti_{16}V_{16}$-900 °C-2 h., c) $Cu_{29}Ni_{29}Al_{14}Ti_{14}V_{14}$-as-cast, d) $Cu_{29}Ni_{29}Al_{14}Ti_{14}V_{14}$-900 °C-2 h.

Compression test results of as-cast and heat-treated (900 °C-2 h.) $Cu_{25}Ni_{25}Al_{18}Ti_{16}V_{16}$ and $Cu_{29}Ni_{29}Al_{14}Ti_{14}V_{14}$ LWHEAs are shown in Figure 6.5. It is seen in the figure that higher mechanical properties in terms of yield strength and ductility combination are achieved in $Cu_{29}Ni_{29}Al_{14}Ti_{14}V_{14}$ LWHEA due to its high Cu and Ni content that increase the ductility. However, the mechanical properties of these LWHEAs could not be improved upon annealing. Further annealing times or higher temperatures can be applied to enhance at least the ductility of the LWHEAs due to improvement in the microstructure and stress relief in the crystals.

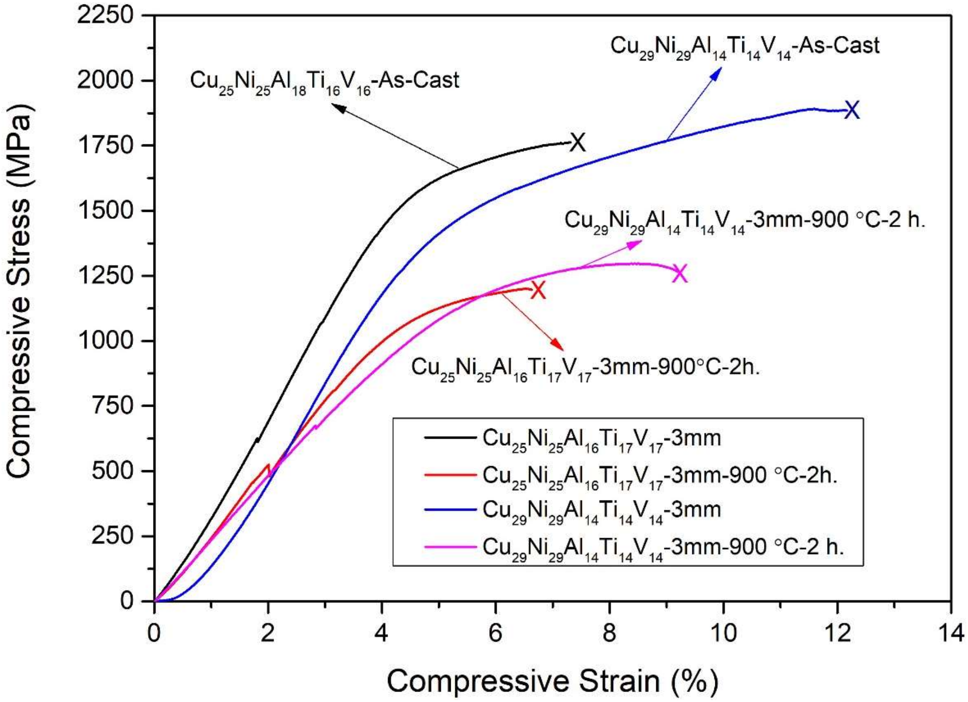

Figure 6.5. Compression test results of as-cast and heat-treated (900 °C-2 h.) $Cu_{25}Ni_{25}Al_{18}Ti_{16}V_{16}$ and $Cu_{29}Ni_{29}Al_{14}Ti_{14}V_{14}$ LWHEAs

Mechanical properties of the $Cu_{25}Ni_{25}Al_{18}Ti_{16}V_{16}$ and $Cu_{29}Ni_{29}Al_{14}Ti_{14}V_{14}$ LWHEAs retrieved from Figure 6.5 are summarized in Table 6.2. It is seen in the table that as-cast $Cu_{25}Ni_{25}Al_{18}Ti_{16}V_{16}$ LWHEA has 1400 MPa yield strength, 1760 MPa fracture strength, and 7.3 % ductility. After annealing at 900 °C for 2 h., a decrease is observed in yield strength, fracture strength and ductility which are 990 MPa, 1200 MPa and 6.5 %, respectively. This can be attributed to the formation of the secondary ordered BCC phase (BCC-2/B2) as seen in Figure 6.2 (b). Also, this phase is seen in the simulated phase diagram of the $Cu_{25}Ni_{25}Al_{18}Ti_{16}V_{16}$ LWHEA. However, no clear evidence of BCC-2 phase is seen in as-cast $Cu_{25}Ni_{25}Al_{18}Ti_{16}V_{16}$ LWHEA. Zadeh et al. [109] performed MD simulations to reveal the effect of cooling rate on the phases during rapid solidification. They revealed that the phases can be controlled in rapidly solidified HEAs to change their properties [109]. Thus, it can be interpreted that rapid solidification of the LWHEA during suction casting suppress formation of BCC-2 phase. Also, higher amounts of FCC phases are seen in as-cast state that retard the fracture of the LWHEAs under compressive load due to its relatively higher slip system as compared to BCC. The similar behavior is seen in the case of $Cu_{29}Ni_{29}Al_{14}Ti_{14}V_{14}$ LWHEA. The LWHEA has 1285 MPa yield strength, 1890 MPa fracture strength, and 12 % ductility. These properties drop to 1000 MPa yield strength, 1295 MPa fracture strength, and 9 % ductility after annealing at 900 °C for 2 h. due to the formation of higher amounts of BCC phases in equilibrium conditions Figure 6.2 (a, b) as compared to the as-cast state. In both as-cast state and after annealing, the strength of the $Cu_{29}Ni_{29}Al_{14}Ti_{14}V_{14}$ LWHEA is lower than $Cu_{25}Ni_{25}Al_{18}Ti_{16}V_{16}$. The decrease in the strength can be attributed to the relatively lower amount of BCC phases [110] in the $Cu_{29}Ni_{29}Al_{14}Ti_{14}V_{14}$ LWHEA as compared to $Cu_{25}Ni_{25}Al_{18}Ti_{16}V_{16}$. On the other hand, higher ductility values are seen in $Cu_{29}Ni_{29}Al_{14}Ti_{14}V_{14}$ LWHEA due to the presence of relatively higher FCC phases. Tang et al. [110] pointed out that increasing VEC values promotes the formation of FCC phases and their formation increase the tendency towards plasticity.

Table 6.2. Mechanical properties of the as-cast and heat-treated (900 °C-2 h.) $Cu_{25}Ni_{25}Al_{18}Ti_{16}V_{16}$ and $Cu_{29}Ni_{29}Al_{14}Ti_{14}V_{14}$ LWHEAs

LWHEAs	**YS (MPa)**	**FS (MPa)**	**Ductility (%)**
$Cu_{25}Ni_{25}Al_{18}Ti_{16}V_{16}$-as-cast	1400	1760	7.3
$Cu_{25}Ni_{25}Al_{18}Ti_{16}V_{16}$-900 °C-2 h.	990	1200	6.5
$Cu_{29}Ni_{29}Al_{14}Ti_{14}V_{14}$-as-cast	1285	1890	12.0
$Cu_{29}Ni_{29}Al_{14}Ti_{14}V_{14}$-900 °C-2 h.	1000	1295	9.0

Fractographic studies are done on 3 mm as-cast and heat-treated (900 °C for 2 h.) $Cu_{25}Ni_{25}Al_{18}Ti_{16}V_{16}$, $Cu_{29}Ni_{29}Al_{14}Ti_{14}V_{14}$, $Cu_{25}Ni_{25}Al_{18}Ti_{16}Cr_{16}$, and $Cu_{29}Ni_{29}Al_{14}Ti_{14}Cr_{14}$ LWHEA rods after compression test using SEM technique.

Fractographic analyses of $Cu_{25}Ni_{25}Al_{18}Ti_{16}V_{16}$, $Cu_{29}Ni_{29}Al_{14}Ti_{14}V_{14}$ LWHEAs in both as-cast and heat-treated conditions are shown in Figure 6.6 (a-h). It is seen in Figure 6.6 (a, b) that as-cast $Cu_{25}Ni_{25}Al_{18}Ti_{16}V_{16}$ LWHEA has a characteristic brittle appearance by cleavage mode [88]. As shown in Figure 6.6 (c, d) after heat treatment, tear edge regions are seen in the copper segregated regions (intergrains) with a dominant cleavage appearance in transgranular mode. However, it is known from the XRD pattern (Figure 6.1 (b)) of the $Cu_{25}Ni_{25}Al_{18}Ti_{16}V_{16}$ HEA that secondary BCC phases (B2) are observed after the annealing process. The formation of these phases prevent to have sufficiently enough ductility in the HEAs [110].

As seen in Figure 6.6 (e, f) $Cu_{29}Ni_{29}Al_{14}Ti_{14}V_{14}$ LWHEA has a brittle fracture surface with facets by cleavage mode [111]. Also, this sample has an intergranular fracture and tear edge appearance in the grain boundaries due to the Cu-rich FCC phases. After annealing at 900 °C for 2 h., fracture lines are seen along with the grain boundaries as seen in Figure 6.6 (g, h). It can be interpreted that after the annealing, the grain boundaries get weaker as compared to the grains. Therefore, the transgranular fracture transforms into intergranular fracture upon annealing. This makes the alloy more brittle with relatively low ductility as seen in the compression test (Figure 6.5).

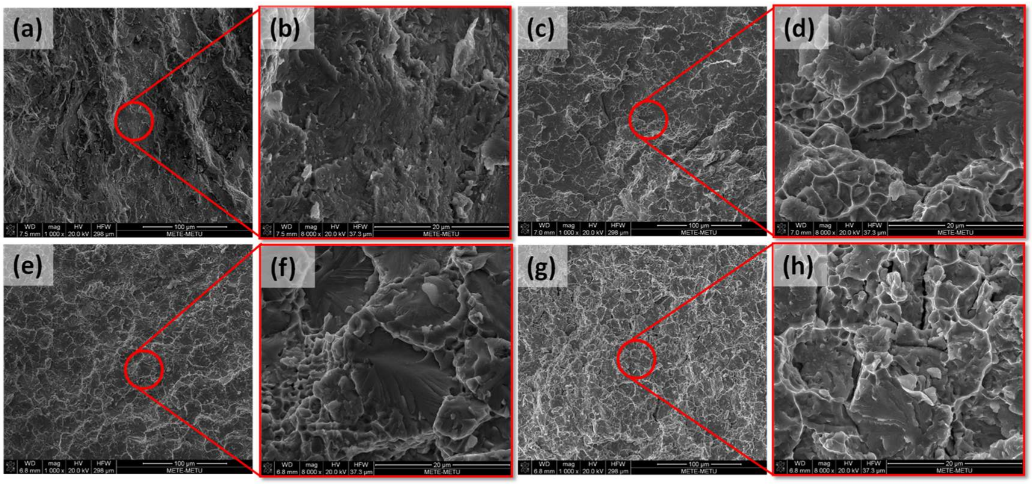

Figure 6.6. Fracture surface SEM images of a) $Cu_{25}Ni_{25}Al_{18}Ti_{16}V_{16}$ as-cast (1000x), b) $Cu_{25}Ni_{25}Al_{18}Ti_{16}V_{16}$ as-cast (8000x), c) $Cu_{25}Ni_{25}Al_{18}Ti_{16}V_{16}$-900 °C for 2 h. (1000x), d) $Cu_{25}Ni_{25}Al_{18}Ti_{16}V_{16}$-900 °C for 2 h. (8000x), e) $Cu_{29}Ni_{29}Al_{14}Ti_{14}V_{14}$ as-cast (1000x), f) $Cu_{29}Ni_{29}Al_{14}Ti_{14}V_{14}$ as-cast (8000x), g) $Cu_{29}Ni_{29}Al_{14}Ti_{14}V_{14}$-900 °C for 2 h. (1000x), h) $Cu_{29}Ni_{29}Al_{14}Ti_{14}V_{14}$-900 °C for 2 h. (8000x)

6.2.2. $Cu_{25}Ni_{25}Al_{18}Ti_{16}Cr_{16}$, and $Cu_{29}Ni_{29}Al_{14}Ti_{14}Cr_{14}$ LWHEAs

XRD pattern of the $Cu_{25}Ni_{25}Al_{18}Ti_{16}Cr_{16}$, and $Cu_{29}Ni_{29}Al_{14}Ti_{14}Cr_{14}$ 3 mm suction cast LWHEAs rods are shown in Figure 6.7. Both samples consist of two BCC phases (BCC-1 and BCC-2) and an FCC phase. The BCC-1 phase corresponds to ordered BCC (B2) due to its (100) reflection. The lattice parameters decrease from 3.640 Å to 3.628 Å for the FCC, from 2.957 Å to 2.949 Å for the BCC-1, and from 2.891 Å to 2.883 Å for the BCC-1 with increasing Cu and Ni content in the LWHEAs because of the relatively smaller atomic radii of these elements.

The relative intensity of the FCC phase in the $Cu_{29}Ni_{29}Al_{14}Ti_{14}Cr_{14}$ is higher than in $Cu_{25}Ni_{25}Al_{18}Ti_{16}Cr_{16}$. This result proves that increasing amounts of Cu and Ni in the LWHEA promote the formation of the FCC phases as predicted in Table 6.1.

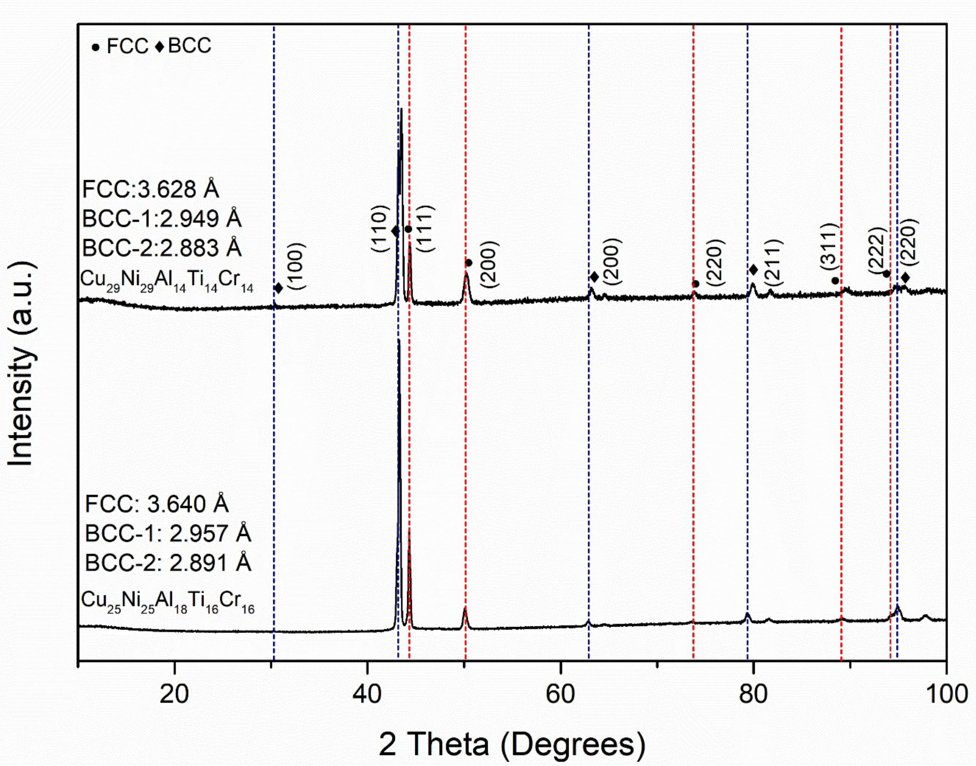

Figure 6.7. XRD pattern of 3 mm $Cu_{25}Ni_{25}Al_{18}Ti_{16}Cr_{16}$, and $Cu_{29}Ni_{29}Al_{14}Ti_{14}Cr_{14}$ LWHEA rods

Simulated phase diagram of $Cu_{25}Ni_{25}Al_{18}Ti_{16}Cr_{16}$ HEA is shown in Figure 6.8 (a). The phase diagram shows that the LWHEA composed of two BCC phases (BCC_B2 and BCC_B2-2) and FCC phases approximately below 950 °C up to room temperature. These results are verified experimentally by HT-XRD and the patterns are shown in Figure 6.8 (b). A similar experimental procedure with $Cu_{25}Ni_{25}Al_{18}Ti_{16}V_{16}$ is done for in-situ HT-XRD experiments due to their similar phase diagrams. The experimental results reveal that the sample preserves its room temperature phases up to 925 °C. The broadening of the peaks decreases at 925 °C due to the increasing grain size of the LWHEA. The sample is cooled down to room temperature (25 °C) in a few minutes. As seen in Figure 6.8 (b), the sample has the same phases and similar XRD patterns at 925 °C and 25 °C.

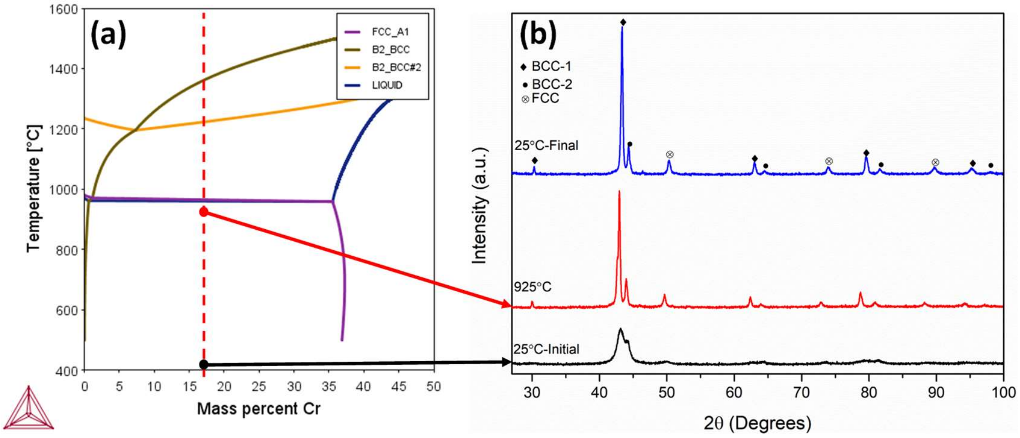

Figure 6.8. a) Simulated phase diagram, and b) high-temperature XRD analysis of $Cu_{25}Ni_{25}Al_{18}Ti_{16}Cr_{16}$ LWHEA

EDS mapping of unetched 3 mm as-cast $Cu_{25}Ni_{25}Al_{18}Ti_{16}Cr_{16}$ LWHEA is seen in Figure 6.9. The sample has grains and intergrains in the microstructure as shown in Figure 6.9 (a). Intergrain regions (Figure 6.9 (b)) are composed of Cu element higher than 77.50 % at. due to its positive ΔH_{mix} value that causes segregation. This Cu-rich region promotes the formation of FCC phases like Cu solid solution. Despite this, almost a homogenous distribution of the Ni, Al, T, and Cr with lower than 10.50 at. % Cu is seen in the grain regions (Figure 6.9 (c-f)). These regions correspond to the

BCC phases due to the lower VEC value of the elements accumulated in these regions that cause a lower overall VEC value below 6.87. It is known that if the VEC value is lower than this critical value, BCC phases are expected in the HEAs [17]. Therefore, it is expected to have higher yield and fracture strength due to BCC and also higher ductility due to the Cu-rich FCC phases.

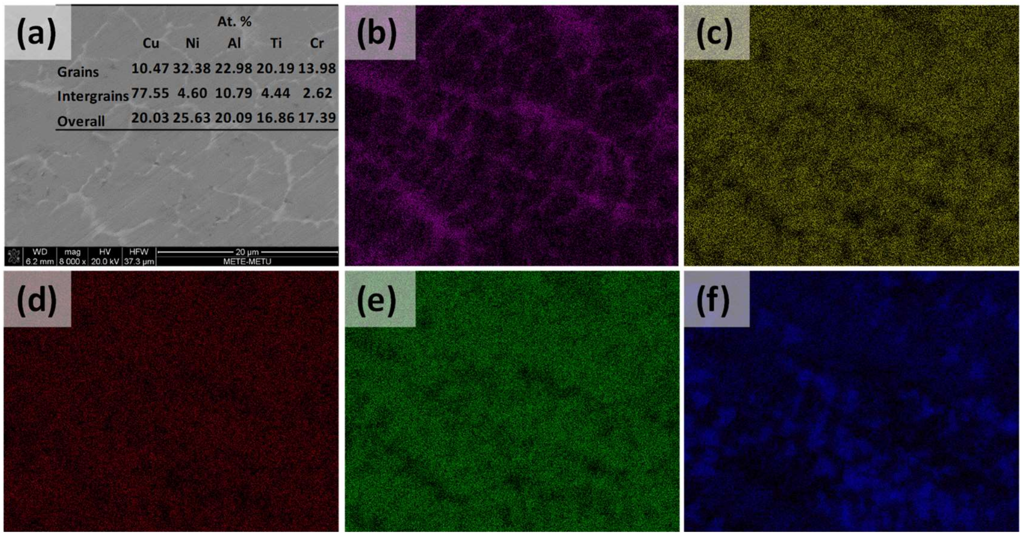

At. %	Cu	Ni	Al	Ti	Cr
Grains	10.47	32.38	22.98	20.19	13.98
Intergrains	77.55	4.60	10.79	4.44	2.62
Overall	20.03	25.63	20.09	16.86	17.39

Figure 6.9. 3 mm unetched $Cu_{25}Ni_{25}Al_{18}Ti_{16}Cr_{16}$ LWHEA a) SEM image (8000x), distribution of b) Cu, c) Ni, d) Al, e) Ti, f) Cr

The microstructure of as-cast and heat-treated (at 900 °C for 2 h.) 3 mm $Cu_{25}Ni_{25}Al_{18}Ti_{16}Cr_{16}$, and $Cu_{29}Ni_{29}Al_{14}Ti_{14}Cr_{14}$ LWHEA rods after etching are shown in Figure 6.10. The grain size of these samples increases after the annealing for both samples. The unetched microstructure and its EDS mapping (Figure 6.9) show that the intergrain regions composed of a Cu-rich composition. Therefore, the etched regions correspond to the FCC regions and it is seen that these regions have low resistance in aqua regia. Also, it is expected to have Cu diffusion to grain boundaries or Cu accumulation in the grains during the heat treatment process. Higher Cu segregation is seen in $Cu_{29}Ni_{29}Al_{14}Ti_{14}Cr_{14}$ LWHEA (Figure 6.10 (c, d)) due to its higher Cu content as compared to the $Cu_{25}Ni_{25}Al_{18}Ti_{16}Cr_{16}$ LWHEA (Figure 6.10 (a, b)). Therefore, the etched regions (voids) in the grains can be interpreted as Cu-rich regions. These composite structures with BCC and FCC phases can enhance both the strength and ductility of the LWHEAs.

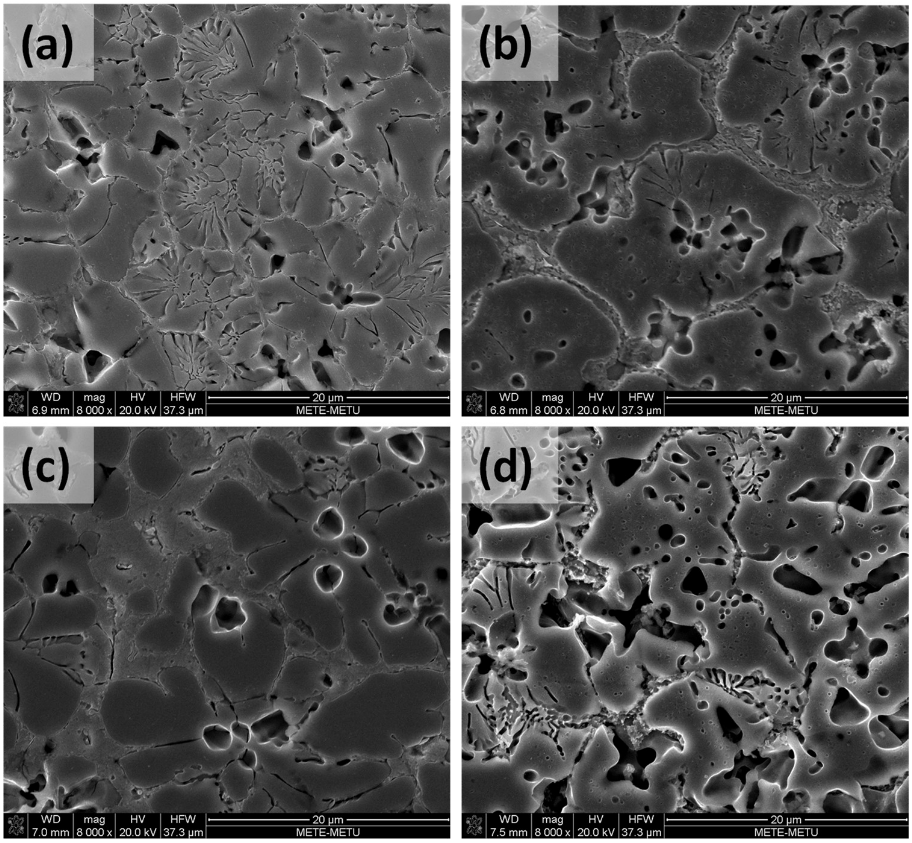

Figure 6.10. a) $Cu_{25}Ni_{25}Al_{18}Ti_{16}Cr_{16}$-as-cast, b) $Cu_{25}Ni_{25}Al_{18}Ti_{16}Cr_{16}$-900 °C-2 h., c) $Cu_{29}Ni_{29}Al_{14}Ti_{14}Cr_{14}$-as-cast, d) $Cu_{29}Ni_{29}Al_{14}Ti_{14}Cr_{14}$-900 °C-2 h.

Compression test results of $Cu_{25}Ni_{25}Al_{18}Ti_{16}Cr_{16}$ and $Cu_{29}Ni_{29}Al_{14}Ti_{14}Cr_{14}$ LWHEAs in as-cast state and heat-treated at 900 °C for 2 h. are seen in Figure 6.11. The strength of the LWHEA is increased with their low Cu and Ni content. On the other hand, ductility values are increased with increasing Cu and Ni content due to the formation of higher amounts of FCC phases (Figure 6.7). In general, the heat treatment process causes a softening in the LWHEAs that increase in the ductility with a slight decrease in yield strength for both the $Cu_{25}Ni_{25}Al_{18}Ti_{16}Cr_{16}$ and $Cu_{29}Ni_{29}Al_{14}Ti_{14}Cr_{14}$ LWHEAs.

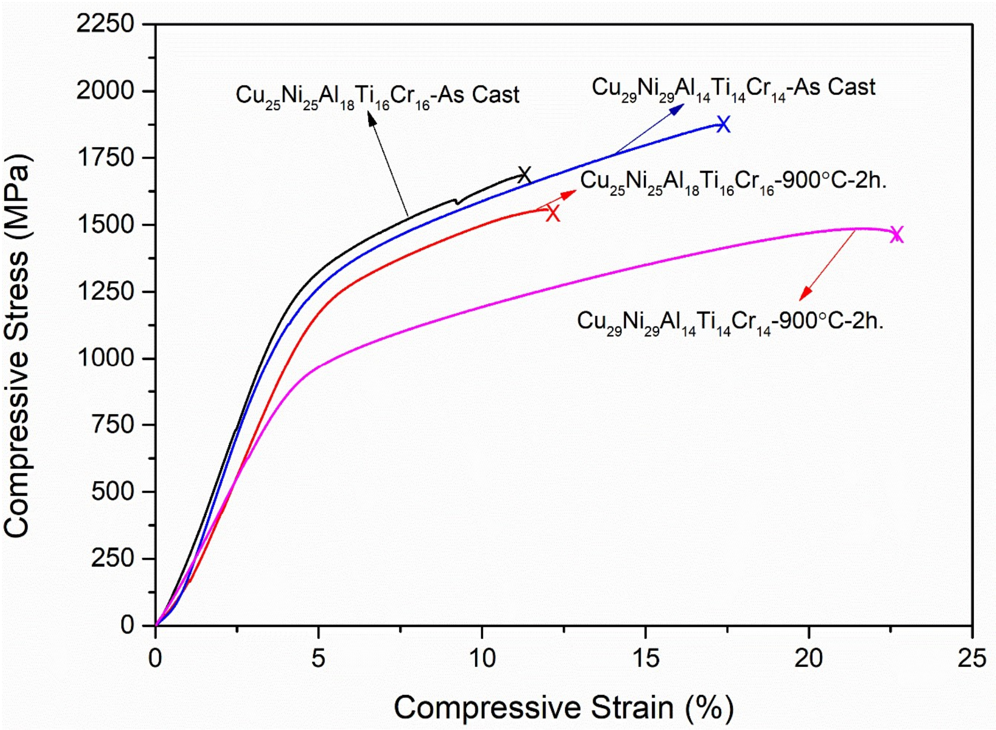

Figure 6.11. Compression test results of as-cast and heat-treated (900 °C-2 h.) $Cu_{25}Ni_{25}Al_{18}Ti_{16}Cr_{16}$ and $Cu_{29}Ni_{29}Al_{14}Ti_{14}Cr_{14}$ LWHEAs

The mechanical properties of the $Cu_{25}Ni_{25}Al_{18}Ti_{16}Cr_{16}$ and $Cu_{29}Ni_{29}Al_{14}Ti_{14}Cr_{14}$ LWHEAs are summarized in Table 6.3. It is seen that $Cu_{25}Ni_{25}Al_{18}Ti_{16}Cr_{16}$ LWHEA has 1170 MPa yield strength, 1685 MPa fracture strength and 11.2 % ductility in the as-cast state. These strength values drop to 1050 MPa yield strength, 1555 MPa fracture strength and, however, the ductility increased slightly to 12 %. The decrease in the strength occurs because of the stress relief in the LWHEA during annealing. In the case of as-cast $Cu_{29}Ni_{29}Al_{14}Ti_{14}Cr_{14}$ LWHEA, although it has lower yield strength with a value of 1080 MPa as compared to $Cu_{25}Ni_{25}Al_{18}Ti_{16}Cr_{16}$ LWHEA, it has a higher fracture strength up to 1870 MPa. Also, the ductility of the $Cu_{29}Ni_{29}Al_{14}Ti_{14}Cr_{14}$ LWHEA is increased to 17.3 % because of the higher amount of the relatively soft FCC. Upon annealing, the strength values of the $Cu_{29}Ni_{29}Al_{14}Ti_{14}Cr_{14}$ LWHEA decrease to 855 MPa yield strength and 1485 MPa fracture strength. However, the ductility of the LWHEA increases to 22.6 %

dramatically that improves its forming ability. The decrease in the strength and increase in ductility can be attributed to the stress relief and Cu segregation upon annealing. Also, Cu segregation promotes an increase in FCC phases in the grain boundaries that has a critical effect on the ductility.

Table 6.3. Mechanical properties of the as-cast and heat treated (900 °C-2 h.) $Cu_{25}Ni_{25}Al_{18}Ti_{16}Cr_{16}$ and $Cu_{29}Ni_{29}Al_{14}Ti_{14}Cr_{14}$ LWHEAs

LWHEAs	YS (MPa)	FS (MPa)	Ductility (%)
$Cu_{25}Ni_{25}Al_{18}Ti_{16}Cr_{16}$-as-cast	1170	1685	11.2
$Cu_{25}Ni_{25}Al_{18}Ti_{16}Cr_{16}$-900 °C-2 h.	1050	1555	12.0
$Cu_{29}Ni_{29}Al_{14}Ti_{14}Cr_{14}$-as-cast	1080	1870	17.3
$Cu_{29}Ni_{29}Al_{14}Ti_{14}Cr_{14}$-900 °C-2 h.	855	1485	22.6

The fracture surfaces of as-cast and annealed (900 °C for 2 h.) $Cu_{25}Ni_{25}Al_{18}Ti_{16}Cr_{16}$ and $Cu_{29}Ni_{29}Al_{14}Ti_{14}Cr_{14}$ LWHEAs are shown in Figure 6.12 (a-h). It is seen in Figure 6.12 (a, b) that as-cast $Cu_{25}Ni_{25}Al_{18}Ti_{16}Cr_{16}$ LWHEA has transgranular river lines in the grains tear edges in the grain boundaries. This characteristic appearance [112] indicates that the crack propagates along either grain boundaries or transgranular cleavage planes. After the annealing process, distinct tear edge formations are seen in $Cu_{25}Ni_{25}Al_{18}Ti_{16}Cr_{16}$ due to the Cu segregation that promotes the higher amount of FCC phases which is inconsistent with other reports in the literature [98], [113], [114]. As shown in Figure 6.12 (c, d), $Cu_{25}Ni_{25}Al_{18}Ti_{16}Cr_{16}$ LWHEA has dimples in the fracture surface. This makes the LWHEA more ductile as seen in the compression test (Figure 6.11). The annealing process forms distinct dimples in the $Cu_{29}Ni_{29}Al_{14}Ti_{14}Cr_{14}$ due to the high volume ratio of the Cu-rich FCC ductile intergrains. Therefore, when the Cu and Ni content of the LWHEA is increased to produce $Cu_{29}Ni_{29}Al_{14}Ti_{14}Cr_{14}$ LWHEA, more ductile fracture surfaces with tear edges and dimples are seen in as-cast and heat-treated $Cu_{29}Ni_{29}Al_{14}Ti_{14}Cr_{14}$ LWHEA as compared to $Cu_{25}Ni_{25}Al_{18}Ti_{16}Cr_{16}$ LWHEA. These images also well agree with the compression test results (Figure 6.11).

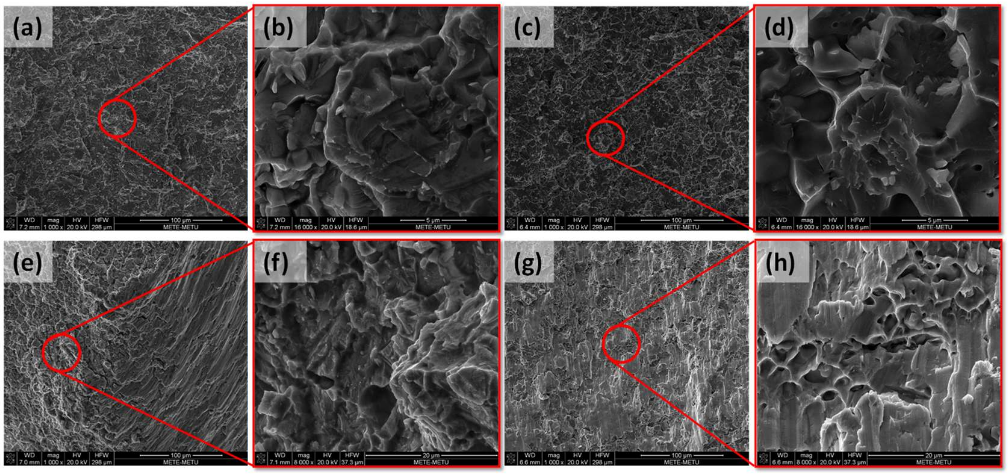

Figure 6.12. Fracture surface SEM images of a) $Cu_{25}Ni_{25}Al_{18}Ti_{16}Cr_{16}$ as-cast (1000x), b) $Cu_{25}Ni_{25}Al_{18}Ti_{16}Cr_{16}$ as-cast (8000x), c) $Cu_{25}Ni_{25}Al_{18}Ti_{16}Cr_{16}$-900 °C for 2 h. (1000x), d) $Cu_{25}Ni_{25}Al_{18}Ti_{16}Cr_{16}$-900 °C for 2 h. (8000x), e) $Cu_{29}Ni_{29}Al_{14}Ti_{14}Cr_{14}$ as-cast (1000x), f) $Cu_{29}Ni_{29}Al_{14}Ti_{14}Cr_{14}$ as-cast (8000x), g) $Cu_{29}Ni_{29}Al_{14}Ti_{14}Cr_{14}$-900 °C for 2 h. (1000x), h) $Cu_{29}Ni_{29}Al_{14}Ti_{14}Cr_{14}$-900 °C for 2 h. (8000x)

6.3. Hardness Comparison of the LWHEAs

Hardness comparison of $Cu_{25}Ni_{25}Al_{18}Ti_{16}V_{16}$, $Cu_{29}Ni_{29}Al_{14}Ti_{14}V_{14}$, $Cu_{25}Ni_{25}Al_{18}Ti_{16}Cr_{16}$, and $Cu_{29}Ni_{29}Al_{14}Ti_{14}Cr_{14}$ LWHEAs in as-cast state and annealed at 900 °C for 2 h. is given in Figure 6.13. It is seen in the figure that the hardness values of the LWHEAs decrease after annealing. The average hardness values of as-cast $Cu_{25}Ni_{25}Al_{18}Ti_{16}V_{16}$, $Cu_{29}Ni_{29}Al_{14}Ti_{14}V_{14}$ LWHEAs are 514, 434 HV, respectively. These values drop to 412, 406 HV after annealing. Although a dramatic decrease is seen in the hardness of $Cu_{25}Ni_{25}Al_{18}Ti_{16}V_{16}$, a slight decrease is observed in $Cu_{29}Ni_{29}Al_{14}Ti_{14}V_{14}$ LWHEAs. These decrease can be correlated with the stress relief and phase transformation from (ordered) BCC-1 (B2) to BCC-2 upon annealing in the LWHEAs as seen in Figure 6.2 (b). It can be interpreted that BCC-2 phase has a relatively soft structure as compared to the BCC-1.

As seen in Figure 6.13 the hardness values of $Cu_{25}Ni_{25}Al_{18}Ti_{16}Cr_{16}$, $Cu_{29}Ni_{29}Al_{14}Ti_{14}Cr_{14}$ LWHEAs drop from 436 to 392 HV, and 420 to 338 HV, respectively after annealing. The phase transformation from BCC to FCC (Figure 6.7) affect the decrease in hardness because of the relatively soft FCC phases. It is shown in Figure 6.2 and Figure 6.8 that the relative amount of FCC phases increases upon annealing. $Cu_{29}Ni_{29}Al_{14}Ti_{14}Cr_{14}$ LWHEAs include higher Cu content that promotes the formation FCC phases dramatically as compared to the $Cu_{25}Ni_{25}Al_{18}Ti_{16}Cr_{16}$. Therefore, a significant decrease in hardness is observed in $Cu_{29}Ni_{29}Al_{14}Ti_{14}Cr_{14}$ LWHEAs.

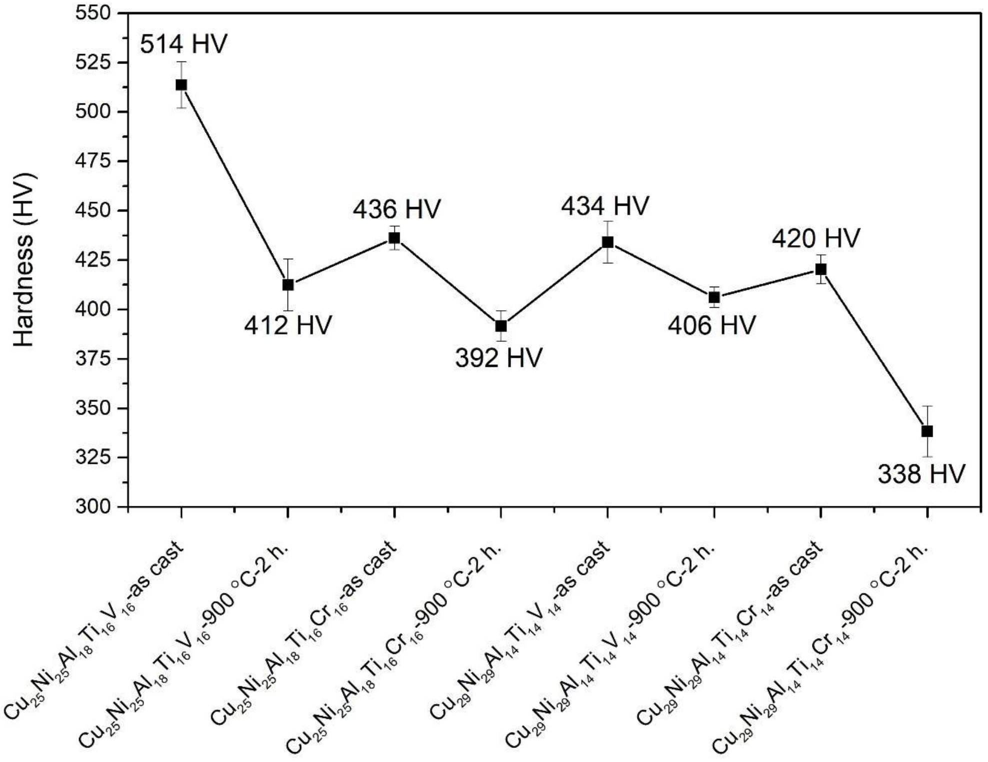

Figure 6.13. Hardness values of as-cast and heat-treated $Cu_{25}Ni_{25}Al_{18}Ti_{16}V_{16}$, $Cu_{29}Ni_{29}Al_{14}Ti_{14}V_{14}$, $Cu_{25}Ni_{25}Al_{18}Ti_{16}Cr_{16}$, and $Cu_{29}Ni_{29}Al_{14}Ti_{14}Cr_{14}$ LWHEAs

6.4. Comparison of $Cu_{29}Ni_{29}Al_{14}Ti_{14}Cr_{14}$ LWHEA and Most Common Alloys

The room temperature yield strength and density comparison of the CCAs (HEAs) with commercial alloys such as Mg, Al, Ti, Fe, Ni based and refractory alloys for structural applications are given in Figure 6.14 using logarithmic scale. The dashed lines indicate the performance index for three loading conditions: uniaxial loading (slope, s = 1), beam bending, (s = 3/2), panel bending (s = 2). If the properties of the materials are above these lines, stronger structures can be made from that alloys. In fact, all the data are below these lines due to the differences between the loading conditions causing the differences different results. Therefore, the best alloy for uniaxial tension whereas Mg alloys are for the beam and panel bending at room temperature [48].

The most promising LWHEA in this thesis is 3 mm $Cu_{29}Ni_{29}Al_{14}Ti_{14}Cr_{14}$ LWHEA rod produced by arc meting and suction casting. The LWHEA has a BCC and FCC composite structure with 855 MPa yield strength and 6.76 g/cm^3 (6760 kg/m^3) density and 22.6 % ductility. This LWHEA shoes better mechanical properties as compared to Mg, Al, Ti and also most of the Fe, Ni alloys and 3d transition metal (TM) CCAs as seen in Figure 6.14. The light CCAs indicated by Gorsee et al. [48], are between Al and Ti alloys. Although the $Cu_{29}Ni_{29}Al_{14}Ti_{14}Cr_{14}$ LWHEA has relatively higher density as compared to light CCAs, the yield strength of the LWHEA is higher than CCAs, significantly.

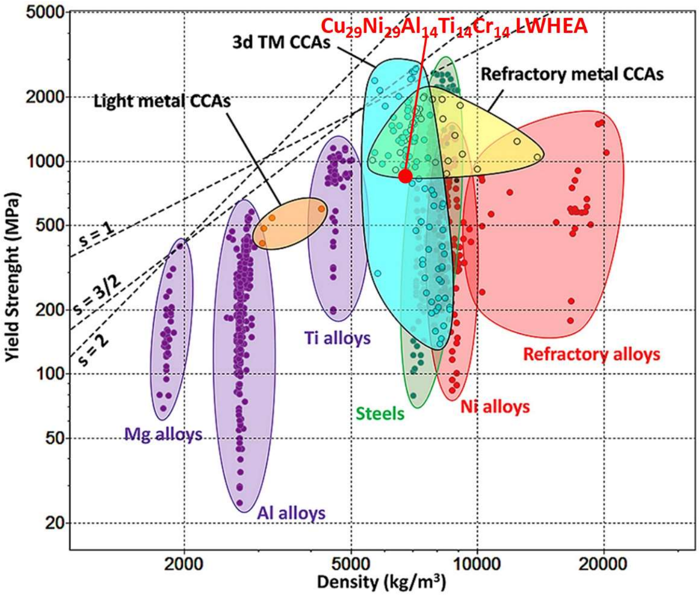

Figure 6.14. Comparison of yield strength and density of conventional metal alloys, CCAs (HEAs) and $Cu_{29}Ni_{29}Al_{14}Ti_{14}Cr_{14}$ LWHEA at room temperature [48]

6.5. Scale-Up Production of $Cu_{29}Ni_{29}Al_{14}Ti_{14}Cr_{14}$ LWHEA

$Cu_{29}Ni_{29}Al_{14}Ti_{14}Cr_{14}$ LWHEAs showing better mechanical properties in arc-melter and suction casting experiments are produced by induction casting. The alloy mixture are prepared from industrial grade Cu (99.0 wt.%), Ni (99.0 wt.%), Al (99.0 wt.%), Ti (99.0 wt.%), and Cr (98.0 wt.%). The melting is done in an alumina crucible under vacuum up to (10^{-1} mbar). The homogenization of the alloys is done by eddy current during induction melting. The alloys are cast into a cylindrical copper mold with 5 mm diameter and solidified under vacuum environment without any further cooling operation. The same experimental analysis and heat treatment procedure (900 °C for 2 h.) with the samples produced from high purity raw materials by arc-melter is performed. Then, compression tests are carried out on the samples according to ASTM E9-09 standard. Compression tests results of 5 mm $Cu_{29}Ni_{29}Al_{14}Ti_{14}Cr_{14}$ LWHEA rods are shown in Figure 6.15. This LWHEA has 944 MPa yield strength, 1347 MPa fracture strength and 8.25 % ductility in as-cast condition. Annealing at 900 °C for 2 h. is performed on the LWHEA to investigate the effect of heat treatment processes. As stress relief is observed in the samples, yield strength slightly drops to 902 MPa with 1332 MPa fracture strength and 12.71 % ductility. The impurity elements present in the industrial grade raw materials may cause additional small amount of phases (i.e. intermetallic compounds) causing a decrease in the ductility as compared to the samples produced from high purity raw materials. However, higher yield and fracture strength are observed as compared to the $Cu_{29}Ni_{29}Al_{14}Ti_{14}Cr_{14}$ LWHEAs produced form high purity raw materials by arc-melter and suction casting.

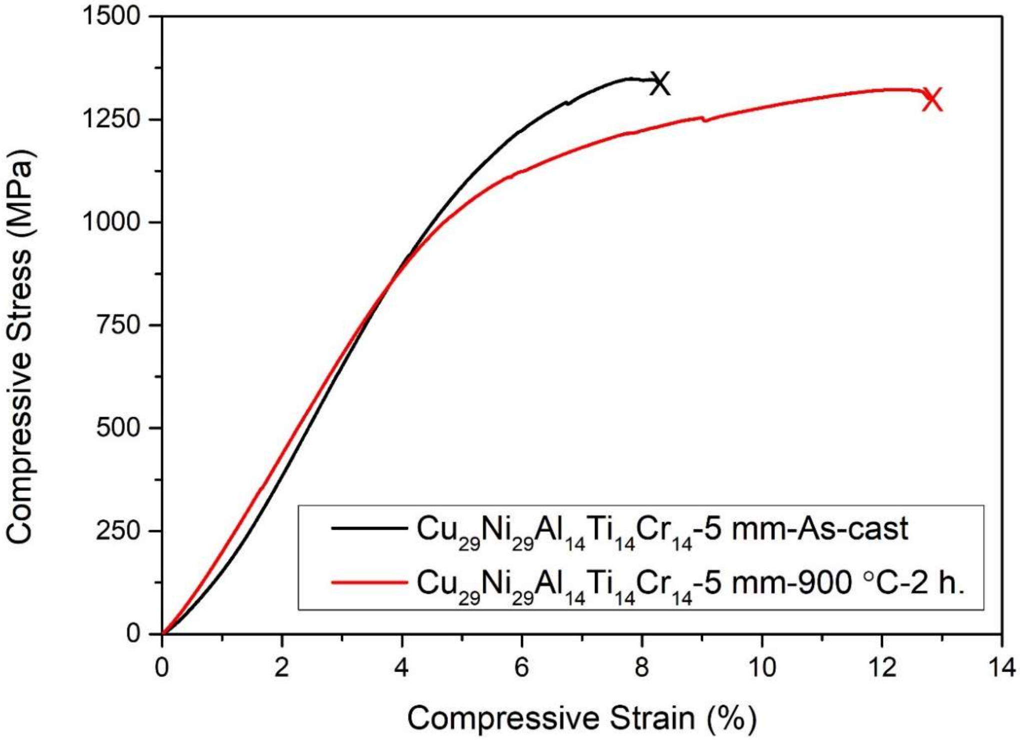

Figure 6.15. Compression test results of as-cast and heat-treated (900 °C-2 h.) $Cu_{29}Ni_{29}Al_{14}Ti_{14}Cr_{14}$ LWHEAs produced by induction casting

6.6. Conclusion

Novel LWHEAs are designed with the addition of V and Cr elements in Cu-Ni-Al-Ti MEAs and $Cu_{25}Ni_{25}Al_{18}Ti_{16}V_{16}$, $Cu_{29}Ni_{29}Al_{14}Ti_{14}V_{14}$, $Cu_{25}Ni_{25}Al_{18}Ti_{16}Cr_{16}$, and $Cu_{29}Ni_{29}Al_{14}Ti_{14}Cr_{14}$ LWHEAs are produced.

The 3 mm $Cu_{25}Ni_{25}Al_{18}Ti_{16}V_{16}$, $Cu_{29}Ni_{29}Al_{14}Ti_{14}V_{14}$ LWHEA rods have BCC and FCC in cast state. An additional BCC-2 (B2) phase is seen upon annealing at 900 °C for 2 h. that makes the LWHEAs brittle and decrease the ductility as compared to the as-cast state. However, the decrease in hardness is observed after annealing process due to the stress relief.

3 mm $Cu_{25}Ni_{25}Al_{18}Ti_{16}Cr_{16}$, $Cu_{29}Ni_{29}Al_{14}Ti_{14}Cr_{14}$ LWHEA rods have FCC, BCC-1 and BCC-2 phases at room temperature in the as-cast state. The samples preserve their phases upon annealing up to 925 °C. However, Cu segregation occurs in the samples in as-cast and heat treated samples that forms the FCC phases. The increasing FCC amount after the annealing process causes the softening in the LWHEAs and makes them more ductile. Thus, $Cu_{29}Ni_{29}Al_{14}Ti_{14}Cr_{14}$ LWHEA shows the most promising mechanical properties with 855 MPa yield strength, 1485 MPa fracture strength, and 22.6 % ductility after annealing at 925 °C for 2 h. The yield, fracture strength and ductility of this LWHEA changes to 902 MPa, 1332 MPa and 12.71 %, respectively, when it is produced from industrial grade raw materials by induction casting.

CHAPTER 7

CONCLUSION

In this study, firstly, various combinations including Al, Ti, V, Cr, Mn, B, Si, Cu, Ni, and Cr elements are designed with four or five elements. The primary aim is to have a lightweight high entropy alloy (LWHEA) with low density, high strength and ductility as compared to density (~7.86 gr/cm^3) and mechanical properties steel parts used in the industry. Thermophysical calculations, Vienna Ab initio Simulation Package (VASP) and Thermo-Calc software with HEA database are used to design LWHEAs. The LWHEAs are produced by copper-hearth arc-melter and suction casting in cylindrical shapes with 3 or 4 mm diameters. The structural investigation electron microscopy (SEM, TEM) and X-ray diffraction (XRD) techniques. Thermal analysis (TGA) are performed to reveal phase transformation and melting behavior of the LWHEAs. Mechanical tests (compression and hardness) are conducted on the LWHEAs. The most promising LWHEA in terms of density, structure, and mechanical properties is produced in-scale up by induction casting.

In the first part of the thesis, novel AlTiVCrMnB$_X$ (x=0, 0.3, 0.6, 1.0), AlTiVCrSi, AlTiVCrMnSi, AlTiVCrMn, $Al_{35}Ti_{35}V_{20}Cr_5Mn_5$, $Al_5Ti_5V_{20}Cr_{35}Mn_{35}$ LWHEAs are designed and produced. The structural characterization analysis results showed that the addition of B element destroys the crystal and promotes the formation of intermetallic compounds (ICs) that makes the LWHEA quite hard and brittle. When B element was replaced by Si, larger negative enthalpy of mixing (ΔH_{mix}) values were seen in the new set of the LWHEAs. The larger negative ΔH_{mix} values caused the formation of ICs with increasing peak intensities in XRD patterns. Therefore, the most promising LWHEA in this group is $Al_{35}Ti_{35}V_{20}Cr_5Mn_5$ LWHEA in terms of density (4.34 g/cm^3), structure. However, the formation of ordered BCC phase (B2) made the alloy very brittle.

In the second part, we have designed novel MEAs ($Cu_{20}Ni_{20}A_{l30}Ti_{30}$, $Cu_{25}Ni_{25}Al_{25}Ti_{25}$, $Cu_{34}Ni_{22}Al_{22}Ti_{22,}$ and $Cu_{35}Ni_{25}Al_{20}Ti_{20}$) using thermophysical calculations. These MEAs were then produced using copper heart arc melting and suction cast into cylindrical rods with 3 mm diameters. The corresponding results reveal that the $Cu_{20}Ni_{20}A_{l30}Ti_{30}$, MEA consists of a BCC phase with some amount of ICs whereas $Cu_{25}Ni_{25}Al_{25}Ti_{25}$ has single BCC phase. When the amounts Cu and Ni are increased in the $Cu_{34}Ni_{22}Al_{22}Ti_{22}$ and $Cu_{35}Ni_{25}Al_{20}Ti_{20}$ MEAs, the system drives itself towards a FCC structure. The mechanical results show that the most promising MEA among the others is $Cu_{35}Ni_{25}Al_{20}Ti_{20}$ rods having 13 % compressive strain with 820 and 1338 MPa yield and compressive strengths, respectively.

Alternatively, LWHEAs with relatively low density (6.20-6.76 g/cm^3) were designed using Cu, Ni, Al, Ti, Cr, and V elements. Although Ni and Cu elements have higher densities, these are used due to their higher VEC values to produce samples with BCC and FCC crystal structures. Therefore, $Cu_{25}Ni_{25}Al_{18}Ti_{16}V_{16}$, $Cu_{29}Ni_{29}Al_{14}Ti_{14}V_{14}$, $Cu_{25}Ni_{25}Al_{18}Ti_{16}Cr_{16}$, and $Cu_{29}Ni_{29}Al_{14}Ti_{14}Cr_{14}$ LWHEAs were designed and cast to cylindrical 3 mm water-cooled copper mold. The effect of V and Cr elements was investigated in details in terms of structure and mechanical properties. Experimental results showed that hard ordered BCC (B2) was present together with the soft FCC phase in all the LWHEA sets consist of V and Cr elements. However, Cr containing $Cu_{25}Ni_{25}Al_{18}Ti_{16}Cr_{16}$, and $Cu_{29}Ni_{29}Al_{14}Ti_{14}Cr_{14}$ LWHEAs showed better mechanical properties as compared to V containing LWHEAs. Higher amount of FCC phases in $Cu_{29}Ni_{29}Al_{14}Ti_{14}Cr_{14}$ LWHEA caused higher ductility in-as-cast condition and it was further increased to 22.6 % upon annealing at 900 °C for 2 h. with 855 MPa yield strength, 1485 MPa fracture strength.

CHAPTER 8

FUTURE RECOMMENDATIONS

8.1. High Entropy Bulk Metallic Glasses (HE-BMGs)

Bulk metallic glasses (BMGs) have received significant attention due to their unique properties such as high strength, high hardness, wear resistance, high corrosion, and excellent soft magnetic properties compared with their crystalline counterparts since it was first discovered in 1960 [115]–[119]. A significant number of glass-forming alloys have been reported up to date based on empirical calculations [120]. Most of these alloys are based on or two constituent elements. The rest of the elements in the periodic table are used for the alloying to have a composition near deep eutectics in binary and ternary systems [121]. However, very few thermodynamic data are available to construct deep eutectic compositions of metallic glasses (MGs) in quaternary and higher-order systems [122].

High-entropy bulk metallic glasses (HE-BMGs) are a novel class of materials that include the bulk form of MGs, namely BMGs with the compositional features of HEAs [120], [123]. It can be seen that both HEAs and BMGs have a common characteristic complexity with their compositions involving more elements. Therefore, The HE-BMGs can be defined as a mathematical intersection of BMGs and HEAs [124], [125]. In general, HEAs consist of five or more principal elements with equiatomic or near equiatomic composition that causes single or dual solid solutions phases such as FCC, BCC or HCP structures [49], [110]. On the other hand, BMGs are composed of two or more constituent elements with a nonstoichiometric composition that form monocrystalline structures. These alloys show glass transition with increasing temperatures [116], [119], [120].

Bizhanova et al. [126] developed novel near-equiatomic $Zr_{31}Ti_{27}Be_{26}Cu_{10}M_6$ (M=Ag, Al, Ni, V, Cr, Fe) and $Zr_{28}Ti_{24}Be_{23}Cu_9Ni_{10}N_6$ (N=V, Cr, Fe, Ag, Al) HE-BMGs by applying empirical calculations rules of HEAs. They investigated the relationship between δ and ΔH_{mix} to reveal the critical HE-BMGs formation regions. It was pointed out that the HE-BMGs have larger δ and ΔH_{mix} values in their amorphous state as shown in Figure 8.1. They also investigated the crystallization kinetics of near equiatomic HE-BMGs that the samples showed characteristics of both equiatomic HE-BMGs and conventional BMGs.

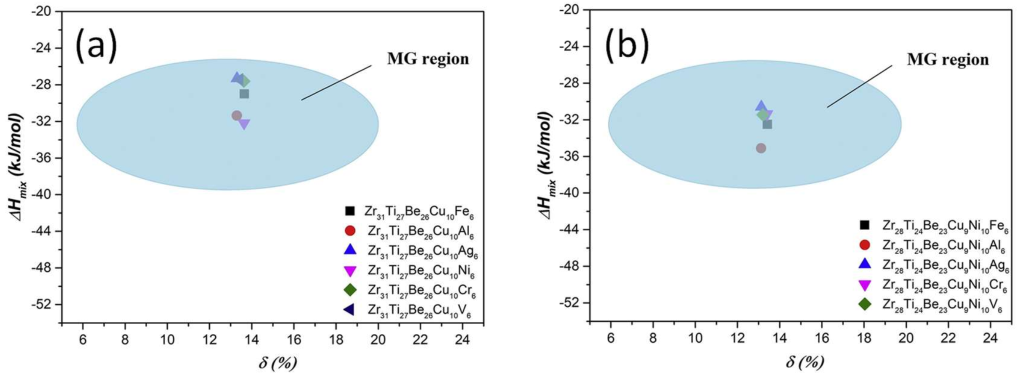

Figure 8.1. δ and ΔH_{mix} regions of a) $Zr_{31}Ti_{27}Be_{26}Cu_{10}M_6$ (M=Ag, Al, Ni, V, Cr, Fe), b) $Zr_{28}Ti_{24}Be_{23}Cu_9Ni_{10}N_6$ (N=V, Cr, Fe, Ag, Al) HE-BMGs [126]

8.2. Our Preliminary Experiments on HE-BMGs

We have designed Zr-Cu-Al based $(Zr_{50}Cu_{40}Al_{10})_{100-x}Sm_x$ (x=0, 2, 4 at. % Sm) MGs produced by arc melting and subsequently melt-spun into 40 μm thick ribbons. The crystallization kinetics of the MGs are investigated using differential scanning calorimetry and XRD analysis under isothermal and non-isothermal conditions. The primer crystallization phase of $Zr_{50}Cu_{40}Al_{10}$ MG (without Sm addition) is found to be $Cu_{10}Zr_7$ under both isothermal and isochronal annealing condition. However, isothermal annealing of $Zr_{49}Cu_{39.2}Al_{9.8}Sm_2$ and $Zr_{48}Cu_{38.4}Al_{9.6}Sm_4$ MGs primarily yields Cu_2Sm crystallization, while Cu_2Sm and $Cu_{10}Zr_7$ phases form under isochronal annealing as seen in Figure 8.2 [127].

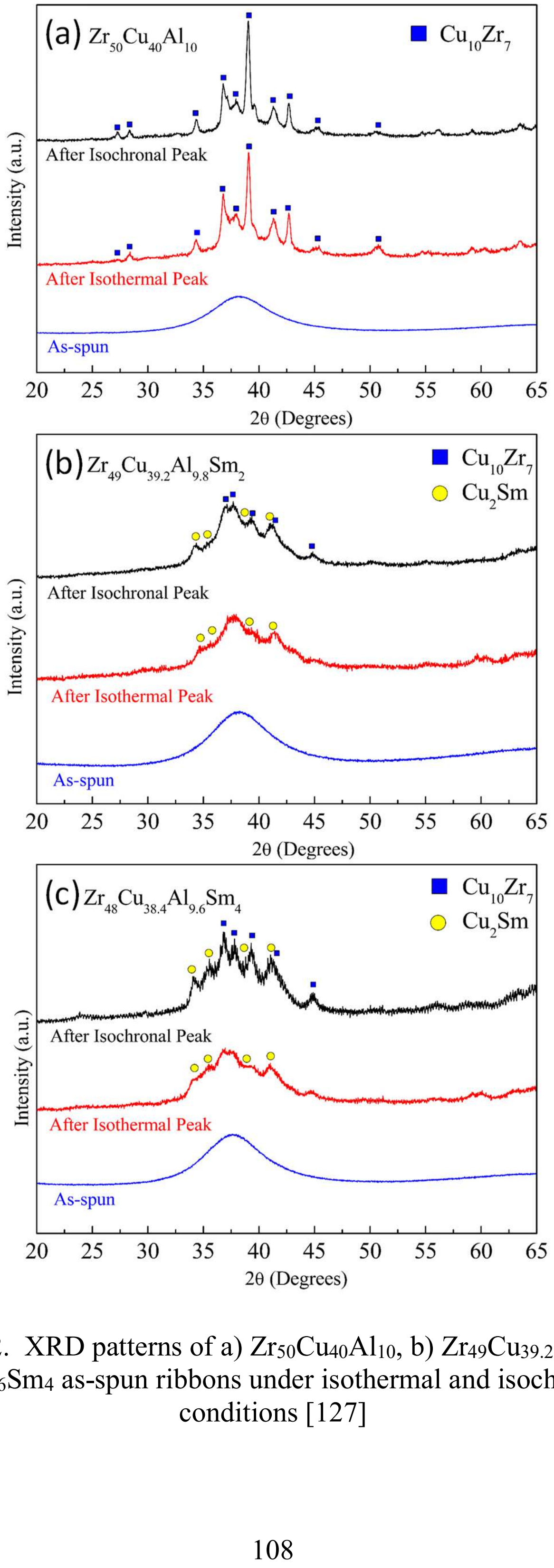

Figure 8.2. XRD patterns of a) Zr$_{50}$Cu$_{40}$Al$_{10}$, b) Zr$_{49}$Cu$_{39.2}$Al$_{9.8}$Sm$_2$, c) Zr$_{48}$Cu$_{38.4}$Al$_{9.6}$Sm$_4$ as-spun ribbons under isothermal and isochronal annealing conditions [127]

Also, kinetics analysis is done on the $Zr_{50}Cu_{40}Al_{10}$, $Zr_{49}Cu_{39.2}Al_{9.8}Sm_2$, and $Zr_{48}Cu_{38.4}Al_{9.6}Sm_4$ MGs and crystallization activation energies are calculated by Kissinger and Ozawa methods. As seen in Table 8.1, Sm addition increases the activation energy required for the crystallization of $Cu_{10}Zr_7$ phase [127].

Table 8.1. Crystallization activation energies of $Cu_{10}Zr_7$ for $Zr_{50}Cu_{40}Al_{10}$, $Zr_{49}Cu_{39.2}Al_{9.8}Sm_2$, and $Zr_{48}Cu_{38.4}Al_{9.6}Sm_4$ as-spun MGs ribbons calculated with Kissinger and Ozawa methods [127]

Composition	**$E_{Kissinger}$ (kJ/mol)**	**E_{Ozawa} (kJ/mol)**
$Zr_{50}Cu_{40}Al_{10}$	347±13	342±13
$Zr_{49}Cu_{39.2}Al_{9.8}Sm_2$	396±11	388±11
$Zr_{48}Cu_{38.4}Al_{9.6}Sm_4$	390±6	382±6

Johnson-Mehl-Avrami (JMA) model is applied to the MGs to reveal their isothermal crystallization kinetics. The calculations are done for the first crystallized phases in the alloys that $Zr_{50}Cu_{40}Al_{10}$ represents the crystallization of $Cu_{10}Zr_7$, while $Zr_{49}Cu_{39.2}Al_{9.8}Sm_2$ and $Zr_{48}Cu_{38.4}Al_{9.6}Sm_4$ compositions mainly represent the crystallization of Cu_2Sm phase. The calculated local energies of the MGs are 387 kJ/mol, 438 kJ/mol, and 457 kJ/mol for $Zr_{50}Cu_{40}Al_{10}$, $Zr_{49}Cu_{39.2}Al_{9.8}Sm_2$, and $Zr_{48}Cu_{38.4}Al_{9.6}Sm_4$. The increase in the local activation energies under isothermal conditions can be attributed to the crystallization of Cu_2Sm that depleting Sm atoms within the amorphous matrix. Therefore, decreasing amount of Sm in the amorphous matrix can make it more stable that causing the crystallization process to be more difficult [127].

Recently, many related works about HE-BGMs consist of Cu, Zr, Al elements with remaining alloying elements such as Ti, Ni, Hf, Co are reported by experimental and simulation techniques [122], [128]–[131]. For instance, Pi et al. [128] and Fang et al.

[129] investigated the mechanical behavior of $Cu_{29}Zr_{32}Ti_{15}Al_{5}Ni_{19}$ HE-BMG produced by suction casting into a water-cooled copper mold. They pointed out that, the alloy has good plasticity and also hardness and Young's modulus values higher than 7.45 GPa, and 93.1 GPa, respectively.

A preliminary experiment is done on HE-BMGs based on our previous MG study [127] and the studies in the literature [122], [125], [129]–[134]. We have produced equiatomic CuZrAlTi HE-BMG by arc melting and suctions casting. XRD analysis is done on the samples in as-melt state and suction cast rods with 3 mm diameter. XRD analysis results are shown in Figure 8.3. The sample has BCC, $(Al_{0.5}Cu_{0.5})_2Zr$, $Cu_{10}Zr_7$, and $Cu_{51}Zr_{14}$ multiphase in the as-cast condition. However, when the alloy is cast into 3 mm water-cooled copper mold by suction casting, a dominant $(Al_{0.5}Cu_{0.5})_2Zr$ phases are seen in the XRD pattern. On the other hand, the relative intensities of the remaining phases are decreased after suction casting. Therefore, it can be interpreted that rapid solidification techniques can improve the alloys towards decreasing the number of phases in the alloys. Also, unmatched peaks are seen in the XRD pattern of the CuZrAlTi HE-BMG.

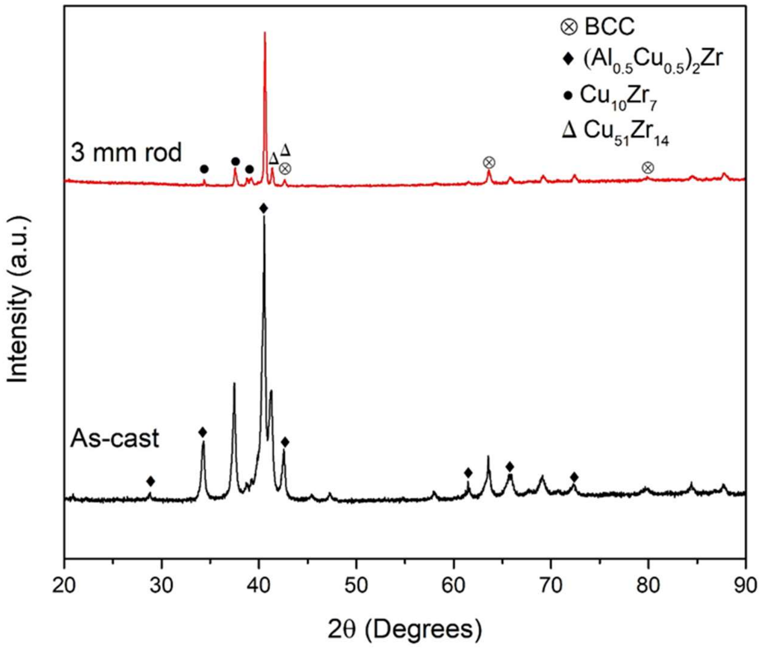

Figure 8.3. XRD results of as-cast and suction cast 3 mm CuZrAlTi HE-BMG

The crystal structure determination done on these peaks reveal that these peaks corresponds to BCC crystal structure with an almost constant lattice parameter (2.938 Å). This phase may be referred to a HEA phase in the CuZrAlTi alloy. Thus, it may be possible to produce HEAs from Cu-Zr-Al-Ti elements with additional multiphase such as crystal and amorphous phases based on the cooling rates. These alloys will be verified in terms of composition and cooling conditions (suction casting, melt spinning, and magnetron sputtering) to tune the phases of the alloys.

8.3. Additive Manufacturing Technique

Most of the studies done on HEAs are based on casting techniques such as are melting and induction casting. The microstructure of the HEAs produced by these methods is commonly required to improve by post-processing methods, such as cold rolling, forging, or annealing treatment [49], [102]. In some cases, further processing is required to remove the casting defects (i.e. shrinkages and pores) in as-cast materials [135]. However, additive manufacturing (AM), also known as three-dimensional (3D) printing, the technique is a flexible method to produce HEAs with complex shapes as compared to conventional methods. This technique has received dramatic attention in scientific and industrial studies to produce materials without any additional post-processing methods [135]. Currently, many engineering alloys such as Al [136], Ti [137], Fe [138] are produced by AM technique. This technique increases the production efficiency, decrease the cost, and enable to design and produce materials with net-shape manufacturing [139]. Recently, the studies focused on production HEAs by AM technique and many HEAs are produced successfully [140], [141]. Brif et al. [142] produced an equiatomic FeCoCrNi HEA by selective laser melting (SLM) as a production route of AM. They used pre-alloyed, gas-atomized FeCoCrNi powders for the production and the same HEA is also produced by arc-melter. The comparison of the mechanical properties shows that the mechanical properties of the AM HEAs were significantly enhanced as compared to the as-cast samples due to their fine microstructure achieved by SLM method. A uniform chemical distribution without segregations was seen in the EDS mapping of the FeCoCrNi HEA as shown in Figure 8.4. Upon annealing at 1000 °C, the HEA shows 433 MPa yield and 682 MPa tensile strength, and 42 % ductility.

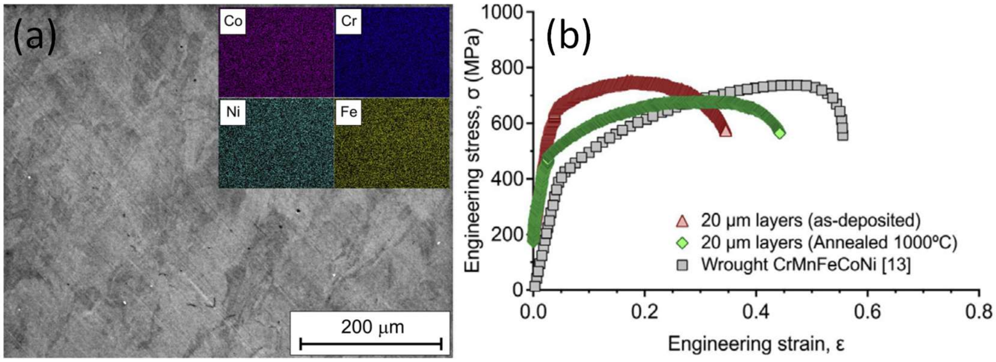

Figure 8.4. a) SE image of as-deposited 20 μm FeCoCrNi HEA with EDS inset showing elemental distribution, b) Representative tensile curves of the HEA [142]

As summarized above, AM will be a major production technique due to its cost and time effective and also net-shape manufacturing capability without any additional post-processing procedure. Therefore, the LWHEAs produced by arc-melter and induction casting techniques can be also produced by AM method. The comparison of the methods can be done in terms of structure and mechanical properties.

REFERENCES

[1] B. S. Murty, J. W. Yeh, S. Ranganathan, and P. P. Bhattacharjee, “High-entropy alloys: basic concepts,” High-Entropy Alloys, pp. 13–30, 2019.

[2] M.-H. Tsai and J.-W. Yeh, “High-Entropy Alloys: A Critical Review,” Materials Research Letters, vol. 2, no. 3, pp. 107–123, 2014.

[3] C. Hsu, J. Yeh, S. Chen, and T. Shun, “Wear resistance and high-temperature compression strength of Fcc CuCoNiCrAl0.5Fe alloy with boron addition,” Metallurgical and Materials Transactions A, vol. 35, no. 5, pp. 1465–1469, 2004.

[4] J. W. Yeh, “Recent progress in high-entropy alloys,” Annales de Chimie: Science des Materiaux, vol. 31, no. 6, pp. 633–648, 2006.

[5] Y. Zhang et al., “Microstructures and properties of high-entropy alloys,” Progress in Materials Science, vol. 61, no. November 2013, pp. 1–93, 2014.

[6] K.-H. Huang and J. W. Yeh, “A study on the multicomponent alloy systems containing equal-mole elements,” National Tsing Hua University, 1996.

[7] J. W. Yeh et al., “Nanostructured high-entropy alloys with multiple principal elements: Novel alloy design concepts and outcomes,” Advanced Engineering Materials, vol. 6, no. 5, pp. 299-303+274, 2004.

[8] Y. Zhang, S. G. Ma, and J. W. Qiao, “Morphology transition from dendrites to equiaxed grains for AlCoCrFeNi high-entropy alloys by copper mold casting and bridgman solidification,” Metallurgical and Materials Transactions A: Physical Metallurgy and Materials Science, vol. 43, no. 8, pp. 2625–2630, 2012.

[9] S. Guo, Q. Hu, C. Ng, and C. T. Liu, “More than entropy in high-entropy alloys: Forming solid solutions or amorphous phase,” Intermetallics, vol. 41, pp. 96–103, 2013.

[10] K. M. Youssef, A. J. Zaddach, C. Niu, D. L. Irving, and C. C. Koch, “A Novel Low-Density, High-Hardness, High-entropy Alloy with Close-packed Single-phase Nanocrystalline Structures,” Materials Research Letters, vol. 3, no. 2, pp. 95–99, 2015.

[11] O. N. Senkov, S. V. Senkova, and C. Woodward, “Effect of aluminum on the microstructure and properties of two refractory high-entropy alloys,” Acta Materialia, vol. 68, pp. 214–228, 2014.

[12] J. W. Yeh, “Alloy design strategies and future trends in high-entropy alloys,” Jom, vol. 65, no. 12, pp. 1759–1771, 2013.

[13] B. S. Murty, J. W. Yeh, S. Ranganathan, B. S. Murty, J. W. Yeh, and S. Ranganathan, "Chapter 2 – High-Entropy Alloys: Basic Concepts," in High Entropy Alloys, 2014, pp. 13–35.

[14] A. Takeuchi, K. Amiya, T. Wada, K. Yubuta, W. Zhang, and A. Makino, "Entropies in alloy design for high-entropy and bulk glassy alloys," Entropy, vol. 15, no. 9, pp. 3810–3821, 2013.

[15] D. B. Miracle and O. N. Senkov, "A critical review of high entropy alloys and related concepts," Acta Materialia, vol. 122, pp. 448–511, 2017.

[16] Y. Zhang, Y. J. Zhou, J. P. Lin, G. L. Chen, and P. K. Liaw, "Solid-solution phase formation rules for multi-component alloys," Advanced Engineering Materials, vol. 10, no. 6, pp. 534–538, 2008.

[17] S. Guo, C. Ng, J. Lu, and C. T. Liu, "Effect of valence electron concentration on stability of fcc or bcc phase in high entropy alloys," Journal of Applied Physics, vol. 109, no. 10, 2011.

[18] E. J. Pickering and N. G. Jones, "High-entropy alloys: a critical assessment of their founding principles and future prospects," International Materials Reviews, vol. 61, no. 3, pp. 183–202, 2016.

[19] J.-W. Yeh et al., "Formation of simple crystal structures in Cu-Co-Ni-Cr-Al-Fe-Ti-V alloys with multiprincipal metallic elements," Metallurgical and Materials Transactions A, vol. 35, no. 8, pp. 2533–2536, 2004.

[20] J. W. Yeh, S. Y. Chang, Y. Der Hong, S. K. Chen, and S. J. Lin, "Anomalous decrease in X-ray diffraction intensities of Cu-Ni-Al-Co-Cr-Fe-Si alloy systems with multi-principal elements," Materials Chemistry and Physics, vol. 103, no. 1, pp. 41–46, 2007.

[21] A. J. Zaddach, C. Niu, C. C. Koch, and D. L. Irving, "Mechanical properties and stacking fault energies of NiFeCrCoMn high-entropy alloy," Jom, vol. 65, no. 12, pp. 1780–1789, 2013.

[22] M. Beyramali Kivy, M. Asle Zaeem, and S. Lekakh, "Investigating phase formations in cast AlFeCoNiCu high entropy alloys by combination of computational modeling and experiments," Materials and Design, vol. 127, no. February, pp. 224–232, 2017.

[23] M. C. Gao, P. Gao, J. A. Hawk, L. Ouyang, D. E. Alman, and M. Widom, "Computational modeling of high-entropy alloys: Structures, thermodynamics and elasticity," Journal of Materials Research, vol. 32, no. 19, pp. 3627–3641, 2017.

[24] H. Mao, H. L. Chen, and Q. Chen, "TCHEA1: A Thermodynamic Database Not Limited for 'High Entropy' Alloys," Journal of Phase Equilibria and Diffusion, vol. 38, no. 4, pp. 353–368, 2017.

[25] H. L. Chen, H. Mao, and Q. Chen, “Database development and Calphad calculations for high entropy alloys: Challenges, strategies, and tips,” Materials Chemistry and Physics, pp. 1–12, 2017.

[26] X. Yang, Y. Zhang, and P. K. Liaw, “Microstructure and Compressive Properties of NbTiVTaAlx High Entropy Alloys,” Procedia Engineering, vol. 36, pp. 292–298, 2012.

[27] C. Zhang and M. C. Gao, “CALPHAD modeling of high-entropy alloys,” in High-Entropy Alloys: Fundamentals and Applications, 2016.

[28] B. S. Murty, J. W. Yeh, S. Ranganathan, B. S. Murty, J. W. Yeh, and S. Ranganathan, “Chapter 5 – Synthesis and Processing,” in High Entropy Alloys, 2014, pp. 77–89.

[29] S. Singh, N. Wanderka, B. S. Murty, U. Glatzel, and J. Banhart, “Decomposition in multi-component AlCoCrCuFeNi high-entropy alloy,” Acta Materialia, vol. 59, no. 1, pp. 182–190, 2011.

[30] V. F. Bashev and O. I. Kushnerov, “Structure and properties of cast and splat-quenched high-entropy Al–Cu–Fe–Ni–Si alloys,” Physics of Metals and Metallography, vol. 118, no. 1, pp. 39–47, 2017.

[31] B. S. Murty, High-entropy alloys. Butterworth-Heinemann, 2014.

[32] C. Wang, W. Ji, and Z. Fu, “Mechanical alloying and spark plasma sintering of CoCrFeNiMnAl high-entropy alloy,” Advanced Powder Technology, vol. 25, no. 4, pp. 1334–1338, 2014.

[33] L. Gao, W. Liao, H. Zhang, J. Surjadi, D. Sun, and Y. Lu, “Microstructure, Mechanical and Corrosion Behaviors of CoCrFeNiAl0.3 High Entropy Alloy (HEA) Films,” Coatings, vol. 7, no. 10, p. 156, 2017.

[34] Q. Ding et al., “Tuning element distribution, structure and properties by composition in high-entropy alloys,” Nature, vol. 574, no. 7777, pp. 223–227, 2019.

[35] Z. Li, S. Zhao, R. O. Ritchie, and M. A. Meyers, “Mechanical properties of high-entropy alloys with emphasis on face-centered cubic alloys,” Progress in Materials Science, vol. 102, no. March 2018, pp. 296–345, 2019.

[36] H. P. Chou, Y. S. Chang, S. K. Chen, and J. W. Yeh, “Microstructure, thermophysical and electrical properties in AlxCoCrFeNi (0 ??? x ???2) high-entropy alloys,” Materials Science and Engineering B: Solid-State Materials for Advanced Technology, vol. 163, no. 3, pp. 184–189, 2009.

[37] R. Feng et al., “Design of light-weight high-entropy alloys,” Entropy, vol. 18, no. 9, pp. 16–29, 2016.

[38] M. Drahansky et al., “We are IntechOpen , the world ’ s leading publisher of

Open Access books Built by scientists , for scientists TOP 1 %," Intech, vol. i, no. tourism, p. 13, 2016.

[39] V. H. Hammond, M. A. Atwater, K. A. Darling, H. Q. Nguyen, and L. J. Kecskes, "Equal-Channel Angular Extrusion of a Low-Density High-Entropy Alloy Produced by High-Energy Cryogenic Mechanical Alloying," Jom, vol. 66, no. 10, pp. 2021–2029, 2014.

[40] X. Yang, S. Y. Chen, J. D. Cotton, and Y. Zhang, "Phase Stability of Low-Density, Multiprincipal Component Alloys Containing Aluminum, Magnesium, and Lithium," Jom, vol. 66, no. 10, pp. 2009–2020, 2014.

[41] R. Li, J. C. Gao, and K. Fan, "Microstructure and mechanical properties of MgMnAlZnCu high entropy alloy cooling in three conditions," Materials Science Forum, vol. 686, pp. 235–241, 2011.

[42] K. K. Tseng, Y. C. Yang, C. C. Juan, T. S. Chin, C. W. Tsai, and J. W. Yeh, "A light-weight high-entropy alloy Al20Be20Fe10Si15Ti35," Science China Technological Sciences, vol. 61, no. 2, pp. 184–188, 2018.

[43] K. M. Youssef, A. J. Zaddach, C. Niu, D. L. Irving, and C. C. Koch, "A novel low-density, high-hardness, high-entropy alloy with close-packed single-phase nanocrystalline structures," Materials Research Letters, vol. 3, no. 2, pp. 95–99, 2014.

[44] A. Kumar and M. Gupta, "An insight into evolution of light weight high entropy alloys: A review," Metals, vol. 6, no. 9, 2016.

[45] N. D. Stepanov, N. Yu Yurchenko, D. G. Shaysultanov, G. A. Salishchev, and M. A. Tikhonovsky, "Effect of Al on structure and mechanical properties of AlxNbTiVZr (x = 0, 0.5, 1, 1.5) high entropy alloys," Materials Science and Technology (United Kingdom), vol. 31, no. 10, pp. 1184–1193, 2015.

[46] N. D. Stepanov, D. G. Shaysultanov, G. A. Salishchev, and M. A. Tikhonovsky, "Structure and mechanical properties of a light-weight AlNbTiV high entropy alloy," Materials Letters, vol. 142, pp. 153–155, 2015.

[47] R. Li, J. Gao, and K. Fa, "Study to microstructure and mechanical properties of Mg containing high entropy alloys," Materials Science Forum, vol. 650, pp. 265–271, 2010.

[48] S. Gorsse, D. B. Miracle, and O. N. Senkov, "Mapping the world of complex concentrated alloys," Acta Materialia, vol. 135, pp. 177–187, 2017.

[49] D. B. Miracle and O. N. Senkov, "A critical review of high entropy alloys and related concepts," Acta Materialia, vol. 122, pp. 448–511, 2017.

[50] Y. Jia, Y. Jia, S. Wu, X. Ma, and G. Wang, "Novel ultralight-weight complex concentrated alloys with high strength," Materials, vol. 12, no. 7, 2019.

[51] Y. Qiu et al., “A lightweight single-phase AlTiVCr compositionally complex alloy,” Acta Materialia, vol. 123, pp. 115–124, 2017.

[52] N. Y. Yurchenko, N. D. Stepanov, S. V. Zherebtsov, M. A. Tikhonovsky, and G. A. Salishchev, “Structure and mechanical properties of B2 ordered refractory AlNbTiVZrx (x = 0–1.5) high-entropy alloys,” Materials Science and Engineering A, vol. 704, no. June, pp. 82–90, 2017.

[53] Y. Ma et al., “The BCC/B2 morphologies in Al x NiCoFeCr high-entropy alloys,” Metals, vol. 7, no. 2, pp. 1–12, 2017.

[54] X. Yang and Y. Zhang, “Prediction of high-entropy stabilized solid-solution in multi-component alloys,” Materials Chemistry and Physics, vol. 132, no. 2–3, pp. 233–238, 2012.

[55] Y. Zhang, X. Yang, and P. K. Liaw, “Alloy design and properties optimization of high-entropy alloys,” Jom, vol. 64, no. 7, pp. 830–838, 2012.

[56] M. Kang, K. R. Lim, J. W. Won, and Y. S. Na, “Effect of Co content on the mechanical properties of A2 and B2 phases in AlCoxCrFeNi high-entropy alloys,” Journal of Alloys and Compounds, vol. 769, pp. 808–812, 2018.

[57] Ł. Rogal et al., “Microstructure and Mechanical Properties of Al–Co–Cr–Fe–Ni Base High Entropy Alloys Obtained Using Powder Metallurgy,” Metals and Materials International, vol. 25, no. 4, pp. 930–945, 2019.

[58] Y. Zhang et al., “Microstructures and properties of high-entropy alloys,” Progress in Materials Science, vol. 61, no. October 2013, pp. 1–93, 2014.

[59] Q. Wei, S. Cheng, K. T. Ramesh, and E. Ma, “Effect of nanocrystalline and ultrafine grain sizes on the strain rate sensitivity and activation volume: Fcc versus bcc metals,” Materials Science and Engineering A, vol. 381, no. 1–2, pp. 71–79, 2004.

[60] S. Guo, “Phase selection rules for cast high entropy alloys: an overview,” Materials Science and Technology, vol. 31, no. 10, pp. 1223–1230, 2015.

[61] A. Argast and C. F. Tennis, “A web resource for the study of alkali feldspars and perthitic textures using light microscopy, scanning electron microscopy and energy dispersive x-ray spectroscopy,” Journal of Geoscience Education, vol. 52, no. 3, pp. 213–217, 2004.

[62] S. Guo and C. T. Liu, “Phase stability in high entropy alloys: Formation of solid-solution phase or amorphous phase,” Progress in Natural Science: Materials International, vol. 21, no. 6, pp. 433–446, 2011.

[63] G. Dale E., Newbury David C. Joy Patrick, Echlin Charles E., Fiori Joseph I., Advanced Scanning Electron Microscopy and X-Ray Microanalysis, Third Edit. Springer US, 2003.

[64] F. Reactor, M. Program, and O. Ridge, “Oak Ridge National Laboratory, 2 University of Tennessee),” vol. 54, pp. 154–161, 2013.

[65] S. Daniel, “X-RAY DIFFRACTION (XRD),” 2013.

[66] V. Soni, O. N. Senkov, B. Gwalani, D. B. Miracle, and R. Banerjee, “Microstructural Design for Improving Ductility of An Initially Brittle Refractory High Entropy Alloy,” Scientific Reports, vol. 8, no. 1, pp. 1–10, 2018.

[67] E. Ghassemali, R. Sonkusare, K. Biswas, and N. P. Gurao, “In-situ study of crack initiation and propagation in a dual phase AlCoCrFeNi high entropy alloy,” Journal of Alloys and Compounds, vol. 710, pp. 539–546, 2017.

[68] U. Roy, H. Roy, H. Daoud, U. Glatzel, and K. K. Ray, “Fracture toughness and fracture micromechanism in a cast AlCoCrCuFeNi high entropy alloy system,” Materials Letters, vol. 132, pp. 186–189, 2014.

[69] Y. Yu, J. Wang, J. Li, H. Kou, and W. Liu, “Characterization of BCC phases in AlCoCrFeNiTix high entropy alloys,” Materials Letters, vol. 138, pp. 78–80, 2015.

[70] H. Huang, J. Ding, and P. G. McCormick, “Micro structural evolution of 304 stainless steel during mechanical milling,” Materials Science and Engineering A, vol. 216, no. 1–2, pp. 178–184, 1996.

[71] T. T. Shun, L. Y. Chang, and M. H. Shiu, “Microstructure and mechanical properties of multiprincipal component CoCrFeNiMo x alloys,” Materials Characterization, vol. 70, pp. 63–67, 2012.

[72] M. S. Lucas et al., “Magnetic and vibrational properties of high-entropy alloys,” Journal of Applied Physics, vol. 109, no. 7, pp. 107–110, 2011.

[73] L. Zhang, Y. Zhou, X. Jin, X. Du, and B. Li, “The microstructure and high-temperature properties of novel nano precipitation-hardened face centered cubic high-entropy superalloys,” Scripta Materialia, vol. 146, pp. 226–230, 2018.

[74] S. Wei, F. He, and C. C. Tasan, “Metastability in high-entropy alloys: A review,” Journal of Materials Research, vol. 33, no. 19, pp. 2924–2937, 2018.

[75] M. Ogura, T. Fukushima, R. Zeller, and P. H. Dederichs, “Structure of the high-entropy alloy AlxCrFeCoNi: Fcc versus bcc,” Journal of Alloys and Compounds, vol. 715, pp. 454–459, 2017.

[76] F. Xu et al., “The BCC/B2 Morphologies in AlxNiCoFeCr High-Entropy Alloys,” Metals, vol. 7, no. 2, p. 57, 2017.

[77] S. Gangireddy, B. Gwalani, V. Soni, R. Banerjee, and R. S. Mishra, “Contrasting mechanical behavior in precipitation hardenable Al X CoCrFeNi

high entropy alloy microstructures: Single phase FCC vs. dual phase FCC-BCC," Materials Science and Engineering A, vol. 739, no. August 2018, pp. 158–166, 2019.

[78] Z. Li, K. G. Pradeep, Y. Deng, D. Raabe, and C. C. Tasan, "Metastable high-entropy dual-phase alloys overcome the strength-ductility trade-off," Nature, vol. 534, no. 7606, pp. 227–230, 2016.

[79] S. Guo, C. Ng, and C. T. Liu, "Anomalous solidification microstructures in Co-free Al xCrCuFeNi2 high-entropy alloys," Journal of Alloys and Compounds, vol. 557, pp. 77–81, 2013.

[80] J. M. Park et al., "Role of BCC phase on tensile behavior of dual-phase Al 0.5 CoCrFeMnNi high-entropy alloy at cryogenic temperature," Materials Science and Engineering A, vol. 746, no. January, pp. 443–447, 2019.

[81] K. R. Lim, K. S. Lee, J. S. Lee, J. Y. Kim, H. J. Chang, and Y. S. Na, "Dual-phase high-entropy alloys for high-temperature structural applications," Journal of Alloys and Compounds, vol. 728, pp. 1235–1238, 2017.

[82] R. Chen et al., "Composition design of high entropy alloys using the valence electron concentration to balance strength and ductility," Acta Materialia, vol. 144, pp. 129–137, 2018.

[83] Y. Zhou, D. Zhou, X. Jin, L. Zhang, X. Du, and B. Li, "Design of non-equiatomic medium-entropy alloys," Scientific Reports, vol. 8, no. 1, p. 1236, Dec. 2018.

[84] A. Gali and E. P. George, "Tensile properties of high- and medium-entropy alloys," Intermetallics, vol. 39, pp. 74–78, 2013.

[85] G. Laplanche, A. Kostka, C. Reinhart, J. Hunfeld, G. Eggeler, and E. P. George, "Reasons for the superior mechanical properties of medium-entropy CrCoNi compared to high-entropy CrMnFeCoNi," Acta Materialia, vol. 128, pp. 292–303, 2017.

[86] S. A. Kube, S. Sohn, D. Uhl, A. Datye, A. Mehta, and J. Schroers, "Phase selection motifs in High Entropy Alloys revealed through combinatorial methods: Large atomic size difference favors BCC over FCC," Acta Materialia, vol. 166, pp. 677–686, 2019.

[87] A. T. and A. Inoue, "Classification of Bulk Metallic Glasses by Atomic Size Difference, Heat of Mixing and Period of Constituent Elements and Its Application to Characterization of the Main Alloying Element," Materials Transactions, vol. 46, no. 12, pp. 2817–2829, 2005.

[88] W. Li, P. K. Liaw, and Y. Gao, "Fracture resistance of high entropy alloys: A review," Intermetallics, vol. 99, no. May, pp. 69–83, 2018.

[89] S. Luo, Z. You, and L. Lu, "Thickness effect on fracture behavior of columnar-grained Cu with preferentially oriented nanoscale twins," Journal of Materials Research, vol. 32, no. 24, pp. 4554–4562, 2017.

[90] Z. Li and D. Raabe, "Influence of compositional inhomogeneity on mechanical behavior of an interstitial dual-phase high-entropy alloy," Materials Chemistry and Physics, vol. 210, pp. 29–36, 2018.

[91] S. P. Wang and J. Xu, "(TiZrNbTa)-Mo high-entropy alloys: Dependence of microstructure and mechanical properties on Mo concentration and modeling of solid solution strengthening," Intermetallics, vol. 95, no. October 2017, pp. 59–72, 2018.

[92] A. Shabani, M. R. Toroghinejad, A. Shafyei, and R. E. Logé, "Evaluation of the mechanical properties of the heat treated FeCrCuMnNi high entropy alloy," Materials Chemistry and Physics, vol. 221, no. November 2017, pp. 68–77, 2019.

[93] B. Schuh, B. Völker, J. Todt, K. S. Kormout, N. Schell, and A. Hohenwarter, "Influence of annealing on microstructure and mechanical properties of a nanocrystalline CrCoNi medium-entropy alloy," Materials, vol. 11, no. 5, 2018.

[94] C. Y. Hsu, C. C. Juan, W. R. Wang, T. S. Sheu, J. W. Yeh, and S. K. Chen, "On the superior hot hardness and softening resistance of AlCoCr xFeMo 0.5Ni high-entropy alloys," Materials Science and Engineering A, vol. 528, no. 10–11, pp. 3581–3588, 2011.

[95] Z. G. Zhu, K. H. Ma, Q. Wang, and C. H. Shek, "Compositional dependence of phase formation and mechanical properties in three CoCrFeNi-(Mn/Al/Cu) high entropy alloys," Intermetallics, vol. 79, pp. 1–11, 2016.

[96] D. H. Xiao et al., "Microstructure, mechanical and corrosion behaviors of AlCoCuFeNi-(Cr,Ti) high entropy alloys," Materials and Design, vol. 116, pp. 438–447, 2017.

[97] N. D. Stepanov, N. Y. Yurchenko, D. V. Skibin, M. A. Tikhonovsky, and G. A. Salishchev, "Structure and mechanical properties of the AlCr<inf>x</inf>NbTiV (x = 0, 0.5, 1, 1.5) high entropy alloys," Journal of Alloys and Compounds, vol. 652, pp. 266–280, 2015.

[98] Y. X. Zhuang, W. J. Liu, Z. Y. Chen, H. D. Xue, and J. C. He, "Effect of elemental interaction on microstructure and mechanical properties of FeCoNiCuAl alloys," Materials Science and Engineering A, vol. 556, pp. 395–399, 2012.

[99] G. A. Salishchev et al., "Effect of Mn and v on structure and mechanical properties of high-entropy alloys based on CoCrFeNi system," Journal of Alloys and Compounds, vol. 591, pp. 11–21, 2014.

[100] M. R. Chen, S. J. Lin, J. W. Yeh, S. K. Chen, Y. S. Huang, and M. H. Chuang, “Effect of vanadium addition on the microstructure, hardness, and wear resistance of Al0.5CoCrCuFeNi high-entropy alloy,” Metallurgical and Materials Transactions A: Physical Metallurgy and Materials Science, vol. 37, no. 5, pp. 1363–1369, 2006.

[101] Y. Dong, K. Zhou, Y. Lu, X. Gao, T. Wang, and T. Li, “Effect of vanadium addition on the microstructure and properties of AlCoCrFeNi high entropy alloy,” Materials and Design, vol. 57, pp. 67–72, 2014.

[102] Z. Lyu, C. Lee, S. Y. Wang, X. Fan, J. W. Yeh, and P. K. Liaw, “Effects of Constituent Elements and Fabrication Methods on Mechanical Behavior of High-Entropy Alloys: A Review,” Metallurgical and Materials Transactions A: Physical Metallurgy and Materials Science, vol. 50, no. 1, pp. 1–28, 2019.

[103] C. Li, J. C. Li, M. Zhao, and Q. Jiang, “Effect of alloying elements on microstructure and properties of multiprincipal elements high-entropy alloys,” Journal of Alloys and Compounds, vol. 475, no. 1–2, pp. 752–757, 2009.

[104] T. Zhang et al., “Microstructure and mechanical properties of FexCoCrNiMn high-entropy alloys,” Journal of Materials Science and Technology, vol. 35, no. 10, pp. 2331–2335, 2019.

[105] S. Gorsse, M. H. Nguyen, O. N. Senkov, and D. B. Miracle, “Database on the mechanical properties of high entropy alloys and complex concentrated alloys,” Data in Brief, vol. 21, pp. 2664–2678, 2018.

[106] S. Guo and C. T. Liu, “Phase stability in high entropy alloys : Formation of solid-solution phase or amorphous phase,” Progress in Natural Science: Materials International, vol. 21, no. 6, pp. 433–446, 2011.

[107] Z. Wang et al., “Quantitative determination of the lattice constant in high entropy alloys,” Scripta Materialia, vol. 162, pp. 468–471, 2019.

[108] Z. Li, K. G. Pradeep, Y. Deng, D. Raabe, and C. C. Tasan, “Metastable high-entropy dual-phase alloys overcome the strength-ductility trade-off,” Nature, vol. 534, no. 7606, pp. 227–230, 2016.

[109] M. Jafary-Zadeh, Z. H. Aitken, R. Tavakoli, and Y. W. Zhang, “On the controllability of phase formation in rapid solidification of high entropy alloys,” Journal of Alloys and Compounds, vol. 748, pp. 679–686, 2018.

[110] Z. Tang, S. Zhang, R. Cai, Q. Zhou, and H. Wang, “Designing High Entropy Alloys with Dual fcc and bcc Solid-Solution Phases: Structures and Mechanical Properties,” Metallurgical and Materials Transactions A: Physical Metallurgy and Materials Science, vol. 50, no. 4, pp. 1888–1901, 2019.

[111] Y. L. Zhao et al., “Development of high-strength Co-free high-entropy alloys hardened by nanosized precipitates,” Scripta Materialia, vol. 148, pp. 51–55,

2018.

[112] S. P. Wang, E. Ma, and J. Xu, “Notch fracture toughness of body-centered-cubic (TiZrNbTa)–Mo high-entropy alloys,” Intermetallics, vol. 103, no. August, pp. 78–87, 2018.

[113] Y. Zhuang, W. Liu, P. Xing, F. Wang, and J. He, “Effect of Co element on microstructure and mechanical properties of FeCoxNiCuAl alloys,” Acta Metallurgica Sinica (English Letters), vol. 25, no. 2, pp. 124–130, 2012.

[114] Y. X. Zhuang, H. D. Xue, Z. Y. Chen, Z. Y. Hu, and J. C. He, “Effect of annealing treatment on microstructures and mechanical properties of FeCoNiCuAl high entropy alloys,” Materials Science and Engineering A, vol. 572, pp. 30–35, 2013.

[115] J. W. Klement, RH. Willens, P. Duwez, “Non-crystalline structure in solidified gold-silicon alloys,” Nature. vol. 187, no. 4740, pp. 869-870, 1960.

[116] K. Russew and L. Stojanova, “Glassy Metals,” Glassy Metals, pp. 1–262, 2016.

[117] W. L. Johnson, “Thermodynamic and kinetic aspects of the crystal to glass transformation in metallic materials,” Progress in Materials Science, vol. 30, no. 2, pp. 81–134, 1986.

[118] W. H. Wang, “Bulk metallic glasses with functional physical properties,” Advanced Materials, vol. 21, no. 45, pp. 4524–4544, 2009.

[119] W. H. Wang, C. Dong, and C. H. Shek, “Bulk metallic glasses,” Materials Science and Engineering R: Reports, vol. 44, no. 2–3, pp. 45–90, 2004.

[120] A. Inoue and A. Takeuchi, “Recent development and application products of bulk glassy alloys,” Acta Materialia, vol. 59, no. 6, pp. 2243–2267, 2011.

[121] H. Wang et al., “Effect of cobalt microalloying on the glass forming ability of Ti-Cu-Pd-Zr metallic glass,” Journal of Non-Crystalline Solids, vol. 379, pp. 155–160, 2013.

[122] K. S. N. Satish Idury, B. S. Murty, and J. Bhatt, “Thermodynamic modeling and composition design for the formation of Zr-Ti-Cu-Ni-Al high entropy bulk metallic glasses,” Intermetallics, vol. 65, pp. 42–50, 2015.

[123] M. C. Gao, P. K. Liaw, J. W. Yeh, and Y. Zhang, “High-entropy alloys: Fundamentals and applications,” High-Entropy Alloys: Fundamentals and Applications, pp. 1–516, 2016.

[124] K. Zhao, X. X. Xia, H. Y. Bai, D. Q. Zhao, and W. H. Wang, “Room temperature homogeneous flow in a bulk metallic glass with low glass transition temperature,” Applied Physics Letters, vol. 98, no. 14, pp. 1–4, 2011.

[125] W. H. Wang, “High-Entropy Metallic Glasses,” Jom, vol. 66, no. 10, pp. 2067–

2077, 2014.

[126] G. Bizhanova, F. Li, Y. Ma, P. Gong, and X. Wang, “Development and crystallization kinetics of novel near-equiatomic high-entropy bulk metallic glasses,” Journal of Alloys and Compounds, vol. 779, pp. 474–486, 2019.

[127] F. Sıkan, G. Polat, I. Kalay, and Y. E. Kalay, “Effect of Sm on Crystallization Kinetics of Cu-Zr-Al Metallic Glasses,” Thermochimica Acta, vol. 683, no. October 2019, p. 178439, 2020.

[128] J. H. Pi, Z. Z. Wang, X. C. He, Y. Q. Bai, and R. Zhen, “Nanoindentation mechanical properties of glassy Cu29Zr32Ti15Al5Ni19,” Journal of Alloys and Compounds, vol. 657, pp. 726–732, 2016.

[129] Q. Fang, M. Yi, J. Li, B. Liu, and Z. Huang, “Deformation behaviors of Cu 29 Zr 32 Ti 15 Al 5 Ni 19 high entropy bulk metallic glass during nanoindentation,” Applied Surface Science, vol. 443, pp. 122–130, 2018.

[130] T. Wada, J. Jiang, K. Yubuta, H. Kato, and A. Takeuchi, “Septenary Zr–Hf–Ti–Al–Co–Ni–Cu high-entropy bulk metallic glasses with centimeter-scale glass-forming ability,” Materialia, vol. 7, no. June, pp. 3–8, 2019.

[131] D. Wang and P. Li, “Thermodynamic and mechanical properties of Cu-Zr-Al-Ti bulk metallic glasses,” AIP Advances, vol. 8, no. 12, 2018.

[132] A. Takeuchi, K. Amiya, T. Wada, K. Yubuta, W. Zhang, and A. Makino, “Alloy designs of high-entropy crystalline and bulk glassy alloys by evaluating mixing enthalpy and delta parameter for quinary to decimal equi-atomic alloys,” Materials Transactions, vol. 55, no. 1, pp. 165–170, 2014.

[133] A. Takeuchi et al., “Alloy design for high-entropy bulk glassy alloys,” Procedia Engineering, vol. 36, pp. 226–234, 2012.

[134] Q. Fang, M. Yi, J. Li, B. Liu, and Z. Huang, “Deformation behaviors of Cu 29 Zr 32 Ti 15 Al 5 Ni 19 high entropy bulk metallic glass during nanoindentation,” Applied Surface Science, vol. 443, no. Aemt, pp. 122–130, 2018.

[135] S. Chen, Y. Tong, and P. K. Liaw, “Additive manufacturing of high-entropy alloys: A review,” Entropy, vol. 20, no. 12, 2018.

[136] N. T. Aboulkhair, M. Simonelli, L. Parry, I. Ashcroft, C. Tuck, and R. Hague, “3D printing of Aluminium alloys: Additive Manufacturing of Aluminium alloys using selective laser melting,” Progress in Materials Science, vol. 106, no. May, p. 100578, 2019.

[137] A. Kumar and R. D. K. Misra, 3D-printed titanium alloys for orthopedic applications. Elsevier Inc., 2018.

[138] Y. M. Wang et al., “Additively manufactured hierarchical stainless steels with

high strength and ductility," Nature Materials, vol. 17, no. 1, pp. 63–70, 2018.

[139] Z. G. Zhu et al., "Hierarchical microstructure and strengthening mechanisms of a CoCrFeNiMn high entropy alloy additively manufactured by selective laser melting," Scripta Materialia, vol. 154, pp. 20–24, 2018.

[140] S. Xiang et al., "Microstructures and mechanical properties of CrMnFeCoNi high entropy alloys fabricated using laser metal deposition technique," Journal of Alloys and Compounds, vol. 773, pp. 387–392, 2019.

[141] B. A. Welk, R. E. A. Williams, G. B. Viswanathan, M. A. Gibson, P. K. Liaw, and H. L. Fraser, "Nature of the interfaces between the constituent phases in the high entropy alloy CoCrCuFeNiAl," Ultramicroscopy, vol. 134, pp. 193–199, 2013.

[142] Y. Brif, M. Thomas, and I. Todd, "The use of high-entropy alloys in additive manufacturing," Scripta Materialia, vol. 99, no. October 2017, pp. 93–96, 2015.

APPENDICES

A. Software for Calculation of Thermophysical Properties of HEAs

Python based software is created by Res. Assist. Doğuhan Sarıtürk to calculate the basic parameters to design HEAs. The citation details and doi number of the software as follows:

Doğuhan Sarıtürk. (2019, December 20). HEACalculator (Version v.0.1-alpha). Zenodo. http://doi.org/10.5281/zenodo.3590319

CURRICULUM VITAE

PERSONAL INFORMATION

Surname, Name	: Polat, Gökhan
Nationality	: Turkish (TC)
Date and Place of Birth	: 10 August 1990, Kars
Phone	: +90 312 210 58 42
E-mail	: gokhanpolat87@gmail.com

EDUCATION

Degree	**Institution**	**Year of Graduation**
MS	Yıldız Technical University Metallurgical and Materials Engineering	2013
BS	Yıldız Technical University Metallurgical and Materials Engineering	2010
High School	İncirli High School, Ankara	2005

WORK EXPERIENCE

Year	**Place**	**Enrollment**
2018-Present	Necmettin Erbakan University	Research Assistant
2014-2018	METU	Research Assistant
2011 December-2014	Yıldız Technical University	Research Assistant
2011-August-December	Necmettin Erbakan University	Research Assistant

FOREIGN LANGUAGES

Advanced English

SEMINARS AND COURSES:

1. European XFEL/DESY Photon Science Users' Meeting, Hamburg, Germany, 27-29 January 2016.
2. DESY/European XFEL - Turkey Workshop "Science at Accelerator-Based X-Ray Sources", Hamburg, Germany, 26 January 2016
3. 13th School on Synchrotron Radiation: Fundamentals, Methods and Applications, Grado, Italy, 14-25 September 2015

PROJECTS:

1. Development of light weight and high strength high entropy alloys (HEAs), TÜBİTAK Project, Scholarship Student, (01/04/2017-…)
2. Design and production of iron based, light and high strength high entropy alloys (HEAs), BAP Project, Middle East Technical University, Researcher, (01/01/2017 - 29/12/2018)
3. Production of high strength and ductile amorphous-nano crystalline steels by using of rapid solidification techniques, BAP Project, Middle East Technical University, Researcher, (01/01/2016 - 31/12/2016)
4. Investigation of use of waste plastics as a reducing agent in production of iron nuggets from composite pellets, BAP Project, Yıldız Technical University, Researcher (2011-2014)

PUBLICATIONS:

1. POLAT GÖKHAN, ERDAL ZİYA ANIL, KALAY YUNUS EREN Design of Novel Non-Equiatomic Cu-Ni-Al-Ti Composite Medium Entropy Alloys

(MEAs), submitted to Journal of Materials Engineering and Performance (Under Review)

2. SIKAN FATİH, POLAT GÖKHAN, KALAY İLKAY, KALAY YUNUS EREN (2020). Effect of Sm on Crystallization Kinetics of Cu-Zr-Al Metallic Glasses. THERMOCHIMICA ACTA, 683, 1-10., Doi: https://doi.org/10.1016/j.tca.2019.178439
3. KOTAN HASAN, POLAT GÖKHAN, BATIBAY AHMET BURÇİN, Darling Kris (2019). Microstructural Stability of Nanocrystalline Stainless Steels with Solute Additions Synthesized from Elemental Powders by Mechanical Alloying. European Congress and Exhibition on Advanced Materials and Processes 2019
4. POLAT GÖKHAN, ERDAL ZİYA ANIL, KALAY YUNUS EREN (2019). Effect of B on the Properties of Low Density High Entropy Alloys (LWHEAs) Including Al, Ti, V, Cr and Mn Elements. European Congress and Exhibition on Advanced Materials and Processes 2019
5. POLAT GÖKHAN, ERDAL ZİYA ANIL, KALAY YUNUS EREN (2018). Design, Production and Characterization of AlTiVMnSix(x=0.25, 0.50) Low Density High Entropy Alloys(LWHEAs). 19th International Metallurgy and Materials Congress
6. ERDAL ZİYA ANIL, POLAT GÖKHAN, KALAY YUNUS EREN (2018). Mechanical Properties of FeCoCrNi High Entropy Alloy (HEA) Produced from Industrial Raw Materials by Induction Melting. 19th International Metallurgy and Materials Congress
7. POLAT GÖKHAN, ERDAL ZİYA ANIL, KALAY YUNUS EREN (2018). Design and Structural Investigation of TiCrMnVAl Low Density High Entropy Alloy (LWHEA). European Materials Research Society (E-MRS) 2018 Fall Meeting
8. POLAT GÖKHAN, KALAY YUNUS EREN (2017). Developing Al-Sm Alloys for Structural Applications. TMS 2017 146th Annual Meeting and Exhibition

9. POLAT GÖKHAN, KOCAOĞLU YILMAZER DICLE, SARIDEDE MUHLİS NEZİHİ (2016). Reduction Conditions of Briquetted Solid Wastes Generated by the Integrated Iron and Steel Plant. World Academy of Science, Engineering and Technology
10. BİROL BURAK, POLAT GÖKHAN, SARIDEDE MUHLİS NEZİHİ (2015). Estimation Model for Electrical Conductivity of Molten CaF2 Al2O3 CaO Slags Based on Optical Basicity. JOM, 67(2), 427-435., Doi: 10.1007/s11837-014-1230-6
11. POLAT GÖKHAN, BİROL BURAK, SARIDEDE MUHLİS NEZİHİ (2014). Utilization of waste polyethylene terephthalate as a reducing agent in the reduction of iron ore composite pellets. International Journal of Minerals, Metallurgy, and Materials, 21(8), 748-754., Doi: 10.1007/s12613-014-0967-9
12. POLAT GÖKHAN, BİROL BURAK, SARIDEDE MUHLİS NEZİHİ. Using of Waste PET Polyethylene Terephthalate as an Alternative Reductant in Iron and Steel Industry. 22nd International Conference on Metallurgy and Materials (METAL 2013)

AWARDS:

1. Young Researcher Award, 19th International Metallurgy and Materials Congress, İstanbul, Turkey, October 2018
2. Best Poster Contest Honorable Mention, 22nd International Conference on Metallurgy and Materials (METAL 2013), Brno, Czech Republic, May 2013